Influence of an external gas puff on the RI-mode confinement properties in TEXTOR

Inaugural - Dissertation

zur
Erlangung des Doktorgrades der
Mathematisch-Naturwissenschaftlichen Fakultät
der Heinrich-Heine-Universität Düsseldorf

vorgelegt von

Denis, Kalupin

aus **Simpheropol**

2002

Gedruckt mit der Genehmigung
der Mathematisch-Naturwissen-schaftlichen Fakultät
der Heinrich-Heine-Universität Düsseldorf

Referent: Prof. Dr. K.H. Spatschek

Korreferent: Prof. Dr. U. Samm

Korreferent: Prof. Dr. R. Weynants

Tag der mündlichen Prüfung: 10.06.2002

Abstract

An actual subject of experimental and theoretical studies in present day fusion research is the development of an operational scenario combining simultaneously high confinement, with at least H-mode quality, and high densities, around or above the empirical Greenwald limit. Recently, this subject was studied in TEXTOR Radiative Improved (RI) mode discharges, in which the seeding of a small amount of impurities is helpful in a transition to the improved confinement stage. It was found that by the careful tailoring of external fuelling and optimisation of the wall conditions it is possible to maintain the H-mode or even higher quality confinement at densities much above Greenwald density limit. However, more intense fuelling, aimed to extend maximal achievable densities, led to the progressive confinement deterioration.

The theory explains the transition to the RI-mode as a bifurcation into the stage where the transport governed by the Ion Temperature Gradient (ITG) instability is significantly reduced due to a high density gradient and high value of the effective charge. The numerical studies of an influence of the gas puff intensity on confinement properties of plasma, done with the help of the 1-D transport code RITM, show that the same theory can be used for an explanation of the confinement rollover triggered by a strong gas puff.

The code was modified in order to simulate the effect of the gas puff on the confinement properties. The anomalous transport coefficients in the plasma core include contributions from the ITG and Dissipative Trapped Electron (DTE) instabilities. The transport at the plasma edge under RI-mode conditions might be described by the electrostatic turbulence caused by electric currents in the scrape-off layer of the limiter. The present computations show that this assumption for the edge transport does not allow the modeling of an effect of the gas puff intensity on the profiles evolution in agreement with experimental observations.

The level of the edge transport must be increased significantly in order to reproduce the evolution of the plasma density and the effective ion charge profiles during confinement degradation caused by a strong gas puff. An increase of this order is in agreement with reflectometer measurements and could tentatively be explained by the effect of neutrals on Drift Resistive Ballooning instability.

Although, an increase of the edge transport is a necessary condition for the core confinement deterioration, the latter is produced by the resumption of ITG instability in the plasma core. The present studies show, that the reduction of impurity content of plasma and high positive time derivative of the density provided by a strong gas puff are crucial conditions for the restart of the ITG mode.

Contents:

Chapter 1

Introduction

1.1 Present and future energy supply, prospects and restrictions

The exhaust produced by the burn of fossil fuels and the huge amount of greenhouse gases released into the atmosphere are the reasons constraining to supply a new energy source for the economic and clean energy production. The number of conceivable non-fossil candidates capable of substantial contribution to the long-term energy production is very limited: nuclear fission, nuclear fusion, hydro-electricity and renewables. Although the renewable energy sources in the world are large and inexhaustible, they have, unfortunately, a limited potential for the energy production [1]. Natural obstacles of renewables, low energy density and fluctuations in time, require energy storage that leads to the extra costs. This can be illustrated by the example of solar cells. To produce 1 GW of power, which is a typical value for the modern fossil power plant, assuming the solar irradiation on a horizontal surface in a Middle Europe of 1000-1100 kWh/(m^2yr) and the best efficiency of sells about 20%, one gets the surface of 50 km^2. The hydro-electricity production does not cause the emission of greenhouse gases but its negative impact on the nature comes from significant changes in the local ecological system, which affects the flora and fauna of the earth, since the huge storage of water is needed.

Another option is given by nuclear energy: fission and fusion. In the case of fission, highly radioactive waste is produced; the volume is about 4m^3 (or 28 tons) of irradiated fuel per GWyr. Moreover, about 27 tons of this irradiated fuel can, in principle, be reprocessed and reused in other reactors. Finally only one tone or 50 dm^3 of a highly activated waste is produced per GWyr. At present, the fission energy is not accepted by the world society because of the possible danger implied by radioactivity of fuel.

The nuclear fusion is still on the way to become an option for the energy production. It promises to be the safe, inexhaustible and rather clean energy production method. In case of fusion, only a small amount of fuel, 100 kg of deuterium and 150 kg of tritium, are needed for the production of 1 GWyr. From the safety point of view, tritium has a very short lifetime in comparison to fission materials. Also, only a few grams of tritium will be contained simultaneously in the reactor. It means that, even in

the case of a big accident, its release into the atmosphere will not lead to a radioactive pollution like it was in Chernobyl. All those elements characterise fusion as the best candidate for the long-term safe energy source.

There are presently two approaches to realise controlled nuclear fusion on the earth: inertial and magnetic fusion. Inertial fusion consists of micro-explosion of the fuel pellet by powerful lasers or particle beams. The confinement of the fuel is based on the inertia of the pellet fuel mass, which resists the natural expansion when it is heated to thermonuclear temperatures. Magnetic fusion uses the magnetic fields to confine the fuel. European fusion research is concentrated on the latest approach. At present days, the magnetic fusion devices called TOKAMAK make a strong effort to demonstrate the feasibility of a fusion reactor.

1.2 Tokamak

Since 1963 [2,3] the toroidal devices called tokamak are leading the competition of the devices in which fusion reaction could be achieved. This type of device will be briefly described in the current section.

The plasma in these machines is obtained by a heating of gas up to the temperatures around 10 millions Kelvin. Together with the characteristic densities in the range of 10^{19} – $1.5*10^{20}$ particles per cubic meter, that gives an idea of the numbers involved. The low density (for the comparison: the atmospheric air has about $2*10^{25}$ particles per cubic meter) requires a vacuum vessel as a basic component of the tokamak. The high temperature places the confinement of such a plasma as the first problem of the experimental set-up. Without any measures, the contact with the walls will lead to a rapid cooling of plasma.

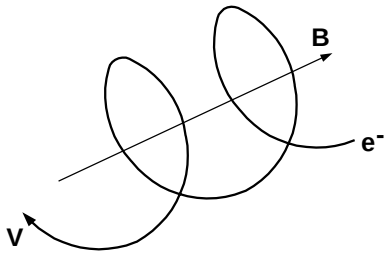

Fig 1.1 Charged particle circulate around a magnetic field, performing the cyclotron motion.

Applying of the magnetic field can significantly increase the confinement of this high temperature plasma. In magnetic field charged particles gyrate around the field line (see Fig 1.1). The cyclotron motion reduces the transport of the charged ions and electrons in the direction perpendicular to the magnetic field. Therefore, the magnetic field must be configured in such a way that it does not cross the vacuum vessel.

In 1963 Russians physicists [2] came up with the tokamak, *Toroidal'naya Kamera Magnitnaya Katushka (Toroidal Chamber with Magnetic Coil)*, concept based on the ideas of Sakharov [4]. In this device the vacuum vessel has a shape of a torus (see Fig

1.2). The largest component of the magnetic field, along the torus, is produced by the toroidal magnetic field coils and is called toroidal magnetic field, B_t. The plasma is heated by the current induced by a transformer, where the plasma itself serves as a secondary winding (Ohmic Heating). This plasma current induces the so called poloidal magnetic field, which encircles the center of the tube. The toroidal and poloidal magnetic fields together produce a helical field, whose filed lines lie on the toroidal surfaces as it is shown in the Fig. 1.3.

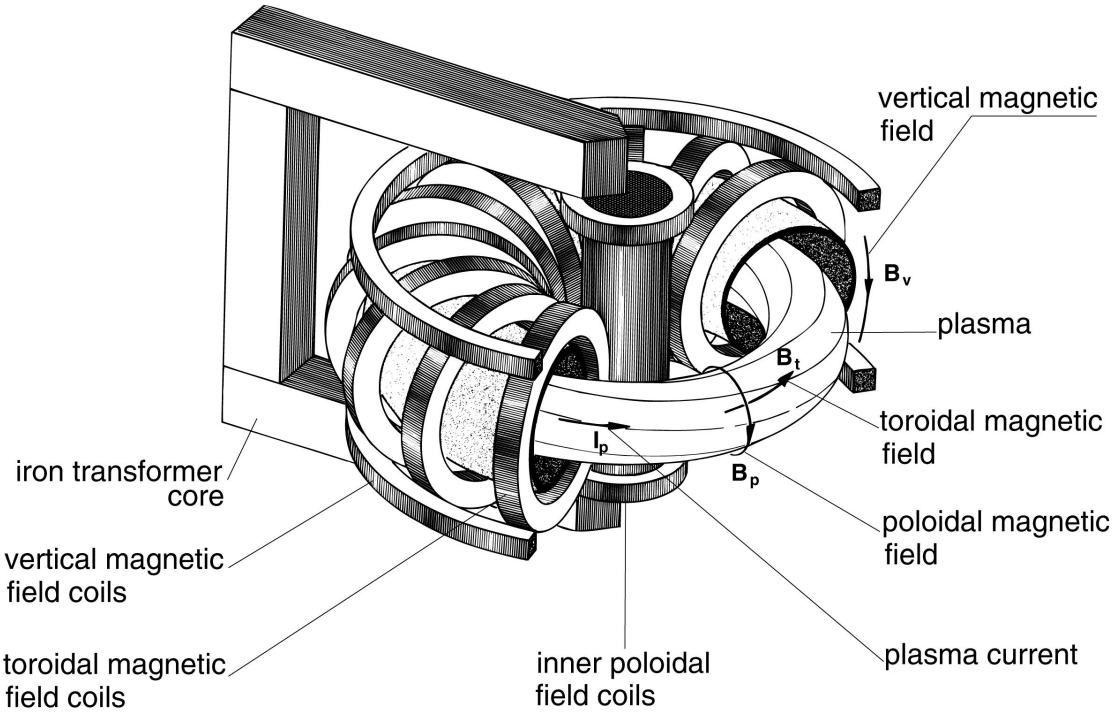

Fig.1.2 Schematic representation of the tokamak set-up.

These magnetic fields are the principle components for the tokamak device. One element not yet mentioned is a vertical magnetic field. This field is needed to counteract the hoop forces, which are the consequences of the toroidal geometry and trying to expand the plasma ring. The first of these forces is the natural tendency of a current loop to expand in an effort to lower its magnetic energy. The second one consists of the sum of the centrifugal and grad-B forces of individual particles during their motion along the field line. These outward forces are balanced by the Lorentz force produced by the vertical magnetic field and plasma current.

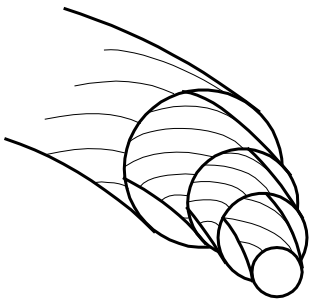

Fig.1.3 Magnetic field lines and surfaces from the tokamak.

Realistic operation of the tokamak device requires a fast and accurate timing of all of the circuits and robust feedback systems necessary to control different plasma parameters. Besides the magnetic field system, stable operation of such a machine needs a lot of engineering skill and physical understanding, which are still in the list of actual topics of the tokamak society.

1.3 What is the performance?

In the fusion reaction, two nuclei of the light elements are brought together within the range of their strong interaction. As a consequence, the nuclei react forming new energetic particles. The most accessible and promising reaction for fusion reactor is the one between deuterium, *D*, and tritium, *T*, in which alpha particle, ${}_2^4He$, and energetic neutron, *n*, are produced:

$$D + T \longrightarrow {}_2^4He + 17.58\ MeV$$

However, in order to bring these two nuclei together, the repelling Coulomb force has to be overcome over a relatively large distance. On the sun, the huge gravity forces help to bring two nuclei together. But, the gravity on the earth is not so strong, thus,

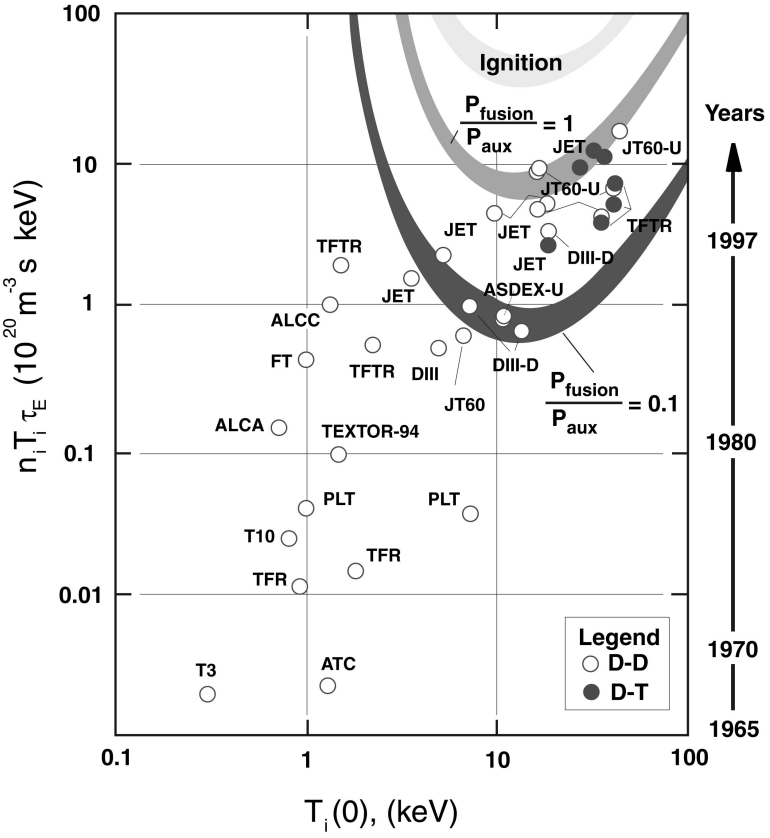

Fig.1.4 Fusion triple product achieved in different tokamaks as a function of the ion temperature.

much higher energies are needed to overcome the repelling force. It means that the temperatures, which should be achieved in the fusion machine, are around 10^8 K. For the high energy gain, a high density, *n*, is required. The volume integral over the pressure is the stored kinetic energy:

$$W = 3/2\,k \int (n_e T_e + n_i T_i)\, dV\,, \tag{1.1}$$

where *k* is the Boltzmann constant and $T_{e,i}$ denotes the temperatures of electrons and ions, respectively. Loss processes, due to Coloumb collisions and turbulences, tend to decrease *W*. To compensate the losses, the plasma should be permanently heated with the deposited power, P_{in}. The effective loss can be quantified in terms of a typical timescale, the energy confinement time, τ_E. This value can be estimated by expression:

$$\tau_E = W / (P_{in} - \partial W/\partial t)\,, \tag{1.2}$$

the bigger value representing the better energy confinement. The triple product of the temperature, density and energy confinement time, $n_i T_i \tau_E$, is a parameter illustrating the fusion performance. It is seen from Fig. 1.4 that the value of the triple product required for the ignition condition is about $5*10^{21}$ m^{-3}s keV. Since the birth time of tokamaks, a significant progress in the performance was made. Such a promising evolution makes us sure about the feasibility of controlled fusion on the earth and tokamak as the reactor concept.

1.4 Heating

1.4.1 Ohmic Heating (OH)

As it was mentioned in the previous section, in order to overcome the Coulomb forces of two nuclei a high temperature of 10^8 K (~10eV) should be achieved in a fusion machine. What are the existent methods for plasma heating in tokamaks? The most obvious one is the Ohmic heating. The loop voltage induced by transformer creates a plasma current needed for the plasma equilibrium, where the plasma works as a secondary winding. This current heats the plasma because of the electrical resistance. The later is given by the expression [5]:

$$\eta \simeq 3\cdot 10^{-8}\, Z_{eff} T_e^{-3/2} \quad (Ohm/m)\,, \tag{1.3}$$

where T_e is the electron temperature in keV, Z_{eff} is the effective plasma charge. This value very strongly decreases with the rise of temperature (at the tokamak temperatures this value is much smaller than the copper resistance), making the Ohmic heating ineffective at temperatures above several keV and therefore requiring an additional heating of the plasma.

1.4.2 Neutral Beam Injection (NBI)

The injection of neutrals is a very effective method of heating in high temperature plasmas. It is done by the injection of neutral particles, accelerated up to the high energies, into the plasma where they are ionised, captured by the magnetic field and decelerated due to collisions with plasma electrons and ions. The fractions of the energy transferred to electrons and ions depend on the energy of the beam, E_B: if E_B higher than the certain energy E^* then the main heating goes to the electrons, if $E_B < E^*$ – to ions, where E^* depends on plasma parameters and about $15T_e$, here and later temperature is measured in eV. The penetration length of the beam into the plasma depends on the energy of the beam and plasma density. In order to increase the absorption of the beam the tangential injection is used. In this case the beam can be directed in two directions "co-" and "counter-" with respect to the direction of the plasma current. The neutral injection can be very efficiently used, also, for the generation of the plasma current, "current drive".

1.4.3 Ion Cyclotron Resonance Heating (ICRH)

Electromagnetic waves in the range of the ion cyclotron resonance can easily propagate into the plasma and are absorbed in a layer were the wave frequency is equal to one of the harmonics of the gyro-frequency, in the zone of Doppler resonance $\omega - n\omega_{Ce} = k_{\|} v_{\|}$. For the increase of the absorption efficiency of the electromagnetic wave two methods can be used. The first one is such a called minority heating scenario, when the heating is realised on a small fraction of minority ions. These ions are heated up to relatively high perpendicular energies, when the heating scheme becomes similar to NBI. The second scheme is the so-called mode conversion mechanism. The fast electromagnetic waves are launched into the plasma where they are converted into the slow waves. The transfer of a power from slow waves to particles is through the Landau damping mechanism.

1.4.4 Electron Cyclotron Resonance Heating (ECRH)

This method is based on the absorption of electromagnetic waves in the range of microwaves (~10^2GHz), with frequencies close to the electron cyclotron frequency. As in the case of ICRH, the absorption is realised in the zone of Doppler resonance. The main advantage of this method is the locality of the heating.

1.5 Transport

One of the main problems in fusion research is that the experimentally observed energy confinement time is much shorter than that determined by the Coulomb collisions of the gyrating particles (Classical Transport) [5]. In an homogeneous magnetic field the coefficients of the ion, χ_i, and electron, χ_e, heat conductivities as well as the diffusion coefficient, D, can be defined by the equations:

$$\chi_i \cong \rho_i^2 \nu_i; \quad \chi_e \cong D \cong \rho_e^2 \nu_e, \tag{1.4}$$

where the ρ_i, ρ_e are the averaged Larmor radii and ν_i, ν_e are the averaged collision frequencies. In systems with the toroidal symmetry, like tokamak, the diffusion mechanism is more complicate because of the particle drifts in inhomogeneous magnetic fields. The theory of A.A.Galeev and R.Z.Sagdeev [6], the so called neo-classical theory, takes into account the drift effects which increase the transport coefficients with respect to the classical values.

Neo-classical theory can be clearly explained from the consideration of the motion of a charge particle in the magnetic field of tokamak. We describe the movement of the guide-center of the particle gyro-orbit with the radius $\rho = \upsilon_\perp / \omega_c$, where $\omega = eB/mc$ is the cyclotron frequency of the charged particle with the mass *m*. In the magnetic field the total energy of the moving particle is constant:

$$E = m\upsilon_\parallel^2 / 2 + m\upsilon_\perp^2 / 2 = const\,, \tag{1.5}$$

where $\upsilon_\perp$ and $\upsilon_\parallel$ are velocity components parallel and perpendicular to the magnetic field. Also the perpendicular adiabatic invariant is constant:

$$\mu_\perp = m\upsilon_\perp^2 / 2B = const\,. \tag{1.6}$$

Therefore, when a particle moves from the low field side to the high field side the parallel kinetic energy reduces and the perpendicular one grows. If the parallel energy is small compare to the perpendicular one then the particle can be reflected by the high magnetic field. The reflection occurs for particles (trapped particles) for which, at $\theta = 0$, the value of the parallel velocity satisfies the criteria: $\upsilon_\parallel^2 < 2\upsilon_\perp^2 r / R$, where *r* and *R* are the minor and major radii respectively (see Fig 1.5). Two main forces are acting on these particles, the centrifugal force,

$$F_c = m\upsilon_\parallel^2 / 2R \tag{1.7}$$

and the force caused by the magnetic field gradient,

$$F_D = -\mu_\perp \nabla B = m\upsilon_\perp^2 / 2R\,. \tag{1.8}$$

These forces lead to the drift with the velocity, υ_d. Assuming that these forces are balanced by the Lorentz force, $e\upsilon_d B/c$, one gets an expression for the drift velocity, $\upsilon_d = (\upsilon_\parallel^2 + \upsilon_\perp^2 / 2)/\omega_c R$. The drift velocity is directed along the vertical axis of symmetry, and consequently, leads to a shift inside the magnetic surface in the lower half of the torus and outside the magnetic surface in the upper half. As a result the trapped particle has a trajectory, whose projection on the poloidal cut looks like a banana (see Fig 1.5).

The characteristic shift of the particle orbit between collisions is in the order of the banana width, $\Delta \cong \upsilon_d t$, where *t* is the flight time on the half of banana. For a typical banana particle with $\upsilon_\parallel \sim r/R\sqrt{\upsilon_\perp r / R}$ and total thermal velocity $\upsilon = \sqrt{2T/m}$:

$\Delta \cong q\rho\sqrt{R/r}$, i.e. much larger than the Larmor radius, ρ. Here q is a value usually between 1 and 3, called safety factor (see next chapter). Thus neoclassical transport coefficients are increased with respect to the classical values, where the value of shift is in order of ρ.

Though, the neoclassical theory provides transport coefficients higher than the classical values, the experimentally measured χ and D exceed the neo-classical predictions by an order of magnitude. Experimental and theoretical transport studies made in two last decades showed that fluctuations can be responsible for anomalies in the heat conductivity and diffusion. Accordingly, the transport caused by particle-wave interactions is called anomalous. Two pictures of the anomalous transport exist: First, it can be assumed that the magnetic surfaces are perfect, but the fluctuating electric field drive the particle flux via fluctuating $E \times B$ drifts. This picture is referred to as 'electrostatic turbulence'. Second, fluctuations in the magnetic field can break the toroidal symmetry and destroy the set of nested flux surfaces. Field lines in such a system show a radial excursion, and particles moving along the field lines cause an enhanced radial transport. This picture is referred to as 'magnetic turbulence'. In reality, any plasma turbulence has both electric and magnetic components.

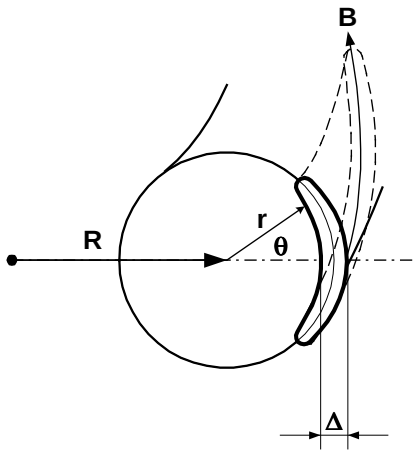

Fig.1.5 Trajectory of a trapped particle (banana orbit) in the magnetic field of tokamak

1.6 Placing this Thesis

As was discussed in the **section 1.3** the performance of the fusion machine can be quantified in terms of the triple product, $nT\tau$. It considers that an operational mode should combine the high energy confinement concurrently with a high density. The current experimental and theoretical studies on tokamaks are aimed at finding the conditions at which this combination can be achieved.

On TEXTOR, the high confinement is achieved in discharges with a seeding of a small amount of impurity ions (like Ar, Ne, Si). This regime is called Radiative Improved or RI-mode [7,8] and combines simultaneously many features needed for a

reactor grade plasma. The impurities play a crucial role in the transition to the state with improved confinement. Recent experiments were aimed to extend such an attractive regime to the higher densities preserving the confinement properties of plasma.

Gas puffing is the simplest and most frequent method for the control of the plasma density in fusion devices. However, as it has been found in many tokamaks, a too intensive puffing can lead to a progressive deterioration of the energy and particle confinement. In particular, a back transition from the High (H) confinement mode, considered as a standard operational scenario for the reactor size machine, to the Low (L) confinement mode has been observed in the divertor tokamaks JET, JT-60, DIII-D, ASDEX-U [9-11] during a strong gas puff. Normally this development is accompanied by a decrease of the time derivative of line-averaged density, $\partial\bar{n}/\partial t$, and finally can lead to the so-called fueling density limit [12].

The experiments with external gas fuelling, performed on TEXTOR tokamak demonstrate a strong dependence of plasma confinement properties on the gas injection rate. In TEXTOR RI-mode discharges with a moderate injection it was possible to rise the confinement above H-mode level at the densities significantly exceeding Greenwald density limit, converse a strong gas puff resulted in the progressive confinement deterioration towards L-mode. Usually, such a deterioration of confinement is accompanied by significant modifications at the plasma edge. The strong correlation of the core confinement to the edge density and neutral pressure is observed, where the higher values of these parameters correspond to the lower confinement.

A theory, based on the model for anomalous transport, explains the RI-mode confinement improvement as a bifurcation between the states where the transport is governed by different kinds of turbulence [14]. Recently this model was incorporated into the one-dimensional transport code RITM [13] (Radiation from Impurities in Transport Model). The results obtained with the RITM-code demonstrated the good agreement with experimental observations and can reproduce the L to RI-mode transition triggered by the impurity injection.

In the present thesis the confinement deterioration caused by strong gas puff is explained on the basis of the same model. It is done by the analysis of the results obtained in the modelling with the RITM-code and comparison to the experimental measurements performed on TEXTOR tokamak.

1.7 References

1. Ongena G. and Van Oost G., Transactions of Fusion Technology, Vol. **37**

   Mar. 2000, pp 3-15

2. Artsimovich L.A. *et al*, Plasma Physics ***7*** *(1965) 305*

3. Kadomtsev B.B., Tokamak plasma: a complex system, Institute of physics publication, Bristol 1992
4. Sakharov A.D. *et al*, in Proc. Of the 1957 Geneva Conf. On Peaceful Appl. Of Atomic Energy *(Pergamon Press, 1961)* Vol **1** pp 21-34
5. Wesson J.A., Tokamaks, Oxford University Press, 1997
6. Galeev A.A and Sagdeev R.Z., Soviet Phisics JETP **26** pp 233, 1968
7. Weynants R.R. *et al* 1999 Nucl. Fusion **39** 1637
8. Messiaen A. et al 1999, RI-mode confinement and performances on TEXTOR-94 under siliconized wall conditions, 26th EPS, Maastricht
9. Horton L.D. *et al* 1999 Nucl. Fusion **39** 1
10. Petrie T.W. *et al* 1993 Nucl. Fusion **33** 929
11. Suttrop W. *et al* 1999 J. Nucl. Mater. **266-269** 118
12. Greenwald M. *et al* 1988 Nucl.Fusion **28** 2199
13. Tokar M.Z. 1994 Plasma Phys. and Control. Fusion **36** 1819
14. Tokar M.Z. *et al* 2000 Phys. Rev. Lett. 84 895

Chapter 2

Operational modes and limits in tokamak

2.1 Safety factor and Hugill diagram

As it was described in the section 1.2 (see Fig 1.3) magnetic field lines in a tokamak have a helical structure. That means, the field line turns over the angle $d\theta$ in the poloidal direction with the shift on the angle $d\varphi$ in the toroidal direction. The length of the arc along φ is equal $Rd\varphi$, and along θ is $rd\theta$. The ratio of both arcs is equal to the ratio of the magnetic field components:

$$Rd\varphi / rd\theta = B_T / B_\theta \text{ or } d\theta / d\varphi = B_\theta R / B_T r \,. \qquad (2.1, 2.2)$$

With a full toroidal turn around the torus the angle θ changes by the value:

$$\Delta\theta = 2\pi B_\theta R / B_T r \,, \qquad (2.3)$$

or $\Delta\theta = 2\pi / q$ by the introducing

$$q = B_T r / B_\theta R \;, \qquad (2.4)$$

which is called the safety factor and plays very important role in fusion devices. Geometrically, it can be defined as the ratio of toroidal, *m*, to poloidal, *n*, numbers of rotations round the torus. If on the magnetic surface this ratio is rational the surface is also called rational.

The value *q(r)* can be interpreted in a more general way. We introduce the toroidal, Φ, and poloidal, Ψ, magnetic fluxes:

$$\Phi = \pi r^2 B_T, \quad \Psi = 2\pi R \int_0^r B_\theta dr \,. \qquad (2.5, 2.6)$$

Their increments on the interval dr are: $d\Phi = 2\pi r B_T dr, \quad d\Psi = 2\pi R B_\theta dr$. Thus the safety factor can be expressed as the rate of change in the toroidal flux with the poloidal flux,

$$q = d\Phi / d\Psi \,. \qquad (2.7)$$

This expression is more universal and can be used for plasmas of different cross-sections.

For a global characterization of the plasma in a tokamak the value of the safety factor at the edge, q_a, is normally used. For a tokamak with a circular cross-section:

$$q_a = 5 B_T a^2 / IR \,, \qquad (2.8)$$

where I is the plasma current in MA, B is in T, a and R are the minor and major radii in m. The value q_a^{-1} can be considered as the dimensionless plasma current, $q_a^{-1} = I / I_c, \quad I_c = 5 B_T a^2 / R$. As it was demonstrated by Shafranov [1], the toroidal plasma cord is destabilized by a kink instability if $q_a<1$, i.e. the plasma current can not exceed the critical value, I_c.

Plasma discharges in a tokamak can be realized only in a limited range of densities. At a given current lower and upper density limits exist. At low densities the collision frequency is very small. That leads to the birth of the so-called runaway electrons, which are accelerated up to very high energies, taking significant part of plasma current and can be dangerous for the machine operation. At high densities, atomic processes at the edge start to play an important role. That can lead to the reduction of the current channel and instability. The role of atomic processes can be quantified in terms of Hugill number, $Hu = q_a \bar{n}_e R / B_T$ or $\bar{n}_e = Hu\,(I / 5a^2)$. With an increase of this value the radiation loses from the plasma, specially at the edge, affect the current density profile that can lead to the deterioration of the energy confinement and a radiative collapse of the discharge.

Finally, the operational space of tokamaks in coordinates of current and density can be summarized in so-called Hugill diagram [2], Fig. 2.1. The Y-axis is the dimensionless current, the X-axis is the dimensionless density. The later is also called Murakami number. As it is seen from the diagram, the operational space of tokamak is limited by four lines: *:* **1** – runaway limit at low densities; **2** – current limit due to MHD activity; **3** – Murakami limit of the absolute value of density; **4** – Hugill limit of density where the Hugill number is constant.

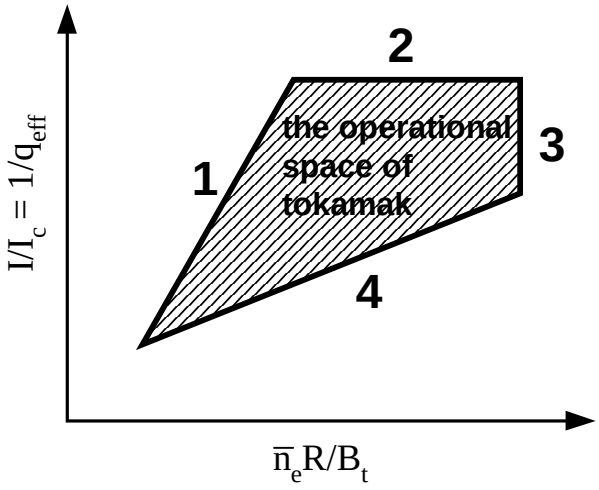

*Fig.2.1 Hugill diagram: **1** – runaway limit; **2** – current limit; **3** – Murakami limit; **4** – Hugill limit*

The operational space for TEXTOR tokamak is shown in Fig. 2.2 [3]. All of operational boundaries can be recognized in this diagram. In particular, the lack of points to the right of the graph represents Murakami and Hugill limits. This boundary is empirical and the different groups of data points show that over the past years this limit has been significantly increased by the use of the additional heating and optimization of the wall conditions. (it is discussed in the next section) The strong additional heating permits a stable operation at the higher radiation level, and the wall coating allows better control of the impurity content. Another boundary represents the current limit, the space above $1/q_a$=0.5 does not contain any point. In this region the external kink mode is destabilized, that leads to the disruption of the discharge.

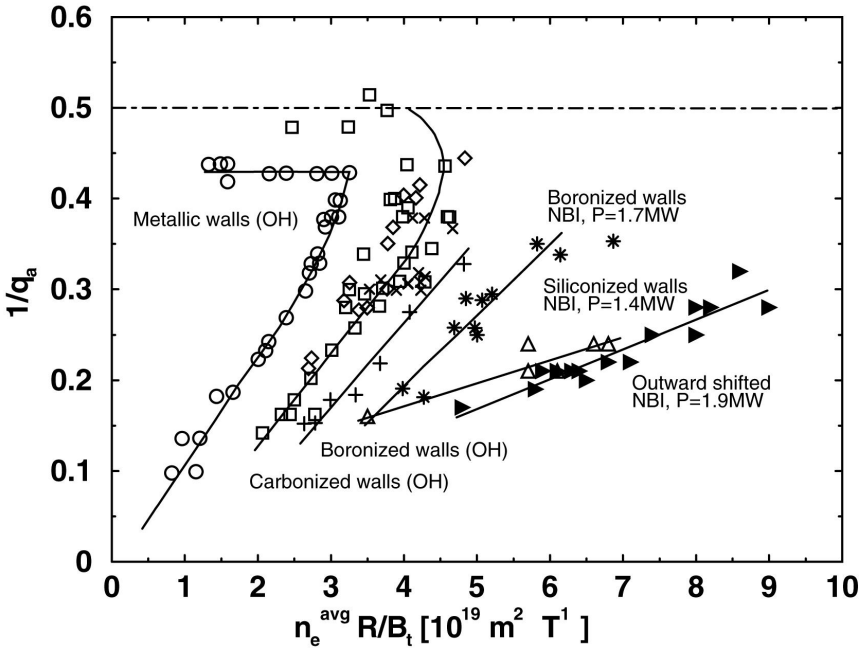

Fig.2.2 Hugill diagram for TEXTOR [3]

2.2 Density limit

Since, the density is one of the most important parameters for the reactor plasma, the current studies on many devices aimed at extending the density limit. As it was mentioned, atomic processes in plasma impose the Hugill limit for the maximal achievable density, there are two main reasons for that.

2.2.1 Radiative collapse.

Because of the dependence of the radiation intensity on the temperature, a plasma, in which the concentration of the high-Z impurities is low, radiates mainly from the edge. With an increase of the density the temperature decreases. This is accompanied by the enhancement of the radiation from low-Z impurities. A poloidally symmetric radiative belt develops around the plasma. The density limit is achieved when the radiated power reaches a certain critical value proportional to the heating power and the radiative collapse occurs. It is clear that both methods, increase of the heating power and decrease of the impurity content (possible made by the wall conditioning), allow to increase the achievable densities. Finally the critical density scales like [4]

$$n^{crit} \propto (P_{heat} /(Z_{eff} -1))^{1/2}, \tag{2.9}$$

where Z_{eff} is the effective plasma charge. The big amount of the heating power together with the possibility to have a low Z_{eff} in the present days experiments would lead to a very high values of the critical densities. Unfortunately, experimentally achieved limit of density demonstrates that other limitations for the achievable density exist and they are not related to the impurity concentration.

2.2.2 MARFE formation.

MARFE means *multifaceted asymmetric radiation from the edge*. This phenomenon is related to the transport of energy and the recycling particles at the plasma edge [5]. MARFE is the toroidal winding of dense and cold plasma, with a high radiation, created at the high field side. The characteristic radiation pattern observed with MARFE is shown on Fig. 2.3. The electron temperature inside MARFE is in the order of a few eV, the densities reach very high values of several 10^{14} cm^{-3}. The energy loss is mainly due to the radiation from impurities and caused by the ionisation and charge exchange of incoming neutral particles. Thus, the onset conditions of MARFE are strongly connected to the recycling particle flux [6,16].

The density limit, which is found to be a general observation on all of tokamaks has been analysed in detail by Greenwald [7]. He derived a very simple scaling law for the maximum achievable line-averaged density in tokamak: $n_{Gr} = I_P / \pi a^2$ called Greenwald density, here I_P is the plasma current in MA and a is the small radius in m. The ratio of the line-averaged density to Greenwald density is called Greenwald number, $f_{Gr} = \overline{n}_e / n_{Gr}$, which is, in fact, the Hugill number multiplied by a constant

around 1.7, $f_{Gr} = k \cdot Hu$. It has been realized later that Greenwald or Hugill limit is connected to the onset of MARFE [7,16].

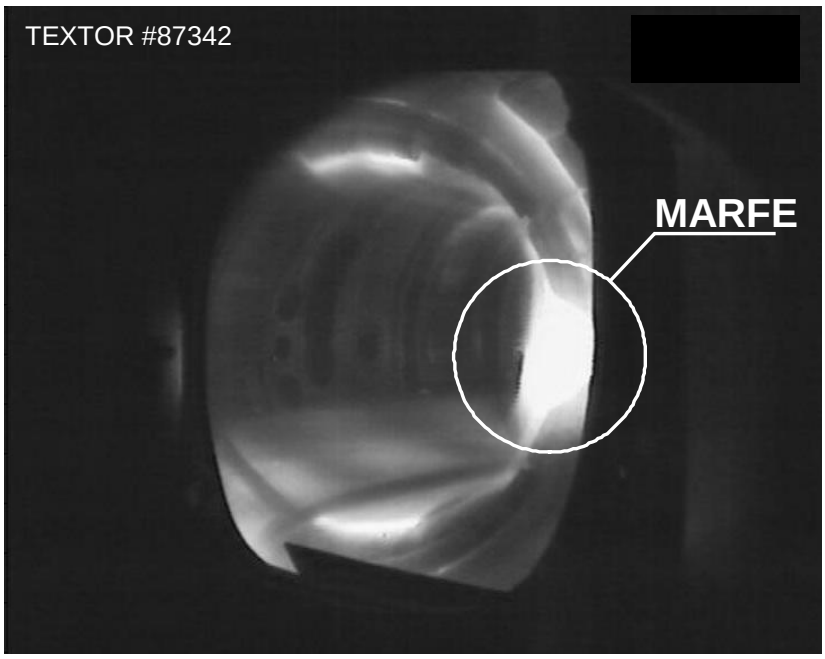

Fig. 2.3 MARFE formation in TEXTOR discharge.

Since the recycling of particles from the high field side is identified as the main cause for the limitation of density [16] as long as sufficient heating power is available and the impurity content is low, the control of this flux might help to improve the limit. Slight shift of the plasma column to the low field side helps to avoid or postpone the appearance of MARFE and achieve the densities up to twice the Greenwald limit. Unfortunately the price paid for that is the deterioration of the confinement time. Possible methods to obtain plasmas with high confinement and high density are discussed in this thesis.

2.3 Beta limit

Besides the limits discussed in sections 1.1 and 1.2, one more limit exists for the tokamak plasmas: the pressure limit [8]. This limit does not directly relate to the limits shown in Hugill diagram. The pressure limit is caused by the so-called ballooning instability. In the outer part of the torus, magnetic field lines have a curvature ~*R*. The increase of the pressure can lead to a swelling on the magnetic surface. Such a swelling of the tube with effective length ~*qR* is compensated by the strain of field lines $\sim B_T^{\,2} / 8\pi qR$. The reason of the swelling is the pressure gradient ~*p/a*, where *p=2nT*. Thus the instability develops if

$$\beta \equiv 8\pi p / B_T^2 \qquad (2.10)$$

exceeds a/qR. If we assume $q \sim q_a \sim B_T a^2 / IR$ then the critical value of the parameter β can be written in the form [9]:

$$\beta_c \equiv g(I / aB_T) \equiv gI_N , \tag{2.11}$$

where I_N is the normalized current. The coefficient g (also named β_N) is called Troyon factor or normalised beta.

The fusion power produced in tokamak scales as: $P_{fus} \sim \beta^2 B^4 V$. In order to increase the energy gain from a fusion machine it is necessary to have the maximum possible beta.

2.4 Scalings

The huge database on the confinement properties of plasmas in different tokamaks can be summarized in simple empirical expressions for τ_E called scalings. The number of such scalings is very big, each experimental group is trying to construct such an empirical dependence representing their results. Most of the scalings depend on the machine parameters and can not be used on other tokamaks without adjustment. Nevertheless, it was possible to construct some universal dependences like Neo Alcator scaling [10],

$$\tau_{NA} = 0.07 naR^2 q , \tag{2.12}$$

which well approximates the results from different machines in the Linear Ohmic Confinement regime.

It is also desirable to extrapolate the results from the present machines to those under development. Experiments from different tokamaks show that the dependence of τ_E on some parameters is weak. In such a case the accuracy of predicted values for τ_E may be in the correct order of magnitude even if these parameters are not known yet.

2.5 Ohmicaly heated plasmas (LOC, SOC, IOC)

A lot of confinement modes were discovered on tokamaks. Each of such a modes has its own dependence of the confinement time on the core and periphery plasma parameters. Thus, the peculiarities of different parameter profiles or the edge effects or a combination of both are important for the establishment of a certain mode.

From the point of view of the tokamak as a relevant reactor concept, the experimental and theoretical activities concentrate mostly on the modes which demonstrate an improvement of the energy confinement. Following the presentation of B.B.Kadomtsev [11], the confinement properties of discharges can be summarised by the diagram presented in Fig. 2.4. In ohmically heated discharges , at low plasma

density, the confinement time is proportional to the plasma density, Linear Ohmic Confinement (LOC) mode, and can be expressed by Neo-Alcator scaling law. Above the critical density [12] called Shimomura density limit,

$$n_s = (B/Rq)\sqrt{A_i\kappa/2}\,, \tag{2.13}$$

the confinement saturation can occur. Here A_i is the atomic weight and κ is the elongation of plasma. Actually, Shimomura density is one more representation of Hugill or Greenwald density limit and can be referred to the later as $n_s = \alpha n_{Gr}\sqrt{A_i\kappa/2}$. The Saturated Ohmic Confinement (SOC) mode has a weak density dependence and can be described by Shimomura scaling law [12]:

$$\tau_S = 0.07aRB\sqrt{A_i\kappa/2}\,. \tag{2.14}$$

Using appropriate wall conditioning or pellet injection it is possible to restore the linear dependence described by Neo-Alcator scaling at the densities higher than n_s. Practically, on TEXTOR in ohmically heated discharges with high density, the confinement lies between Neo-Alcator and Shimomura scalings depending upon the machine conditions.

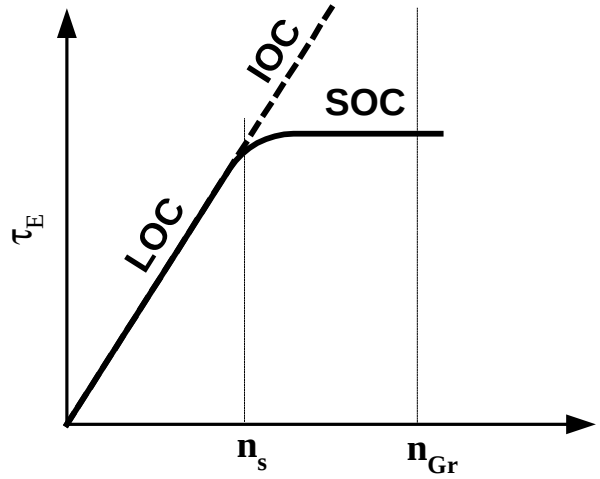

Fig. 2.4 Dependence of the energy confinement on the density in ohmically heated plasmas

2.6 Auxiliary heated plasmas (L-mode, H-mode, RI-mode)

The basic operational mode obtained in auxiliary heated discharges is the so-called Low (L) confinement mode (see Fig. 2.5). This mode is obtained automatically (the conditioning of the machine is not required and demonstrates the lowest confinement which is usually taken as a reference for the comparison of the confinement quality. On the contrary, the additional heating leads to the deterioration of confinement with

respect to the SOC-mode. The confinement in this mode does not depend on the value of density and can be described by the Goldston scaling [13],

$$\tau_G = 0.037 I_P P^{-0.5} a^{-0.37} R^{1.75} B \sqrt{A_i \kappa / 1.5}\,, \tag{2.15}$$

or by T-10 scaling [11],

$$\tau_{T-10} = \tau_S (P_{OH} / P_{tot})^{0.5}\,. \tag{2.16}$$

Both of these scalings are similar to the Shimomura one. Many improved confinement schemes have roughly the same parametric dependence, and can be characterised by their enhancement factors, $f_{H,L}$, with respect to the L-mode. The best known was discovered on ASDEX tokamak and is called High (H) confinement mode, the enhancement factor, $f_{H,L}$, for this mode is of the order of 1.5-2.0.

The H-mode is an improved confinement regime observed in the divertor and limiter machines above a certain threshold in the additional heating power. The H-mode is characterized by the following features. Usually, during the L-H transition, a small increase of the electron temperature at the plasma edge leads to a bifurcation, when the plasma proceeds to the H-mode. Profiles of the density and temperature at the periphery become steeper and form a pedestal at the plasma edge. Simultaneously, the energy confinement increases in spite of the same heating power, to a new stationary level. The particle confinement time also increases. That leads to a reduction of recycling, as it is seen in the reduction of H_α light. During H-mode the Magneto Hydro Dynamic (MHD) effects called ELMs (Edge Localised Mode) can occur. They reduce the enhancement factor, $f_{H,L}$, whose value depends on the ELMs repetition rate. Moreover, at high density a further degradation of τ_E is observed and which makes it difficult to maintain the H-mode above the Greenwald density limit (see paragraph 2.2).

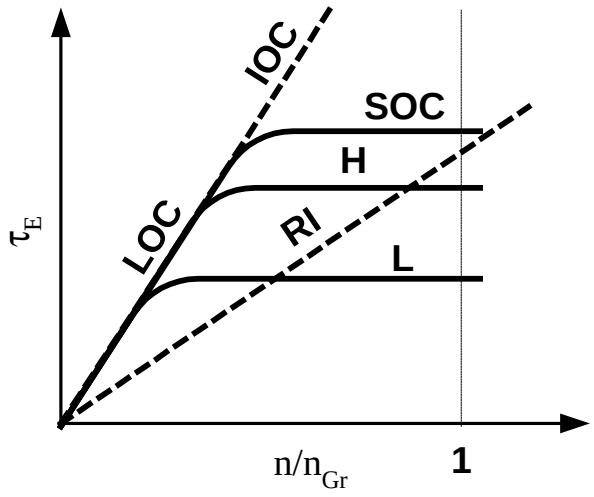

Fig. 2.5 Dependence of the energy confinement on the density in auxiliary heated plasmas for a given current and heating power

In auxiliary heated plasmas it is also possible to obtain the linear dependence of confinement on density with the scaling law being similar to the Neo-Alcator one. It is realised by the seeding of a small fraction of impurities into the plasma [14]. As it is discussed in the paragraph 1.5, the transport in a tokamak is governed by micro-turbulences and the puff of impurities leads to the suppression of the most dangerous one called Ion Temperature Gradient (ITG) instability. Since, this instability is suppressed, the reduction of transport leads to a bifurcation in the confinement and the plasma proceeds into the stage where the energy confinement time depends linearly on the density (see Fig. 2.5). This regime is called the Radiative Improved (RI) mode and characterised by the high radiated power. Due to the confinement degradation with the increased power the line for the RI-mode goes below the LOC-IOC branch, but, on the other hand, allows to obtain the confinement much higher than in the H-mode at densities well above the Greenwald limit. This paper is concentrated on the RI-mode of TEXTOR tokamak. The main features and physical mechanisms of ri-mode will be discussed in the next chapter.

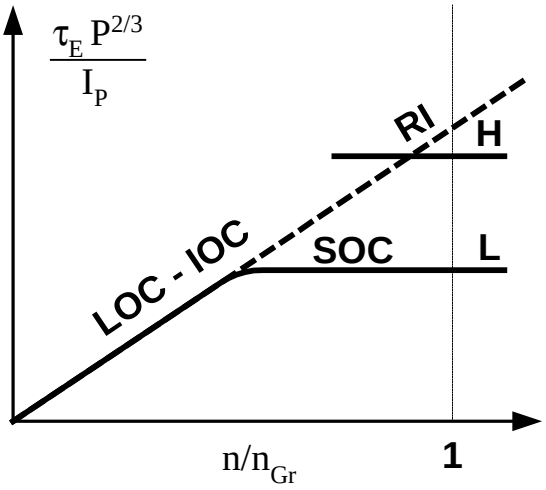

Fig.2.6 Normalised energy confinement time versus Greenwald number

Usually, in order to compare the confinement properties of different modes the diagram for the normalized confinement is used [17] (see Fig. 2.6). This representation form is more convenient because the scaling laws on this diagram are independent of the current and the heating power. Here RI-mode continues the line LOC-IOC for the discharges with additional heating, as well the L-mode demonstrates the same normalized confinement as SOC-mode.

Figure 2.7 shows the normalized confinement diagram for TEXTOR discharges. The confinement in ohmically heated plasmas saturates at densities above 0.6 of the Greenwald limit, following SOC-L-mode branch, whereas in auxiliary heated discharges where also the impurity injection was applied, it was possible to recover the linear scaling of confinement at densities even above n_{Gr}.

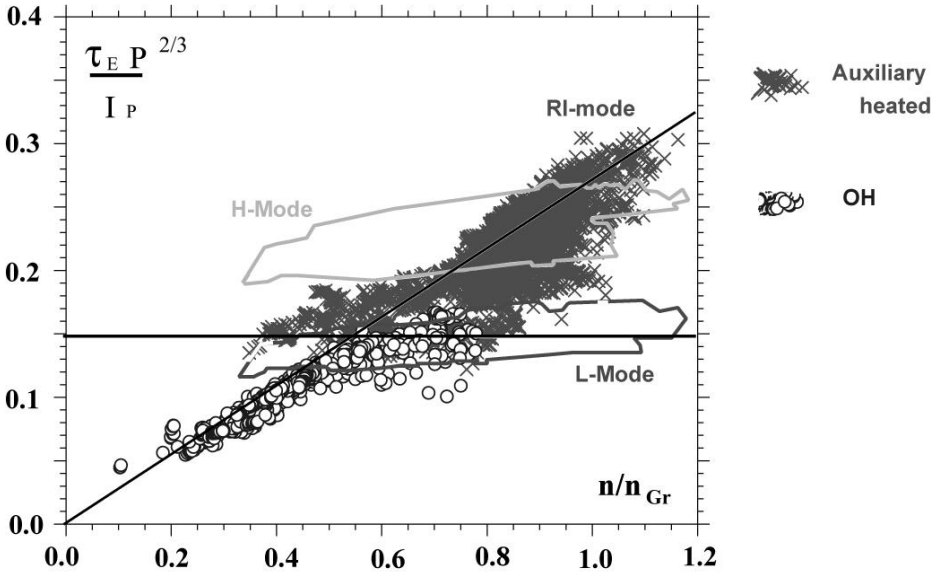

Fig. 2.7 Normalized confinement diagram for TEXTORdischarges [17]

2.7 ITER scalings

Currently the project [15] of the International Thermonuclear Experimental Reactor (ITER) is being under development to show the feasibility to release the fusion power with efficiency necessary for a power plant and to test required technologies. Predictions for the performance of such a machine can be done by the extrapolation of the results from present days experiments. In the database of the existing machines it was found that the dependence of τ_E on two parameters, f_S and f_q, is weak.

$$f_S = 0.3(R/a)^{3/4} R^{1/4} K_X^{1/2}; \qquad f_q = q_{95}/3.2 \tag{2.17}$$

Here K_X is the elongation of separatrix and q_{95} is the safety factor in the point where the poloidal flux is 95% of the flux at the separatrix. In existing tokamaks both f_S and f_q are close to one. In ITER, the values, f_S and f_q, also should be close to those in the present tokamaks. It means that it is possible to extrapolate existing scalings for τ_E to ITER with accuracy given by $f_S^{\alpha_S}$ and $f_q^{\alpha_q}$, where $|\alpha_S| < 0.7$; $|\alpha_q| < 0.15$.

Usually, two ITER scalings, ITERL-89P for the L-mode and ITERH-93P for the ELM-free H-mode, are used [10]:

$$\tau_{ITERL-89P} = 0.048 I_P^{0.85} P^{-0.5} a^{0.3} R^{1.2} B^{0.2} n^{0.1} \sqrt{A_i \kappa} \tag{2.18}$$

$$\tau_{ITERH-93P} = 0.036 I_P^{1.06} P^{-0.67} a^{-0.11} R^{1.9} B^{0.32} n^{-0.17} A_i^{0.41} \kappa^{0.66} \tag{2.19}$$

In order to compare the confinement time obtained in present devices to values predicted for ITER, scientists often use enhancement factors, which quantify the confinement with respect to values given by Eq. (2.18) and (2.19).

$$f_{L89} = \tau_E / \tau_{ITERL-89P} \tag{2.20}$$

$$f_{H93} = \tau_E / \tau_{ITERH-93P} \tag{2.21}$$

2.8 References

1. Shafranov V.D. Plasma Equilibrium in a magnetic field, Reviews of Plasma Physics, Vol. **2**, 103, Consultants Bureau, New York, 1966
2. Fielding S.J., Hugill J. et al Nuclear fusion **17**, 1382, 1977
3. Koslowski H.R. et al., Nuclear fusion **40**, 821, 2000
4. Shuller F.C., Plasma Physics and Controlled Fusion **37**, 135, 1995
5. Lipshultz J., J. Nucear Mater. **15**, 145-147, 1987
6. Rapp J. et al., Nuclear fusion **28**, 2199, 1988
7. Greenwald M. *et al* Nucl.Fusion **28**, 2199, 1988
8. Sauter O. et al., Phys. Plasmas **4**, 1654, 1997
9. Troyon F. et al., Plasma Physics and Controlled Fusion **26**, 209, 1984
10. Ongena G. and Messiaen A., Transactions of Fusion Technology, Vol. **37** Mar. 2000, pp 455-466
11. Kadomtsev B.B., Tokamak plasma: a complex system, Institute of physics publication, Bristol 1992
12. Shimomura Y., Japanese Energy Research Institute, JAERI-M, **87**, 080, 1987
13. Goldston R.J., Plasma Physics and Controlled Fusion **26**, 87, 1984
14. Ongena G et al, Plasma Physics and Controlled Fusion **41**, 379, 1999
15. Aymar R. et al., Nucl.Fusion **41**, 1301, 2001

16. Vries P.C. et al Phys. Rev. Letter vol. **80**, pp.3519, 1998

17. Weynants R.R. *et al* 1999 Nucl. Fusion **39** 1637

Chapter 3

Radiative Improved mode on TEXTOR

3.1 The solution for the power exhaust problem

The power exhaust is one of the major outstanding problems which should be solved in order to achieve a burning fusion plasma. The huge heat flux, foreseen for a reactor size machine, can be dangerous for the plasma facing components and does not allow them to survive for a long time. Developments in two directions should bring a solution for this problem. From one side, new materials that are more resistant to the heat load should be developed. From the other one, the plasma physics should develop discharge scenarios, which allow to reduce the harmful influence of heat fluxes.

The concept of a cold, radiating plasma mantle is considered as a possible solution of this problem (see Fig. 3.1) [1]. Line radiation from impurities injected into the plasma distribute the power over a large area and allow to avoid unacceptable highly localized heat loads to the plasma facing components like limiter or divertor plates.

However, at the same time many other important requirements have to be met: (i) injected impurities should not deteriorate the energy confinement of the target plasma; (ii) impurities should not influence to much the fusion reactivity, i.e. their concentration in the plasma core should be sufficient low; (iii) an efficient helium exhaust should be possible.

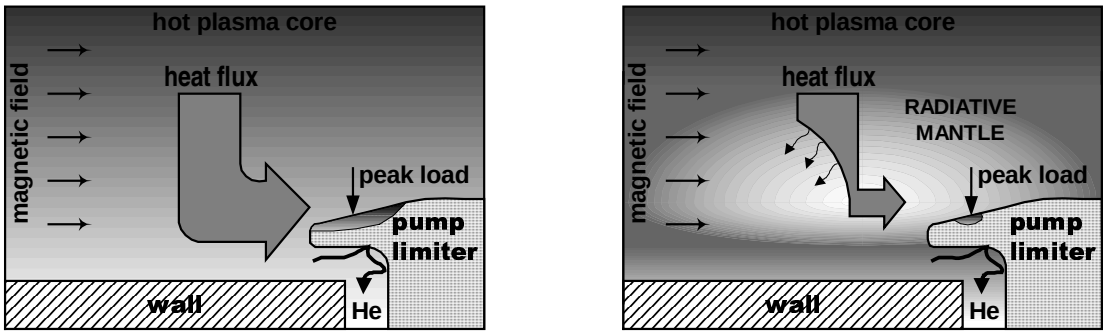

Fig. 3.1 The reduction of the heat flux going to the wall by the creation of the Radiative mantle

The first experiments on the TEXTOR tokamak showed the practicability of the concept of the radiating plasma mantle under quasi-stationary conditions in auxiliary heated discharges. These experiments were performed using neon and/or silicon as the radiating impurity. The radiation was mostly at the edge (see Fig 3.2) and up to 95% of the total input power [2]. At the same time, in contrary to the common belief, the impurity injection does not lead to a deterioration of the energy confinement, but can substantially improve the confinement with an appropriate heating and operational scenario. This regime is called the ***Radiative Improved mode*** (RI-mode).

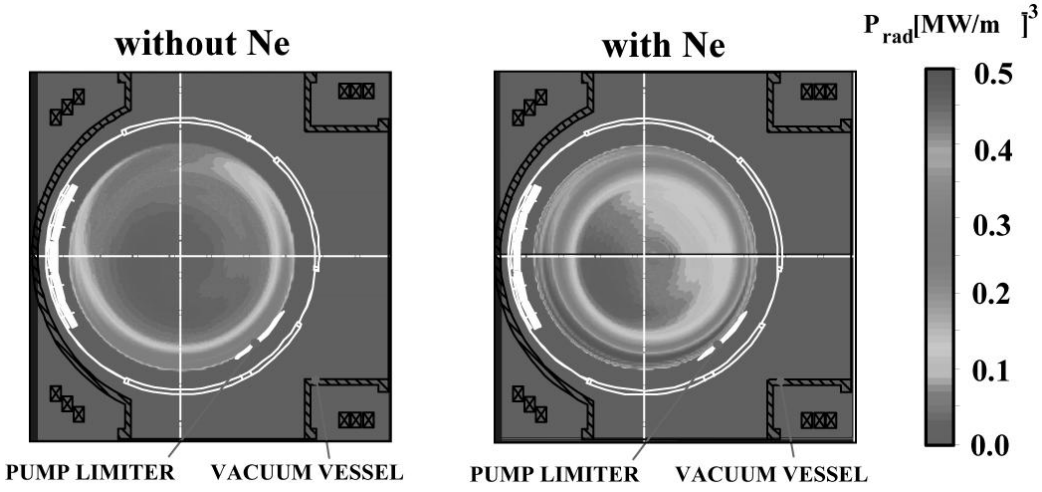

Fig. 3.2 Radiative mantle on TEXTOR created by the puff of small fraction of neon

3.2 Two main scenarios for the RI-mode on TEXTOR

There are two main scenarios to get the RI-mode (see Fig. 3.3) [2,3]. The trajectory **1** schematically represents the scenario where the transition from L to RI-mode occurs as a result of neon injection at high density. The second trace shows the discharge, which from the start follows the LOC-IOC-RI branch while the gas puff rises the density up. Here, the silicon sputtered from the walls is used as the radiating impurity.

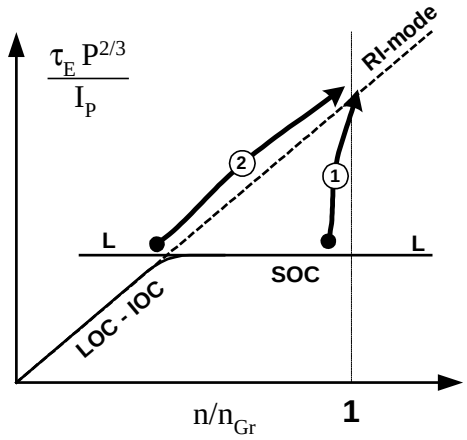

Fig. 3.3 Schematic version of the evolution of discharges with neon injection, 1, and siliconized walls, 2 [3]

Though the final performance resulting from these two scenarios is very similar (see Fig.3.4), since the physical mechanism leading to the confinement improvement in the RI-mode is the same in both cases, the time evolution of discharges is different.

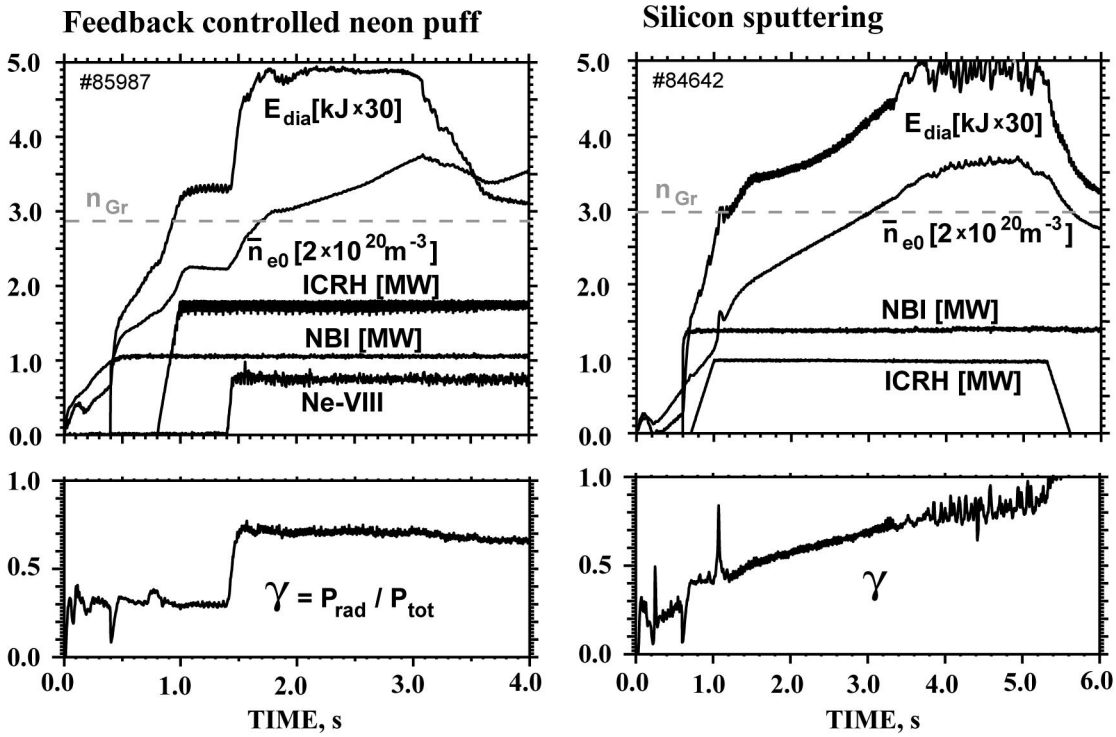

Fig. 3.4 Temporal evolution of density, diamagnetic energy and the fraction of radiated power for two different discharge scenarios

In the discharge on the left side the transition to the improved confinement stage occurs after the neon injection, as it is seen in the sudden increase of the diamagnetic energy. The radiation fraction, $\gamma = P_{rad} / P_{tot}$, being one of the most important parameters characterizing the RI-mode performance, increases during this transition and reaches 70%.

It is necessary to mention, that one of the most salient features of the RI-mode, which also thought to be instrumental in the confinement improvement, is the peaking of the density profile (can be quantified by the ratio of the central to volume averaged density). In the L-mode, before neon is injected, the density profile does not show any tendency to peak. The peaking occurs after the neon injection while the confinement improves [3]. Figure 3.5 shows a typical evolution of the enhancement factor, f_{H93}, versus density peaking factor.

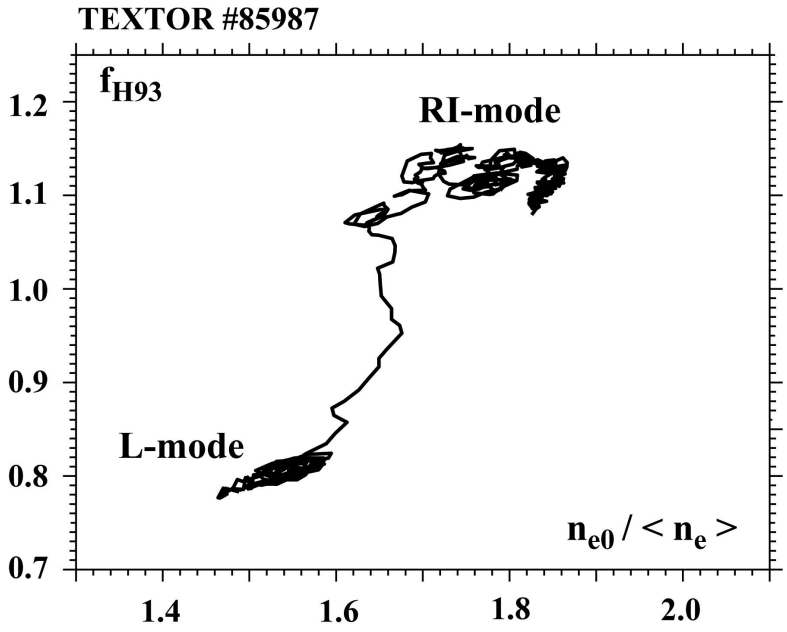

Fig.3.5 Evolution of the confinement properties of the discharge presented in the Fig. 3.4 (left) after the neon injection triggers L-RI transition.

The discharge shown on the right site of Fig.3.4 does not demonstrate a transition like the first one. At any time this discharge does not stay in the L-mode; it evolves along the LOC-IOC-RI line on the confinement diagram. The density profile is highly peaked from the start and does not increase its peaking when the discharge goes to the RI-mode. The diamagnetic energy rises linearly with the density as predicted by the LOC-IOC scaling law, which is also valid for the RI-mode. The radiation fraction in this discharge rises linearly with the density, since impurities are present from the startup, and reaches 80%.

3.3 Attractive features and critical parameters for the RI-mode

The RI-mode experiments have demonstrated the capability of this regime to reduce significantly the heat load to the plasma facing components. However, at the same time the discharges with impurity injection demonstrate a lot of other features needed for the reactor grade plasma [2-4].

A lot of plasma parameters achieved in the RI-mode meet or even overcome the values required for the next step machine called ITER:

- Confinement is that of ELM-free H-mode, the enhancement factor (see equation 2.21) $f_{H93} \geq 1$, the required value for ITER is 1;
- High densities, with a Greenwald number up to 1.4 (the required one ~0.85);
- Radiated power is mostly at the edge and up to 95% of the total input power;
- High normalized toroidal beta (see equation 2.11) β_n is up to 2;
- No significant influence of the seeded impurities on the fusion reactivity;
- Possibility of the long stationary discharge with a duration of up to 7 s or 160 times the energy confinement time.

Figure 3.5 demonstrates that all these advantages can be obtained simultaneously and in stationary state. Such a big number of attractive features has brought the RI-mode to the list of the reactor relevant scenarios.

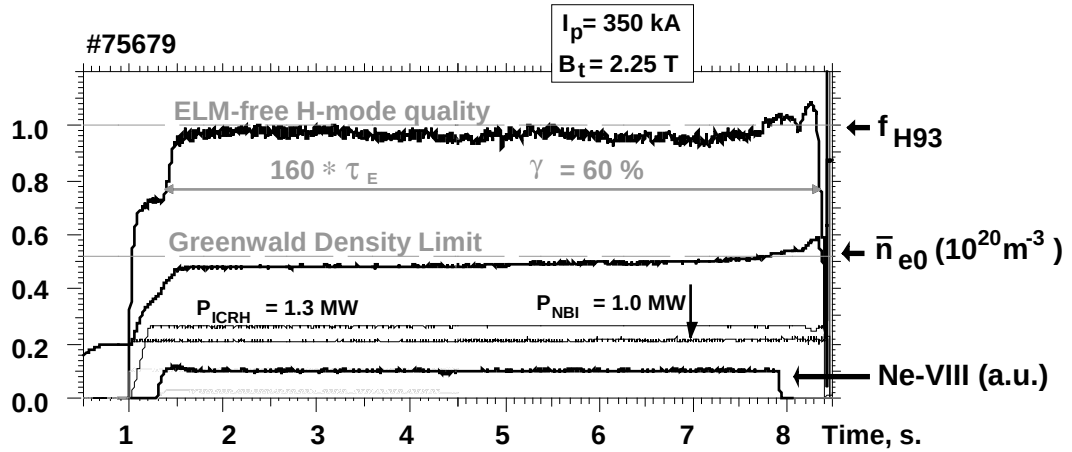

Fig. 3.6 The time traces of f_{H93} enhancement factor, density and additional heating power for the TEXTOR discharge with impurity seeding (shown by Ne-VIII line) where the high confinement achieved concurrently with a high density in a stationary state with a duration of 7s or 160 times the energy confinement time [3].

Although the RI-mode performance has many advantages, to reach those conditions certain number of requirements have to be fulfilled:

(i) a radiation fraction of at least 45-50%;

(ii) a density exceeding 70% of Greenwald limit;

(iii) a deuterium plasma with a minimal co-current deuterium beam injection of 20-25% of the total heating power;

(iv) a low fuelling rate and optimized wall conditions;

(v) an optimum plasma position depending on the current, toroidal magnetic field and heating scenario.

The understanding of the physical nature of these requirements limiting the RI-mode performence is a topic deserving intensive experimental and theoretical studies. The present thesis is concentrated on the limitation imposed by the fuelling rate and the wall conditions.

3.4 The physics of the L - RI-mode transition

3.4.1 drift waves

As was mentioned already in section 1.5, the experimentally measured transport is larger than that predicted by the neoclassical theory. The physics of this high transport, called anomalous, is thought to be based on the particle-wave interactions destabilizing the so-called *Drift Waves*, that finally leads to the grow of the density and potential perturbations.

The physics of the *Drift Waves* can be understood from Fig. 3.7, which shows the poloidal cut of the tokamak plasma. The perturbation of the density,

$$\tilde{n} \sim \exp(-i\omega t + ik_y y)\,, \tag{3.1}$$

leads, due to the Boltzmann distribution, to a perturbation of the potential of the same form,

$$T_e \frac{d\,\tilde{n}}{d\,y} = en \frac{d\,\tilde{\varphi}}{d\,y}. \tag{3.2}$$

The drift velocity in the perturbed electric field is given by the expression:

$$\tilde{V}_x = c\frac{\tilde{E}_y}{B} = -ik_y c\frac{\tilde{\varphi}}{B}. \tag{3.3}$$

The particle drift in different points along the *y*-axis is in opposite directions, that results in the motion of the perturbation as a wave in the y-direction.

The drift waves in the tokamak are the perturbations strongly localized in the minor radius, moving in the direction of the electron drift with the frequency:

$$\omega_* = \frac{cT_e k_{\perp \max}}{eB}\left(-\frac{d\ln n_e}{dr}\right). \qquad (3.4)$$

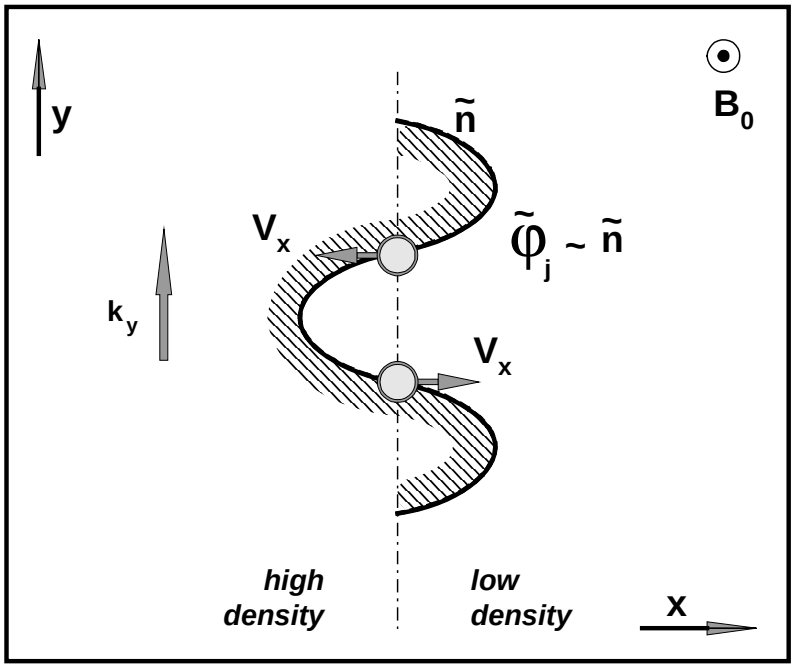

Fig. 3.7 The physical mechanism of the drift wave

In the ideal two-fluid approximation, drift waves does not cause any transport across the magnetic surfaces. But, the dissipation processes, taken into account, can produce the imaginary addition to the frequency ω_*, corresponding to the growth rate of the drift wave.

Here we consider two most known mechanisms for the growth of the drift waves. One is called Dissipative Trapped Electron (DTE) mode [6] and based on the detrapping of the "banana" particles through their collisions. The other one appear if the ion temperature gradient exceeds the certain value, and this mode is called Ion Temperature Gradient (ITG) instability [7,8]. Its mechanism is described in the following section.

3.4.2 Ion Temperature Gradient (ITG) instability

The Ion Temperature Gradient instability is the electrostatic instability driven by the gradient of the ion temperature. Figure 3.8 schematically represents the physical mechanism of the ITG instability. Consider the magnetic surface where the ion temperature, $\tilde{T}_i$, is perturbed as it is shown in the Fig.3.8 (a). That leads to the perturbation of the pressure, $\tilde{P}_i$, and, as a consequence, produces the radial drift driven by the pressure gradient,

$$\tilde{T}_i \Rightarrow \tilde{P}_i \Rightarrow \tilde{V}_{r,P} = c\frac{\nabla_y \tilde{P}_i}{Z_i n_i e B}, \tag{3.5}$$

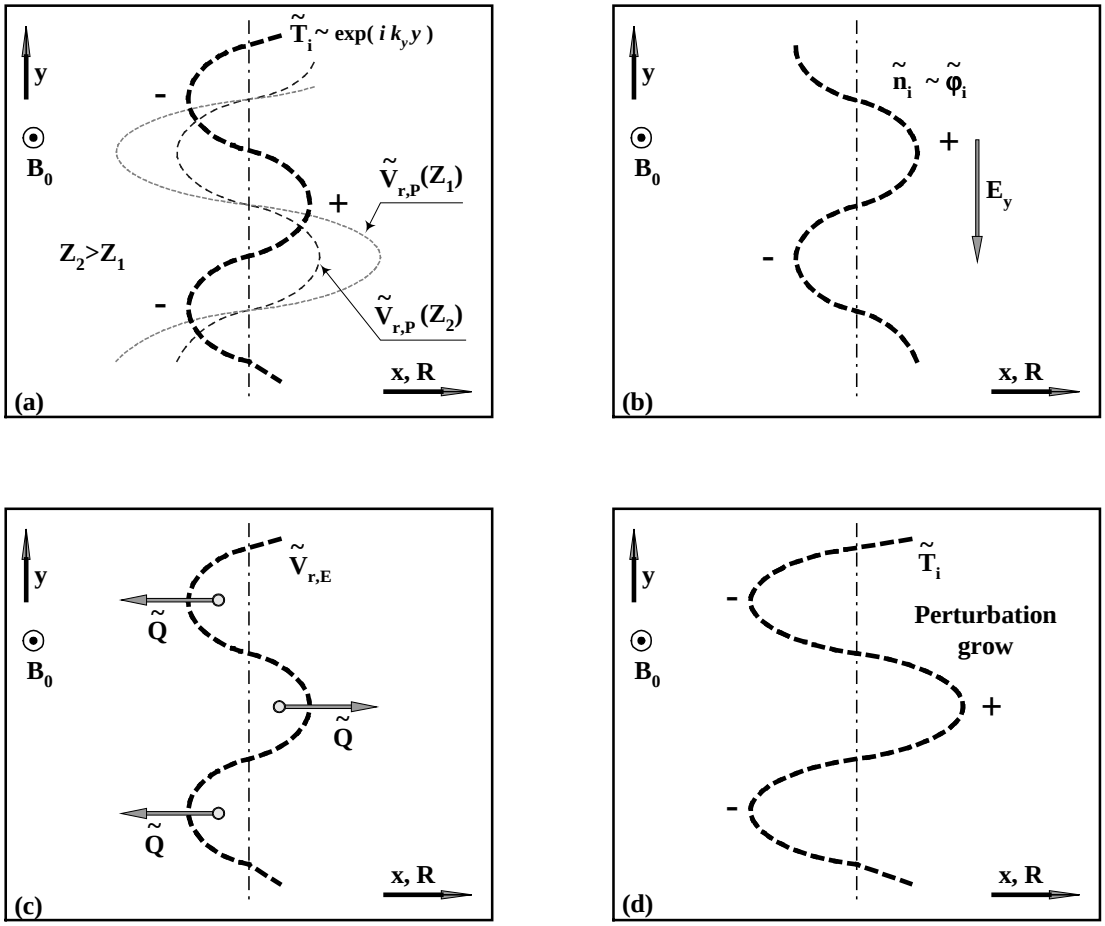

Fig. 3.8 The physical mechanism of the ITG instability

where c is the velocity of light and Z_i is the ion charge. In toroidal geometry $div(\tilde{V}_{r,P}\, n) \neq 0$, i.e. the $\tilde{V}_{r,P}$ drift leads to the perturbation of the ion density and potential, see Fig.3.7(b). According to the Eq. (3.3) the electric potential produces the radial $E \times B$ drift (Fig. 3.8(c)). The heat flow associated with the later,

$$\frac{3}{2}\frac{\partial n_i T_i}{\partial t} = -div\left(-\frac{5}{2} n_i \tilde{V}_{r,E} T_i\right) = -\frac{5}{2} n_i \tilde{V}_{r,E} \frac{\partial T_i}{\partial r} \equiv \tilde{Q}, \tag{3.6}$$

enhances the initial perturbation of the temperature, Fig. 3.8 (c,d).

For the plasma of not very low collisionality, the ITG-mode can be characterized by the individual growth rate [10, 11]:

$$\gamma^{ITG} \approx \frac{cT_e k_\perp^{ITG}}{eB} \cdot \left[\left(-\frac{d\ln T_i}{dr} + \frac{2}{3}\frac{d\ln n_e}{dr} \right) \left(Z_{eff} R \right)^{-1} - \frac{1}{8}\left(\frac{d\ln n_e}{dr} + \frac{2}{R} \right)^2 + \frac{5}{9}\left(\frac{d\ln n_e}{dr} \right)^2 Z_{eff}^{-2} \right]^{1/2}. \tag{3.7}$$

From this formula, it is seen that the growth rate is proportional to the square root of the parameter η,

$$\gamma^{ITG} \sim \sqrt{\eta - \eta_{crit}}\,, \tag{3.8}$$

$$\text{where } \eta = \partial \ln T \,/\, \partial \ln n\,, \tag{3.9}$$

$$\eta_{crit} = \frac{2}{3} + \varepsilon_n \left(\frac{10}{9Z_{eff}} + \frac{Z_{eff}}{4} \right) + \frac{Z_{eff}}{4\varepsilon_n} - \frac{Z_{eff}}{2}, \tag{3.10}$$

$$\text{and } \varepsilon_n = -\frac{R}{2\,L_n}, \quad L_n = \frac{1}{\partial \ln n / \partial r}. \tag{3.11, 3.12}$$

One can see that γ^{ITG} decreases with decreasing η and reduces to zero when η approaches the critical value, η_{crit}. It is, also, seen that this critical level become larger with the growing Z_{eff}.

3.4.3 ITG-mode suppression during L to RI-mode transition

An analysis of TEXTOR data base allows to unify the scalings established for the energy confinement time in RI-mode and LOC modes through a suitable normalization of the discharge parameters, as it is seen in Fig. 2.7 [3]. This led to the idea that in both regimes the transport is governed by the same kind of turbulence and originates from Dissipative Trapped Electron instability, as this instability was identified as the most important one under the LOC conditions [7,8]. It was further conjecture, that the more dangerous toroidal ITG instability, which causes the deterioration of the energy confinement in SOC and L modes, is quenched in the LOC-mode due to a strongly peaked density profile [9-11].

Subsequent theoretical analysis of TEXTOR discharges allowed to show that within the transition from L to RI-mode the ITG-turbulence is quenched over 2/3 of plasma radii. Figures 3.9 (a) and (b) represent profiles of the electron density, η and η_{crit} for one discharge, before and after the neon injection. If one assumes that the individual growth rate for the ITG instability is proportional to the square root of the parameter η (see Eq. (3.8) and [11]), then it can be expected from the profiles of η and η_{crit}, that the impurity seeding results in the strong suppression of ITG instability. It is mainly

caused by a peaking of the density profile and increase of the effective charge, which, both, are instrumental factors for the suppression of ITG turbulence, as it appears from Eq.(3.7).

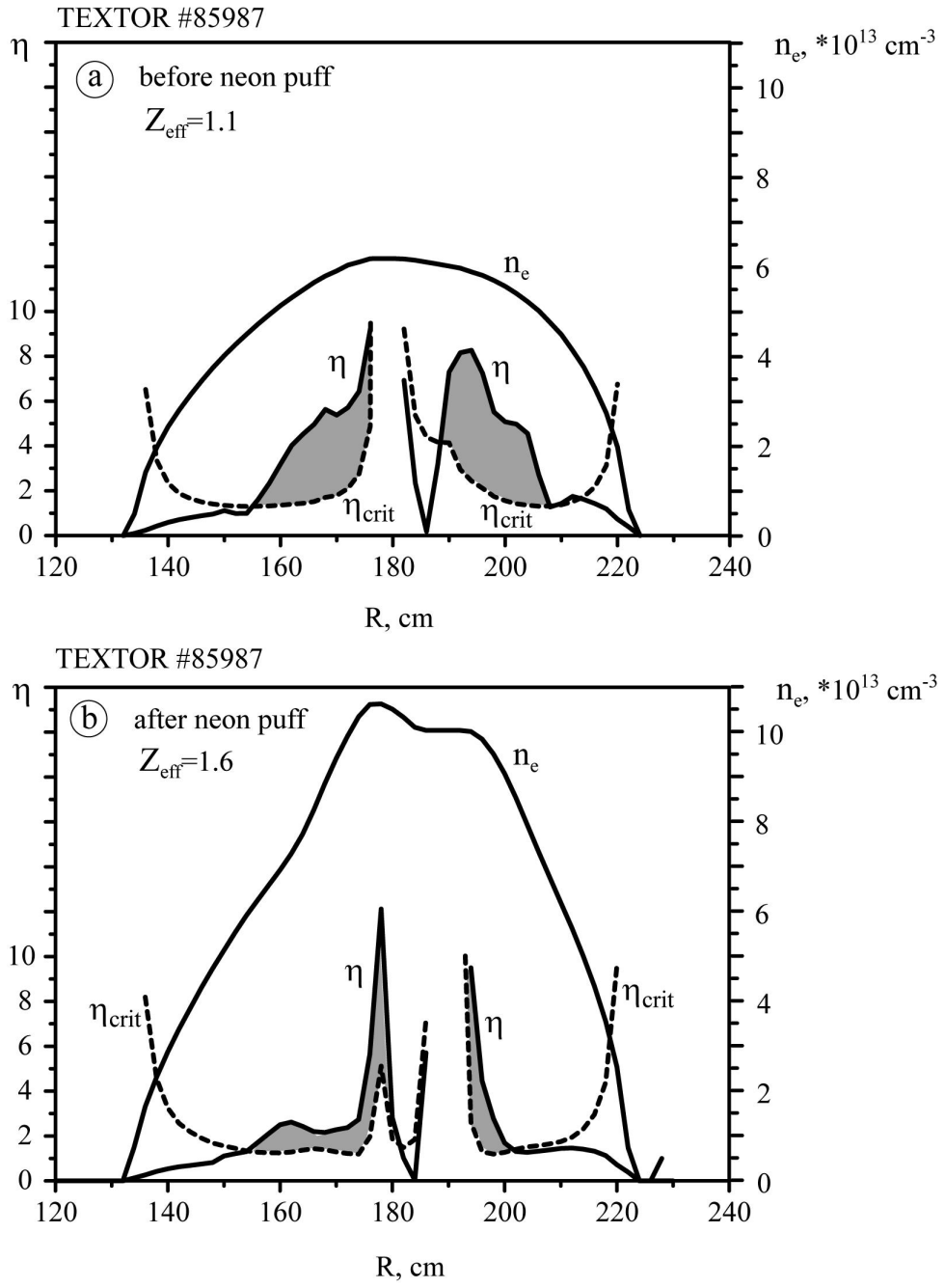

Fig. 3.9 Profiles of electron density, η and η_{crit} for L-mode (before neon puff) and RI-mode (after neon puff)

3.5 Transport model and bifurcation mechanism

The analytical model for anomalous transport, which takes into account contributions from both ITG or DTE instabilities to the convective and diffusive components of the

electron flow, can explain the L-RI transitions as the bifurcation between the plasma states where the transport is governed mainly by ITG and DTE instabilities respectively. This bifurcation is triggered by the increase in the effective charge, which, due to its effect on the anomalous transport coefficients, modifies the electron particle balance. As the result the density profile peaks what helps to suppress completely the ITG turbulence.

For plasmas of not very low collisionality, typical for L and RI-mode regimes, ITG and DTE modes can be characterized by individual linear growth rates, γ [13]. The growth rate for the ITG-mode is given by the Eq. (3.7) and for the DTE by [6]:

$$\gamma^{DTE} \approx f_{tr}\eta_e \frac{\omega_*^2}{\nu_{e,eff}}, \tag{3.13}$$

apparent from Eq. (3.4) it is seen that γ^{DTE} scales as η^{-1}. Here ρ_s is the ion Larmor radius, $\nu_{e,eff} = \frac{1}{\tau_{ei}}\frac{R}{r}$ is the effective collision frequency. The fraction of trapped particles, f_{tr}, is determined by the inhomogeneity of the toroidal magnetic field and by the efficiency of detrapping through Coulomb collisions:

$$f_{tr} = \sqrt{\frac{2r}{r+R}}\ \exp\left[-\sqrt{\frac{qR}{\lambda_e}\left(\frac{R}{r}\right)^{3/2}}\right]. \tag{3.14}$$

Instead of the parameter η, usually used for the ITG turbulence analysis, we use the *peaking factor* $p \equiv \eta^{-1}$. In consideration of typical TEXTOR RI-mode plasmas with $L_n \ll R$ and $Z_{eff} > 2$, it is possible to simplify Eq. (3.7), finally:

$$\gamma^{ITG} \approx \frac{\sqrt{2}cT_e k_\perp^{ITG}}{eBR}\cdot\left[\left(1-\frac{2}{3}p\right)\frac{\varepsilon_T}{Z_{eff}} - \frac{1}{4}\varepsilon_T{}^2 p^2\right]^{1/2}, \tag{3.15}$$

here $\varepsilon_T = -\frac{R}{2\,L_T}$, $L_T = \frac{1}{\partial \ln n/\partial r}$.

The behavior of the peaking factor can be described by the continuity equation for the electron density:

$$\frac{\partial n_e}{\partial t} + \frac{1}{r}\frac{\partial}{\partial r}(r\Gamma) = S_e, \tag{3.16}$$

here, S_e is the electron source due to ionization of deuterium and impurity ions, and Γ is the density of electron flux including contributions from ITG and DTE modes, $\Gamma = \Gamma_{ITG} + \Gamma_{DTE}$, to both diffusive and convective components:

$$\Gamma_{ITG} = -D_{\perp}^{ITG} f_{tr} \left(\frac{\partial n}{\partial r} + \kappa \frac{\partial \ln q}{\partial r} n\right), \tag{3.17}$$

$$\Gamma_{DTE} = -D_{\perp}^{DTE} \left(\frac{\partial n}{\partial r} + \frac{\partial \ln q}{\partial r} n\right), \tag{3.18}$$

This takes into account that the main contribution of ITG turbulence to the particle transport comes from stochastization of orbits of trapped electrons and should therefore be proportional to their relative abundance f_{tr} [13]. The small factor $\kappa = \frac{4r}{3R}$ reflects a relatively weak effect on convection of instabilities caused by ion dynamics, in particular, ITG instability [11,21].Characteristic values of the transport coefficients can be estimated in the mixing length limit, $D_{\perp} \propto \gamma_{\max} / k_{\perp,\max}^2$ [11], where $\gamma_{\max}$ is the maximum growth rate of the relevant unstable mode and $k_{\perp,\max}$ is the perpendicular wave number at which this maximum is achieved, and $k_{\perp,\max}^{ITG} \approx 0.3/\rho_s$, $k_{\perp,\max}^{DTE} \approx 1/\rho_s$.

Integral of equation (3.16) results in an equation for the local peaking factor, *p*:

$$G(p) \equiv \Gamma - \frac{1}{r}\int_0^r \left(S_e - \frac{\partial n_e}{\partial t}\right) r\, dr = 0\ , \tag{3.19}$$

with the help of Eqs. (3.13-3.18) one gets:

$$n_e \left[\left(-\frac{p}{L_T} - \frac{4r}{3R}\frac{\partial \ln q}{\partial r}\right) f_{tr} D_{\perp}^{ITG}(p) + \left(-\frac{p}{L_T} - \frac{\partial \ln q}{\partial r}\right) D_{\perp}^{DTE}(p)\right] - \frac{1}{r}\int_0^r \left(S_e - \frac{\partial n_e}{\partial t}\right) r\, dr \equiv G(p) = 0 \tag{3.20}$$

The bifurcation mechanism (at a given radius) can be explained from the *N*-shape of G(p) function and positions of minimum and maximum of it with respect to zero. Figure 3.10 shows G(p) calculated for the conditions pertaining to 3 times during L-RI transition at 2/3 of the minor radius, where the change in the density gradients after the impurity puff is most pronounced. The value of the peaking factor at a given time corresponds to the points where the function G(p) reduces to zero. The number of such states is determined by the position of G^{max} and G^{min}, with respect to zero level.

In the case of an the L-mode state the positions of minimum and maximum are such that $G^{min} \le 0 \le G^{max}$, and there are three possible solutions, ***a***, ***b*** and ***c***. The solution ***a*** with the minimal **p** is realised since there is no density peaking observed before neon is injected. An increase of Z_{eff} with a puff of impurities causes a reduction of the transport governed by the Ion Temperature Gradient instability, as is apparent from Eq. (3.7), and G^{max} decreases. At the same time the solution moves along the zero line in the direction of high peaking up to the position ***d*** where only one crossing point

with zero remains on the ITG branch of the curve. When G^{max} becomes negative, only a single solution ***e***, on the branch of DTE, remains, where the density peaking is high. This state corresponds to the RI-mode. During the further evolution, the plasma remains in the RI-mode stage and finally settles in the state ***f***.

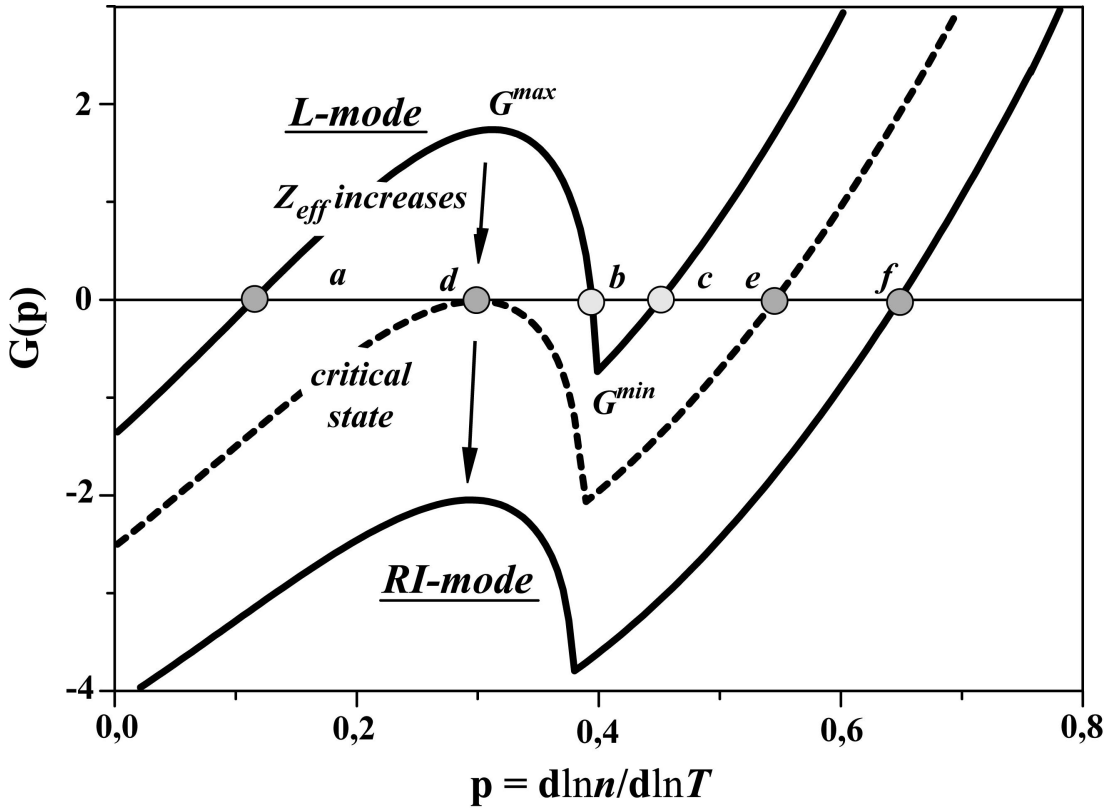

Fig.310 The G function versus the peaking factor p for L and RI-mode at 2/3 of plasma radius

The evolution of the local confinement properties and the effective charge, during the bifurcation process in Fig. 3.10, are shown in Fig. 3.11. At the low peaking factor corresponding to the solution ***a*** in Fig.3.10, the high transport, governed mainly by ITG-turbulence, imposes the low quality of confinement. An increase of the effective charge, after the neon puff, leads to the reduction of ITG-induced transport with a simultaneous increase of the peaking factor. It results in the improvement of the local confinement by a factor 2. When Z_{eff} reaches its critical value, solution ***d*** in Fig. 3.10, the bifurcation into the state ***e*** occurs. During the bifurcation, the effective charge does not change, and the final suppression of the ITG-turbulence occurs on account of increasing peaking factor. Since the ITG-instability is disabled after the bifurcation, the transport is governed by DTE-turbulence alone. It explains the linear degradation of the confinement with the peaking factor while the discharge goes into the stationary state. Finally, the plasma settles in the state ***f*** where the local confinement is by a factor 8 higher than it was before the neon injection (the state ***a***).

The density peaking and the increasing Z_{eff} are the key factors in understanding the transition from L to RI-mode. As it is seen from the Fig. 3.9, the density profile, before the neon puff, does not demonstrate any peaking at all and the value of the

effective charge is low, about 1.1. The injection of neon leads to an increase of the impurity content of plasma, Z_{eff}=1.6, and strong peaking of the density profile.

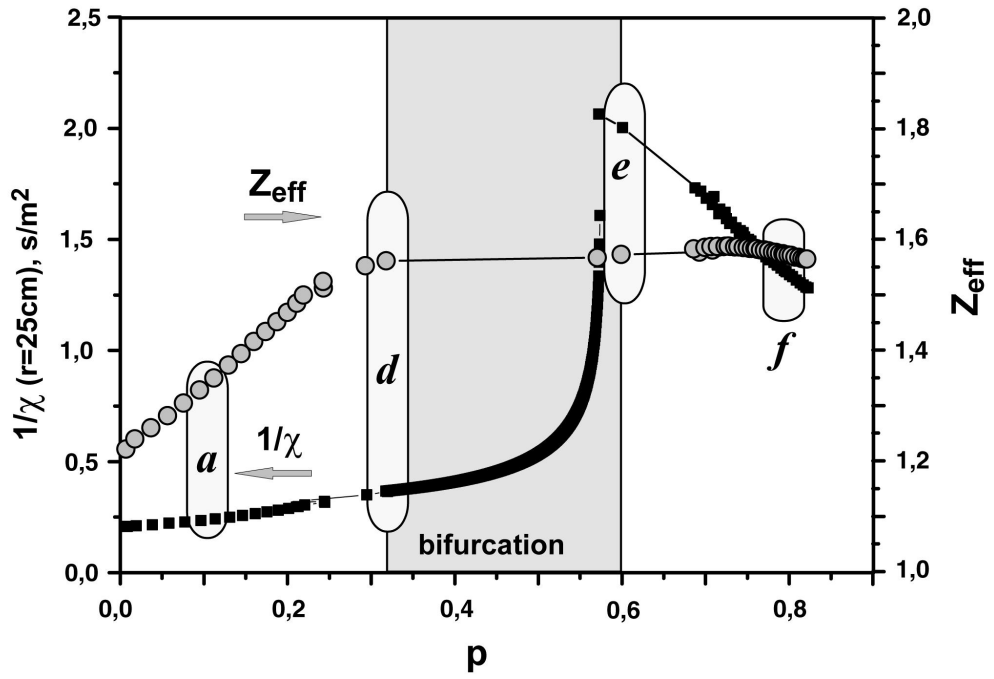

Fig.3.11 Evolution of the local confinement properties during the bifurcation process

The evolution of the density peaking factor, quantified by the ratio of the central to the volume averaged density,

$$\gamma_n = \frac{n_{e0}}{< n_e >} \quad , \tag{3.21}$$

and line-averaged Z_{eff} versus the Greenwald number during the L-RI transition, is shown in Fig. 3.12. Though γ_n is a global parameter and is not an averaged value of *p*, therefore it is proportional to an averaged gradient of density and should evolve similarly to *p*. During the L-mode, before the neon injection, the line averaged density increases while the shape of the density profile, characterized by the peaking factor, does not change. After the neon injection, the value of the effective charge increases significantly. Simultaneously the density profile starts to peak. At densities about 0.9 of n_{Gr} the saturation of Z_{eff} occurs and bifurcation to the RI-mode starts. This bifurcation occurs only on account of density peaking while Z_{eff} is constant. Finally, in the RI-mode, the values of the Z_{eff} and peaking factor are high that results in significantly reduced ITG-instability and confinement improvement.

Figure 3.13 (left), schematically represents the evolution of the density profile and corresponding ITG-induced diffusion. At the certain radius, during the bifurcation the total electron flux, Γ, including the contributions from ITG and DTE modes, changes so that the diffusive component of flow governed mainly by ITG-turbulence decreases with respect to the convective part. The dominance of the convective flux leads to the peaking of the density profile and to the further suppression of ITG turbulence,

mainly through the last term in γ^{ITG} being non-linear with respect to the density gradient. With time, this combination of density peaking and turbulence suppression penetrates deeper into the plasma, it also can be seen from an experimental evolution of the density profile, Fig. 3.13 (right).

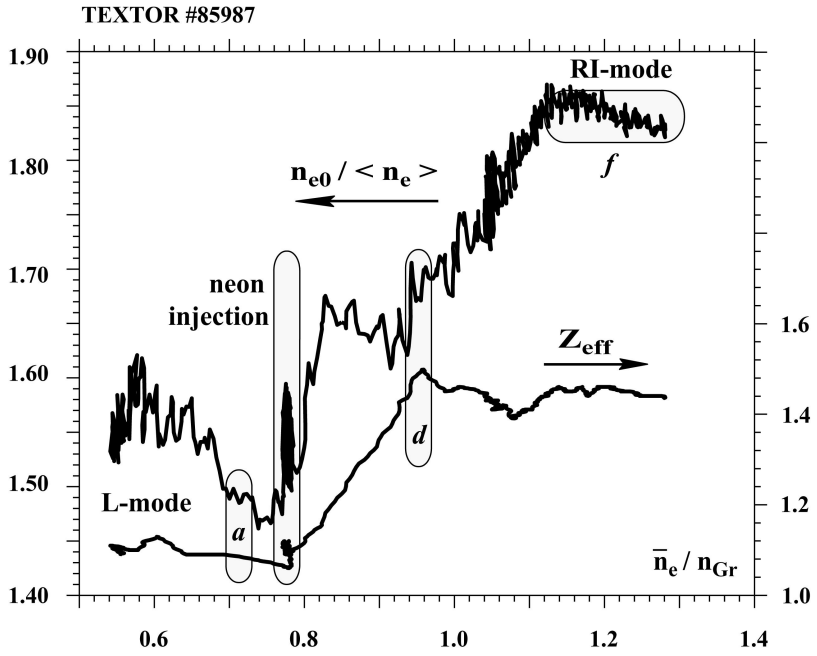

Fig 3.12 The evolution of the density peaking factor and Z_{eff} versus Greenwald number during the L-RI-mode transition.

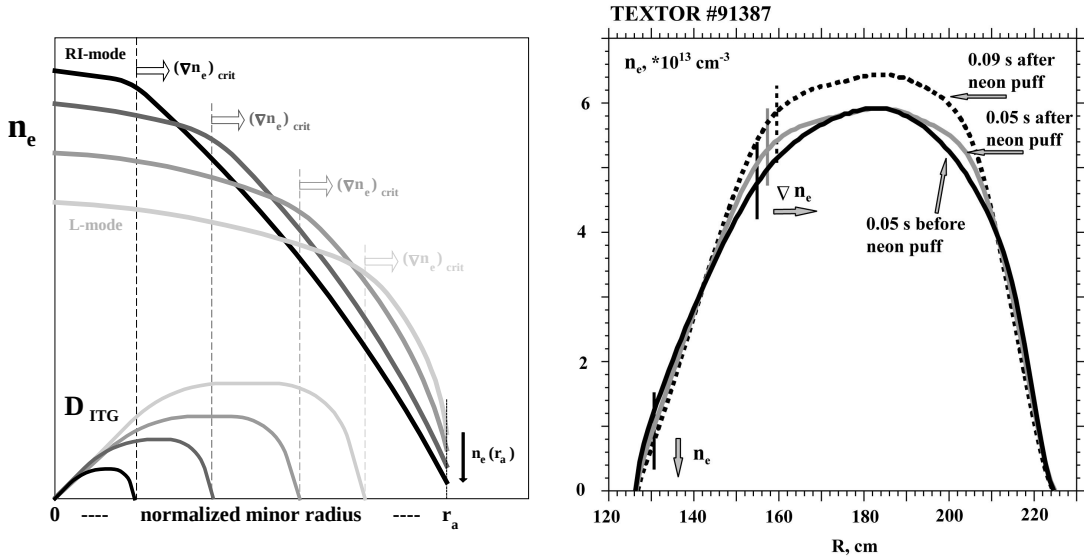

Fig. 3.13 Schematic representation of the evolution of the density profile and ITG-induced diffusion, during L-RI transition, following from the bifurcation model (left), and comparison to the experimental evolution of the density profile after the neon injection (right).

3.6 Trans Greenwald densities in RI-mode discharges and confinement deterioration

A subject of intense investigations in present day fusion research is the development of an operational scenario, providing at the same time (i) high confinement with at least H-mode quality (see Eq.(2.19)) and (ii) high densities around or above the empirical Greenwald limit (see paragraph 2.2 in this thesis). During past years a big success has been achieved by adjusting of deuterium fuelling and pumping and by optimizing of wall conditions [14,15]. Recently, this subject was studied in TEXTOR in discharges with impurity seeding. As it is seen from Fig. 3.14, by injection of deuterium gas it was possible to achieve densities of 1.4-1.6 of Greenwald limit. The data in this diagram, obtained in discharges with silicon sputtering, illustrate three types of behaviour depending on the fuelling rate:

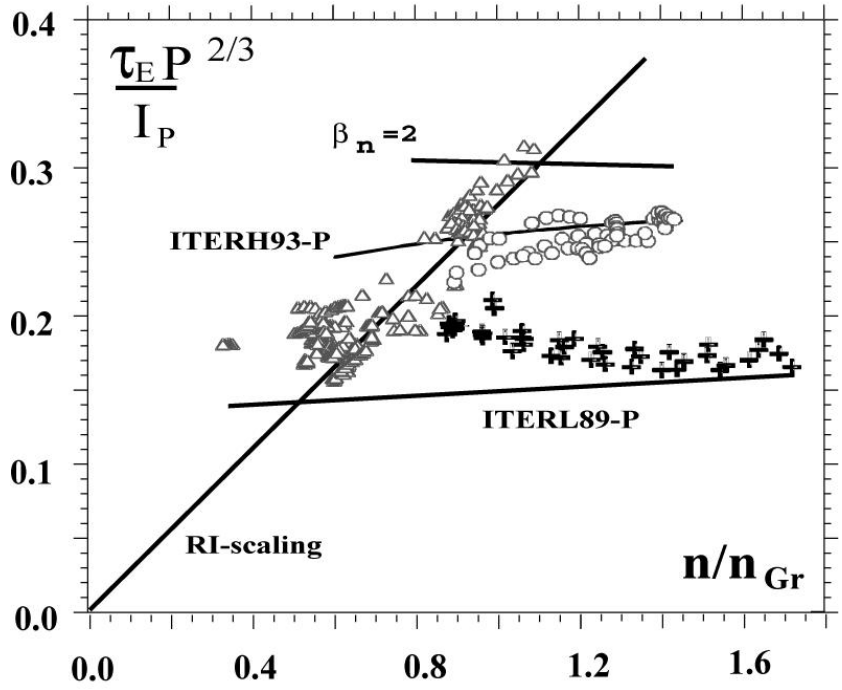

Fig. 3.14 Statistical normalized confinement diagram for discharges with a gas puff [14]

(i) The triangles correspond to the discharges where the confinement follows the RI-mode scaling

$$\tau_{RI} = k\,\bar{n}_{e0}\,P_{tot}^{-2/3}, \tag{3.22}$$

where k is the coefficient about 1.8, P_{tot} is the total heating power in MW and $\bar{n}_{e0}$ is the central line averaged density in 10^{20} m^{-3} [2,3]. For these discharges a very low (of about $1*10^{21}$ D/s) D_2 gas puffing or no gas puffing at all was applied. The maximum achievable confinement is limited by the β-limit (see

section 2.3), β_n=2. The later also imposes a limit for a maximum obtainable density, $n/n_{Gr}\approx 1.1$.

(ii) The crosses correspond to discharges where the strong gas puff was applied. Here, the intensity of the gas puff is about $2*10^{21}$ D/s. That allows to obtain a very high densities with the Greenwald numbers of order 1.4-1.6. However, such a strong gas puff leads to the progressive confinement deterioration towards L-mode.

(iii) The third cluster of points, represented by cycles, corresponds to the discharges where the confinement obtained at high densities is saturated at the intermediate level between L and RI-mode and being nearly the H-mode quality. The gas puff rate in these discharges is moderate with respect to the second group but slightly higher than in the discharges following the RI-mode scaling.

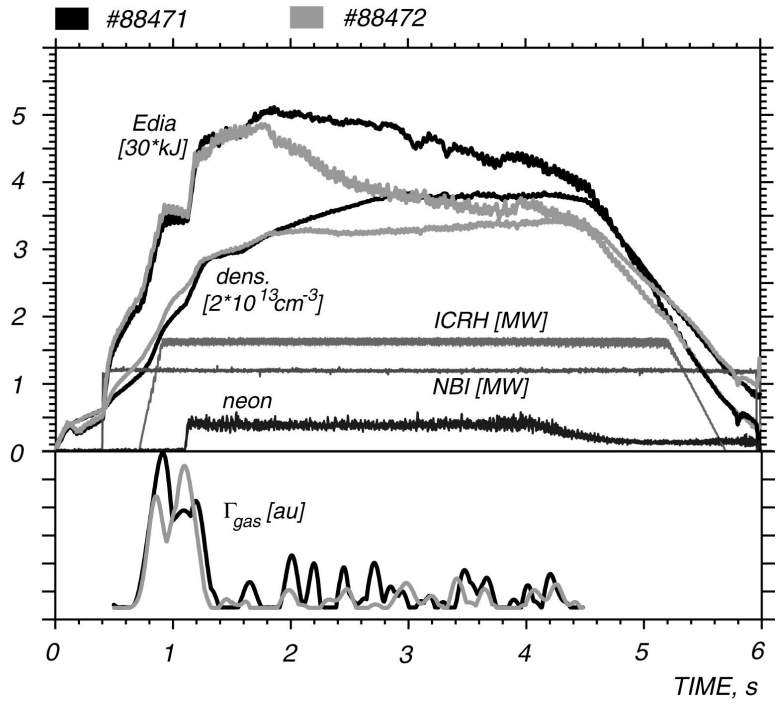

Fig.3.15 Deterioration of confinement due to not optimized wall conditions

Thus, the quality of the obtained confinement depends on the gas puff intensity. Only the moderate gas injection allows to maintain the confinement of the H-mode or higher quality. But it is not possible to define inflexible ranges for intensity of the gas puff corresponding to the certain confinement quality. In some of the discharges the deterioration of confinement occurs, even, with the low gas puff, but if the walls contain a lot of gas from the previous shot. Figure 3.15 compares two discharges at the same gas puff but with different wall conditions. The discharge #88471 demonstrates the confinement of the H-mode quality with a slight progressive confinement deterioration during the gas puff phase. The same, or even lighter, gas

injection in the following discharge (#88472) leads to much stronger degradation of the diamagnetic energy. That occurs as the result of the strong gas influx coming from the walls saturated by the gas during the first shot. In order to recover the performance obtained in the shot #88471, it is necessary to make a low-density discharge, without impurity seeding, which takes the superfluous gas out from the walls.

Thus, the best performance is obtained in discharges combining the careful tailoring of the gas injection and optimized wall conditions. The strong gas injection allows to obtain densities much above n_{Gr} if the MARFE formation is avoided but the price is strongly degraded confinement of the L-mode quality.

3.7 Evolution of different plasma core parameters in discharges with different fuelling rate

Figures 3.16 [a,b] presents two discharges differing in the intensity of the gas puff. The position of the gas inlet is above the equatorial plain at the low field side. The total auxiliary heating is 2.4 MW and produced by the NBI and ICRH heating systems. The neon puff from 1.4 to 5 s is indicated by the brilliance of the NeVIII line. The gas puff, through the main gas inlet, rises the plasma density up. The intensity of fuelling is controlled by automatic with a feedback to the value of density. It stops at the time of 1.8 s, when an additional puff of various intensity is applied.

In both discharges, the injection of neon was applied, that triggers the transition into the improved confinement state, where both of compared discharges demonstrate the same plasma performance. In the discharge #85986 (solid curves) a strong deuterium puff was applied. It results in a significant deterioration of the energy content in the plasma and confinement rollover towards L-mode (see Fig. 3.16[b]). At the same time the content of neon particles in the plasma volume was drastically reduced such that the effective plasma charge, Z_{eff}, was decreased to its L-mode level ($Z_{eff}\approx1.1$).

Conversely, a less intensive gas puff in the discharge #85984 (see Fig. 3.16 [a,b], dashed curves) allowed to preserve the energy confinement of the RI-mode quality, with the confinement time being proportional to the density (see Eq. (3.22)), which rises significantly above the H-mode level at densities exceeding n_{Gr}. The line averaged density achieved in this discharge is 10% higher than in the previous one and limited by the β-limit. Also, the value of the effective charge in this shot is not deteriorated by the gas injection and typical for the RI-mode, Zeff≈1.8. Finally, this discharge arrived at the β-limit, where the MHD activity sets in and the back transition in the energy confinement occurs.

One of the most salient features of the RI-mode is the high peaking of the density profile. An evolution of the density peaking factor versus the Greenwald number, for compared discharges, is shown in the Fig 3.17. It is seen that the neon injection, in both of the discharges, leads to the peaking of the density profile. This peaking increases while the density rises up to the Greenwald density, where the deuterium injection is applied. For the discharge with the low gas puff this peaking increases further up to a very high value. The final density profile, just before the β-limit is achieved, is shown in Fig. 3.18 (dashed curve). It is characterized by very strong

gradients being of principle important for the RI-mode behavior. The value of γ_n is close to 2.0.

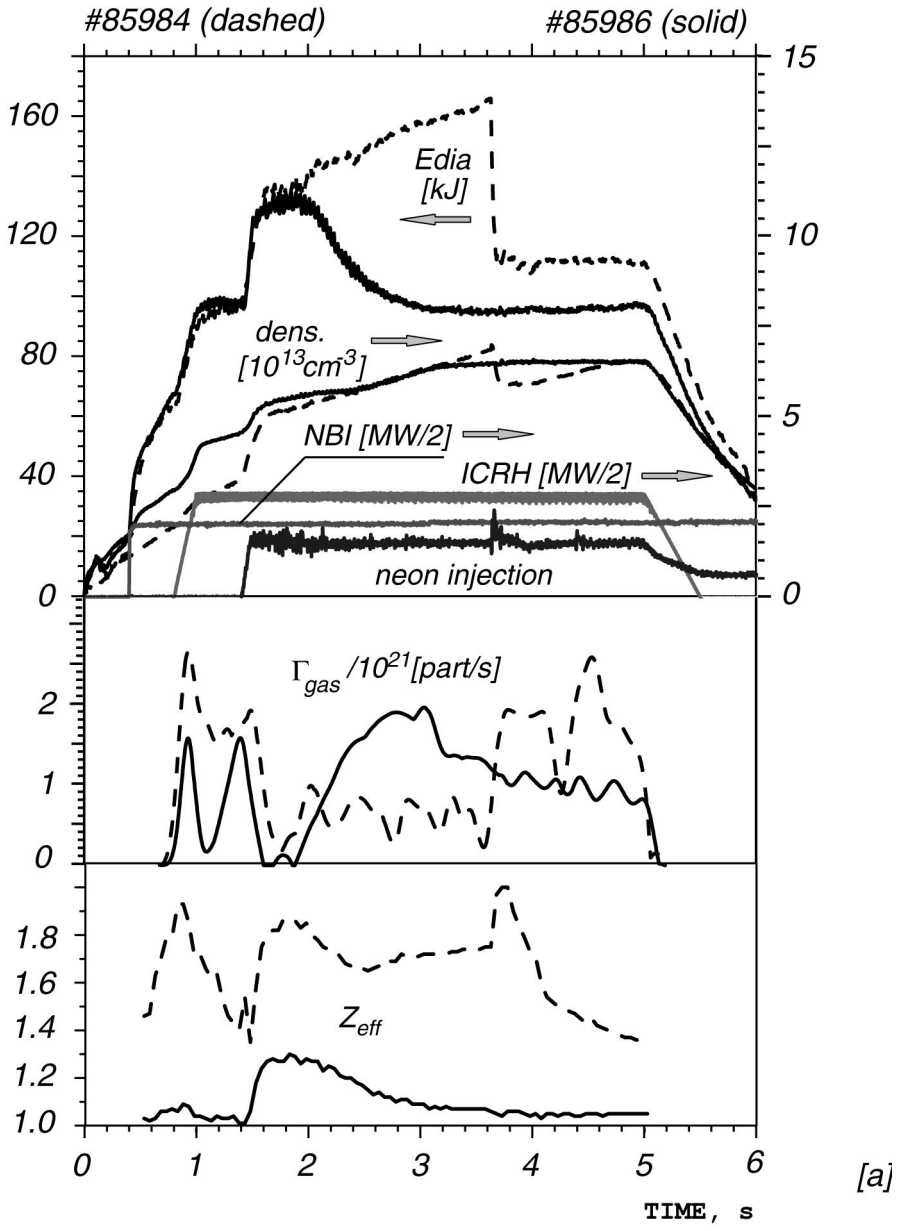

Fig.3.16 [a] Two discharges differing by the gas puff rate: 85984 (dashed curves) – low gas puff, 85986 (solid curves) – strong gas puff. Time traces for diamagnetic energy, the line averaged electron density, ICRH and NBI heating, Ne-VIII line, gas influx and Z_{eff}.

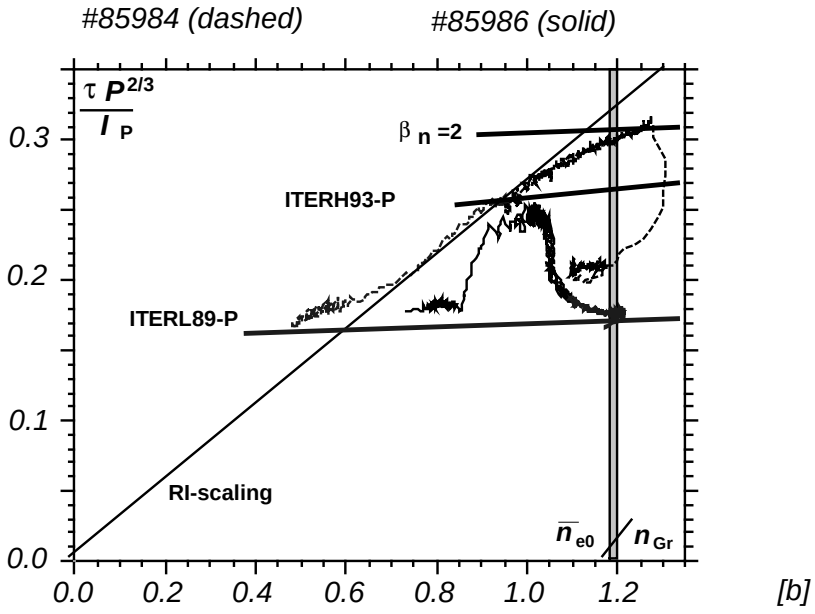

Fig. 3.16 [b] Evolution of discharges shown in Fig 3.16 [a] in the normalized confinement diagram.

Strong gas puff in the discharge #85986 interrupts the peaking of the density profile, observed after the neon injection, and leads to a significant flattening of the profile. The value of γ_n progressively decreases towards the level observed before the neon injection. The shape of the density profile after the rollover, Fig. 3.18 (solid curve), is typical for the L-mode where strong gradients exist only close to the plasma edge.

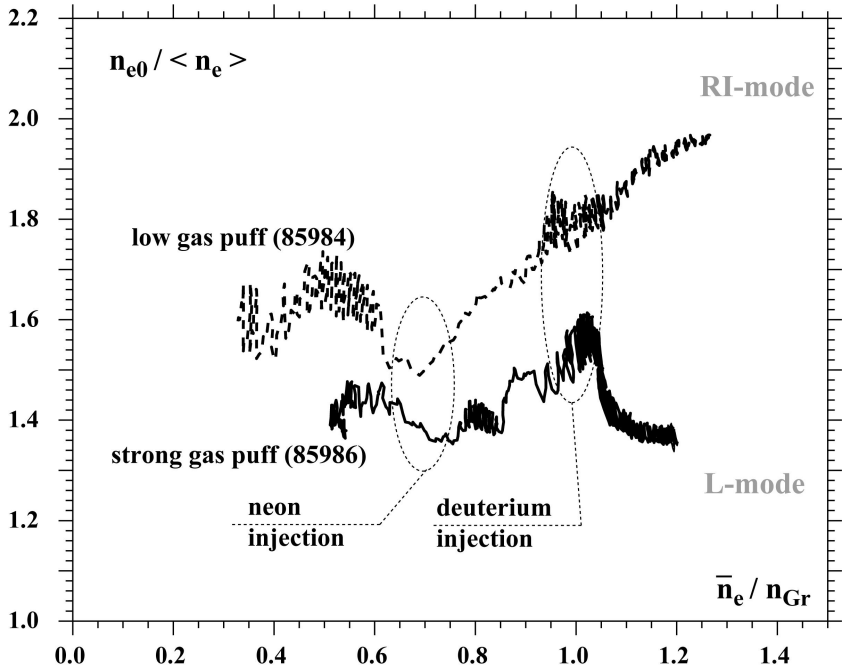

Fig. 3.17 Evolution of the density peaking factor versus Greenwald number for discharges shown in Fig 3.16 [a,b]

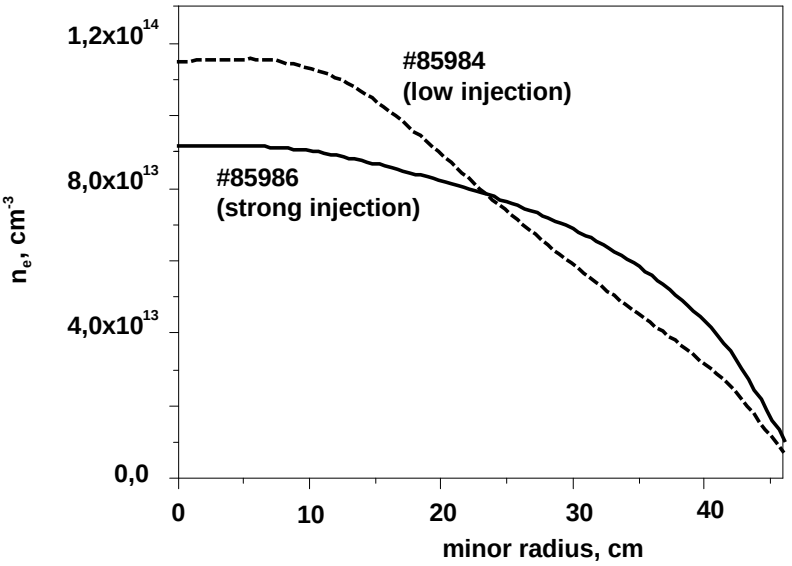

Fig. 3.18 Density profiles of the compared discharges taken after the deuterium injection at the same line averaged density, $n/n_{Gr}=1.2$ (see Fig. 3.16 [b]).

3.8 Edge parameters behavior with different gas puff rate

Understanding of the influence of the edge parameters on the global plasma properties is important subject among those permanently attracting attention in current research program [16]. Furthermore, experimental observations from different tokamaks and numerical simulations demonstrate an important role of the edge conditions dictating the global energy and particle confinement. In particular, a back transition from the high (H) confinement to the low (L) confinement mode has been observed in the divertor tokamaks JET [13], DIII-D [19], ASDEX-U [20] during a strong gas puff.

On TEXTOR tokamak, a strong correlation of the plasma edge parameters with the obtained performance is observed in impurity seeded plasmas where the confinement deterioration was triggered by the strong deuterium puff.

Figures 3.19 and 3.20 display the electron density measured with the He-beam at the LCMS (*Last Closed Magnetic Surface*) and neutral pressure at the wall as a function of the Greenwald number [17], where the different symbols indicate the confinement properties with respect to the value given by the Eq. (3.22). It is seen that the edge parameters have a clear correlation with the global plasma performance. High performance, with the energy confinement time being at least 80% of the value predicted by the RI-mode scaling, at high densities is characterized by the low density at the LCMS and by the low neutral pressure at the wall. In discharges where the gas injection triggers the confinement deterioration, the edge density rises significantly faster than the line-averaged one and can be up to a factor of 1.7 higher than in

discharges with the same line-averaged density but where the moderate gas injection does not lead to the degradation of the confinement.

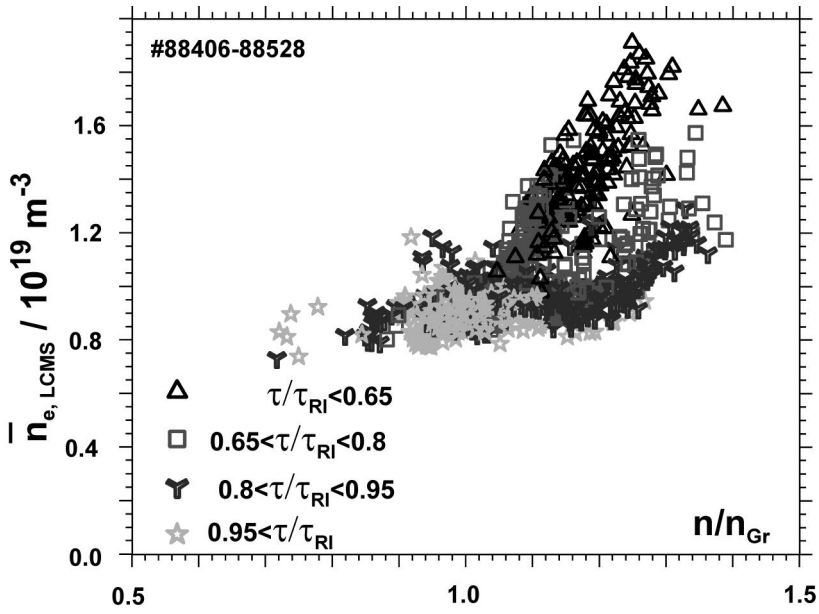

Fig. 3.19 Correlation of the electron density measured at the LCMS with the obtained performance

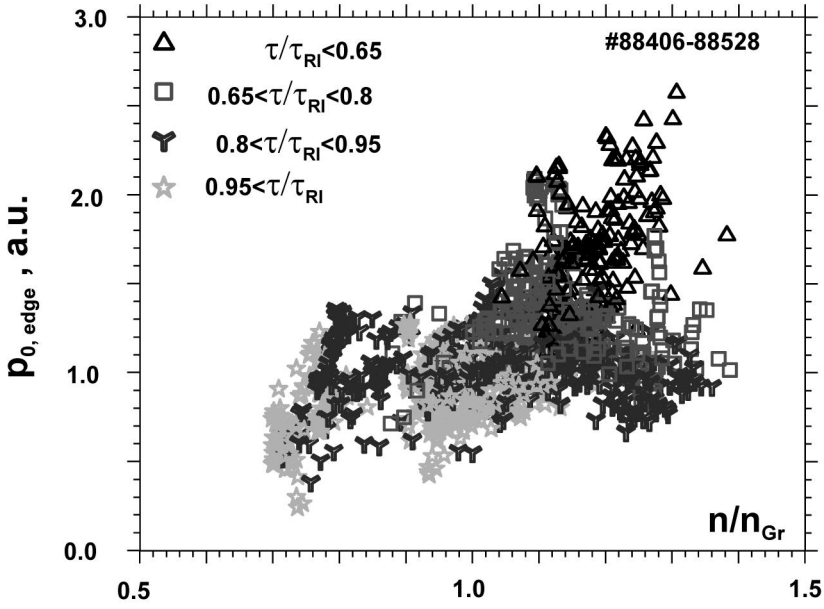

Fig 3.20 Correlation of the neutral pressure at the wall with the obtained performance

Usually, an increase of the edge density and the neutral pressure can be expected after the reduction of the core confinement (e.g. due to MDH). However, the inverse link between the core confinement and the neutral pressure at the edge is also possible. A strong gas puff, although it is always less than 5% of the recycling flux, can lead to

the significant modification of the plasma boundary, increase of $p_{0,edge}$ and recycling flux. Such changes can effect the density profile, the peaking factor decreases, and the deterioration of the core confinement occurs. The relevance of the second scenario can be proved by the fact, that it is possible to use a feedback control of the gas puff rate in order to adjust the confinement degradation [18].

3.9 Questions posed from the “gas puff” experiments

Experiments with different fuelling rates, presented in this chapter, demonstrate a clear correlation between the intensity of the gas puff and obtained performance. At the same time the physical picture of the mechanism leading to the deterioration of the confinement caused by the strong neutral injection is not completely clear at the moment. There are several major questions:

The transport model described in the section 3.5 explains the transition from L to RI-mode as a bifurcation between the plasma states, where the transport is governed mainly by the ITG and DTE modes, respectively. The high value of the effective charge, emerging after the neon puff, is a trigger for such a bifurcation. Can the same model be used to explain the effect of the gas puff on the core confinement, especially by taking into account that a strong reduction of the Z_{eff} is observed in discharges where the confinement properties were destroyed by the gas puff?

Whereas the confinement degradation caused by a strong gas puff, is clearly correlating to the processes at the plasma edge, the linkage between the edge properties and the core confinement is not clear.

The fact, that the neutral flux produced by the gas puff is always less than 5% of the total recycling flux indicates that, probably, the local effects are important. As we shall see, such effects can not be introduced into the present model, as it is one-dimensional. The model should try to explain the “gas puff “ effect based on the processes averaged on the magnetic surface, assuming that the local effects can enhance the transport processes.

The next chapter presents the results of the modeling activity performed to tackle the questions formulated above.

3.10 References

1. Unterberg B. et al Plasma Phys. and Control. Fusion **39**, b189, 1997

2. Messiaen A. et al 1999, RI-mode confinement and performances on

   TEXTOR-94 under siliconized wall conditions, 26th EPS, Maastricht

3. Weynants R.R. *et al* 1999 Nucl. Fusion **39** 1637

4. Ongena J. et al Plasma Phys. and Control. Fusion **41**, a379, 1999
5. Messiaen A. et al Comments onPlasma Phys. and Control. Fusion **18**, No.4 pp221-234, 1997
6. Kadomtsev B.B. and Pogutse O.P 1971 Nucl. Fusion **11** 67
7. Romanelli F. et al 1986 Nucl. Fusion **26** 1515
8. Dominguez R.R. and Waltz R.E. 1987 Nucl. Fusion **27** 65
9. Nordman H. *et al* 1990 Nucl. Fusion **33** 983
10. Tokar M.Z. *et al* Plasma Phys. and Control. Fusion **41** L9 1999
11. Tokar M.Z. *et al* 2000 Phys. Rev. Lett. **84** 895
12. Kalupin D. et al 2000, Evolution of electron density, temperature and pressure profiles in the RI-mode of TEXTOR-94, 27th EPS, Budapest
13. Horton W *et al* 1985 Plasma Phys. Controll. Fusion **27** 937
14. Mank G. et al., Phys. Rev. Letters **85**, No 11, 2312, 2000
15. Maingi R. et al., Phys. Plasmas **4**, 1752, 1997
16. Unterberg B. et al 1999 J. Nucl. Mater. **266-269**, 75
17. Unterberg B. *et al.* 2000 Improved energy confinement at trans-Greenwald densities in discharges with a radiating edge in the tokamak TEXTOR-94, IAEA-CN-77/EX5/2
18. Messiaen A. et al 2001, Use of the correlation between the confinement and the edge neutral pressure for the feedback control of the plasma energy in the RI-mode of TEXTOR-94, 28th EPS, Madeira
19. Petrie T.W. *et al* 1993 Nucl. Fusion **33** 929
20. Suttrop W. *et al* 1999 J. Nucl. Mater. **266-269** 118
21. Baker D.R and Rosenbluth M.N. 1998 Phys. Plasmas **5** 2936

Chapter 4

Modeling of the effect from a strong gas puff and comparison with experiment

Introduction

The one-dimensional transport code RITM (*Radiation from Impurities in Transport Model*) [1] was developed to simulate in a self-consistent manner an influence of impurities on the transport under different plasma conditions. The results obtained with this code showed a good agreement with experimental observations from TEXTOR and demonstrated evidence of ITG-turbulence suppression during L-RI-mode transition. We used the same code to investigate an influence of changes at the plasma edge occurring with a strong gas puff on the density profile and on the confinement properties of plasma. The RITM-code was rearranged in such a way that it was possible to reproduce an experimental time evolution of discharges. Computations made with the RITM-code in which an external gas puff was introduced are presented in this chapter.

4.1 The RITM Code, transport equations

4.1.1 neutral particles transport

Recombination of charged particles at the wall and the gas puff are the main sources of neutrals in tokamak. Entering the plasma they interact with electrons and ions. The following elementary processes are taken into account by the RITM model. Molecules dissociate and two Franck-Condon atoms with an energy about 3 eV are generated:

$$H_2 + e \rightarrow (k_d^m) \rightarrow 2H + e\,.$$

Besides undergoing dissociation, molecules can also be ionized by electrons or charge-exchange with ions:

$$H_2 + e \to (k_i^m) \to [H_2^+ + 2e] \to H + H^+ + 2e\,;$$

$$H_2 + H^+ \to (k_{cx}^m) \to [H_2^+ + H] \to 2H + H^+\,.$$

Atoms charge-exchange with ions,

$$H + H^+ \to (k_{cx}^a) \to H^+ + H\,,$$

are ionized by electrons,

$$H + e \to (k_i^a) \to H^+ + 2e$$

and reproduced by the recombination of ions and electrons,

$$H^+ + e \to (k_r^a) \to H\,.$$

All those processes are characterized by the rate coefficients given in the bracket.

For all kinds of neutrals, RITM solves, in a diffusive approximation, the kinetic equations for the distribution functions of the velocity component along the minor radius, $f_j(v_r)$:

$$\frac{1}{g_1}\frac{\partial}{\partial r}\left(g_2 v_r f_j\right) = S_j - \nu_j f_j\,, \tag{4.1}$$

where r is the minor radius of the magnetic surface, j corresponds to different kinds of neutrals; S_j and ν_j are the sources and the frequencies of disintegrative processes for the corresponding neutrals. The Shafranov shift computed from the Grad-Shafranov equation in cylindrical approximation is used with analytically prescribed elongation and triangularity of the magnetic surfaces to determine the metric coefficients $g_{1,2}$ which differ from 1 due to toroidicity [2].

4.1.2 charged particles transport

The transport of charged particles is described by continuity equations for electrons

$$\frac{\partial n_e}{\partial t} + \frac{1}{r g_1}\frac{\partial}{\partial r}\left(r g_2 \Gamma_\perp^e\right) = S_n + \sum_Z Z S_Z\,, \tag{4.2}$$

and impurity ions of all charge states of He, C, O, Ne and Si:

$$\frac{\partial n_z}{\partial t} + \frac{1}{r g_1}\frac{\partial}{\partial r}\left(r g_2 \Gamma_\perp^Z\right) = S_Z\,; \tag{4.3}$$

with $n_{e,Z,}$ being the densities of the electrons and impurity species of the charge Z; both diffusive and convective contributions are included in the particle flux densities:

$$\Gamma_\perp^e = -D_\perp \frac{\partial n_e}{\partial r} + V_\perp n_e, \quad \Gamma_\perp^Z = -D_\perp^Z \frac{\partial n_Z}{\partial r} + V_\perp^Z n_Z ; \tag{4.4}$$

S_n is the net electron source due to ionization of hydrogen neutrals, S_Z is the source of the impurity species. The electron diffusivity is adopted in the form:

$$D_\perp = D_\perp^{ITG} \cdot f_{tr} + D_\perp^{DTE} + D_\perp^{EDGE}, \tag{4.5}$$

where the characteristic transport coefficients due to ITG and DTE modes are estimated from the individual growth rates given by Eq. (3.6) and (3.7) respectively in a mixing length limit [5],

$$D_\perp^{ITG} = \frac{\gamma_{\max}^{ITG}}{k_{\perp,\max}^2}; \qquad D_\perp^{DTE} = \frac{\gamma_{\max}^{DTE}}{k_{\perp,\max}^2}, \tag{4.6a,b}$$

The edge transport is characterized by the coefficient [6]:

$$D_\perp^{EDGE} \approx \frac{cT_e^{LCMS}}{eB} \frac{\rho_s^{LCMS}}{L_P^{LCMS}}, \tag{4.7}$$

where L_P is the e-folding length of the electron pressure and the superscript *LCMS* denotes that the parameters are computed at the LCMS. To simulate the decrease toward the plasma core of the anomalous transport triggered by the turbulence in the SOL an empirical factor $\exp\left(-\frac{r_{LCMS}-r}{L_P}\right)$ has been introduced.

The anomalous particle pinch velocity is governed mainly by the magnetic shear [7-9]:

$$V_\perp = \left(D_\perp^{ITG} \cdot f_{tr} \cdot \kappa + D_\perp^{DTE}\right) \frac{d \ln q}{dr}. \tag{4.8}$$

The small factor $\kappa = \frac{4r}{3R}$ reflects a relatively weak effect on convection of instabilities caused by ion dynamics, in particular, ITG instability [7,9]. The particle transport due to the instabilities under consideration is ambipolar since it results from drifts due to fluctuating electric fields. This implies that the diffusivities of electrons and ions are close each other. For the pinch velocity of impurity particles we adopt a neoclassical one, which is caused by the density and temperature gradients of the background ions [13]:

$$D_\perp^Z = D_\perp, \quad V_\perp^Z = V_\perp^{Z,neo}. \tag{4.9a,b}$$

The density and flux of the background ions are computed from the quasi-neutrality conditions:

$$n_i = n_e - \sum Z \cdot n_Z, \quad \Gamma_\perp^i = \Gamma_\perp^e - \sum Z \cdot \Gamma_\perp^Z \tag{4.10a,b}$$

4.1.3 heat transport

Heat transport is governed by the following equations for the electron and ion temperatures T_e and T_i. The latter is assumed the same for all ion species:

$$\frac{3}{2}\frac{\partial n_e T_e}{\partial t} + \frac{1}{rg_1}\frac{\partial}{\partial r}\left[rg_2\left(1.5\Gamma_\perp^e T_e - \kappa_\perp^e \frac{\partial T_e}{\partial r}\right)\right] = \frac{J^2}{\sigma} + Q_{au}^e - Q_{ei} - Q_{en} - Q_{eI} \tag{4.11}$$

$$\frac{3}{2}\frac{\partial n_\Sigma T_i}{\partial t} + \frac{1}{rg_1}\frac{\partial}{\partial r}\left[rg_2\left(1.5\Gamma_\perp^\Sigma T_i - \kappa_\perp^\Sigma \frac{\partial T_i}{\partial r}\right)\right] = Q_{au}^i + Q_{ei} + Q_{in} \tag{4.12}$$

where $n_\Sigma = n_i + \Sigma n_Z$, $\Gamma_\perp^\Sigma = \Gamma_i + \Sigma\Gamma_Z$, and $Q_{au}^{e,i}$ are the densities of electron and ion heat sources due to additional heating from NBI and ICRH estimated from TRANSP computations, Q_{ei}, Q_{en}, Q_{eI} the energy losses from electrons due to Coulomb collisions with ions, excitation and ionization of neutrals and impurities, respectively, Q_{in} the energy exchange between main ions and neutrals. The heat conduction coefficients are:

$$\kappa_\perp^i = \kappa_\perp^{i,NEO} + \left(D_\perp^{ITG} + D_\perp^{EDGE}\right) n_\Sigma, \quad \kappa_\perp^e = \left(D_\perp^{ITG} \cdot f_{tr} + D_\perp^{DTE} + D_\perp^{EDGE}\right) n_e, \tag{4.13a,b}$$

the neoclassical contribution is computed by taking into account all ion species [10].

The time evolution of the current density profile $J(r)$ including both ohmic and bootstrap contributions is computed from the current diffusion equation with the conductivity σ taking into account neoclassical corrections [11].

The boundary conditions to the transport equations, at the LCMS, are given by the e-folding lengths for the densities and temperatures, taken from measurements. This, of course, limits the self-consistency of our model. A future development is planned to improve this by coupling with a description of the SOL (*Scrape-off-Layer*) analogously to the approach realized by [4]. Additionally the total toroidal plasma current and the time evolution of the averaged plasma density are given. The latter is generated by choosing for each time step an appropriate influx of cold molecules in an iterative procedure. During the time interval of a strong puff the gas inflow is prescribed. The program for the neon puffing is chosen to reproduce the experimental evolution of the integral plasma radiation.

4.2 Influence of gas puff intensity on plasma profiles

4.2.1 simulation of the low gas puff

The 1-D transport code RITM with the anomalous transport model described above has been used to simulate the confinement rollover from the RI to the L-mode in plasmas with a strong gas puff. The calculations have been arranged in order to reproduce the experimental density profiles and also to obtain Z_{eff} in accordance with the experimental value. Computations are arranged in such a way, that the evolution of discharges is similar to the experimental one, discussed in the paragraph 3.7, and cab be compared to discharges in Fig. 3.16[a] at times 0.6-3.0 s. The computations are done with a constant neon puff, starting from the beginning of calculations, and with the ion temperature profile evolution taken from the experiment.

Fig. 4.1 [a] shows the time evolution of the electron density profile modelled with a ***low gas injection***. The calculations start from the initial parabolic profile. Then the gas influx is feedback controlled by the prescribed program for the ramp of the line averaged density up to the time of 0.3 s (see Fig. 4.1[b]). It is seen that the puff of impurities leads to the peaking of the density profile with decreasing edge density. This behavior is in agreement with the experimental observation during L to RI-mode transition [12 and paragraphs 3.5, 3.7 of this thesis]. At a time of 0.3 s quasi-stationary RI-mode conditions are reached, which are characterised by a peaked density profile, a high radiation fraction P_{rad}/P_{tot}~0.7 and by ITG mode suppression over a wide radial zone of the plasma. From this time till the end of calculations at t=0.6s the gas puff is maintained constant (see Fig. 4.1[b]).

After the gas puff rate is fixed, the density profile continues to peak and the central electron density exceeds $1.1 \cdot 10^{14}$ cm^{-3}. Simultaneously, with the increase of line averaged density, the edge density is maintained at a relative low level. During the whole time the effective ion charge, Z_{eff}, (see Fig. 4.1[b] and Fig.4.2 curve **a**) is in the range 1.8-2.4. The simulated evolution of the profiles is typical for the experimental behaviour observed in the discharges with a low or moderate fuelling rate (see Fig. 3.18). It is necessary to note, that in present computations the absolute values of the gas puff intensity are by the order of magnitude higher than those in Fig. 3.16[a], it is mainly due to shorter time scale and high absolute values of transport given by Eq. (4.7). Nevertheless, the time evolution of a gas puff is similar to one in Fig. 3.16 [a], that allows to reproduce an evolution of the density profile in agreement with experiment.

The steady state profile finally reached in this simulation reproduces well the experimental RI-mode density profile and has a steep gradient over a wide plasma zone. As a result, the ITG-mode is suppressed and the diffusion flow caused by this turbulence is reduced over 2/3 of the radius.

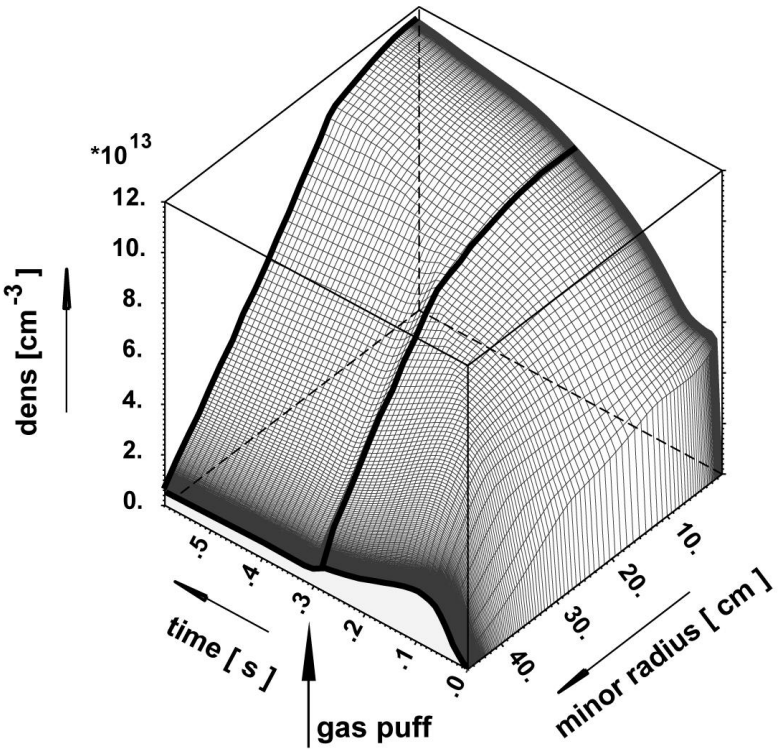

Fig. 4.1[a] Evolution of the electron density profile with impurity seeding started from the beginning and low gas puff started at 0.3 s.

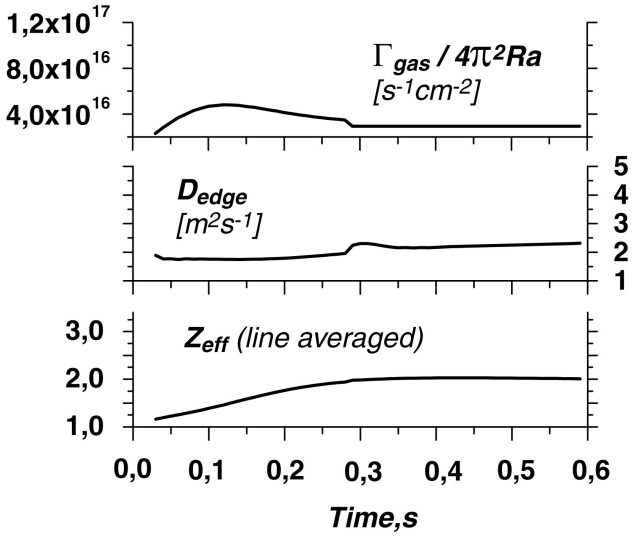

Fig. 4.1[b] Time traces of the gas influx, edge diffusion and Z_{eff} durin the simulations presented in Fig. 4.1 [a]

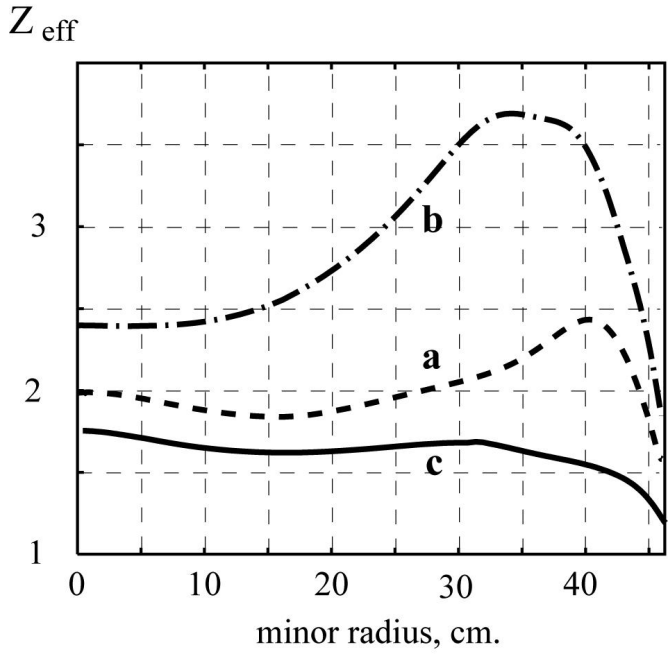

Fig. 4.2 Final Z_{eff} profiles for the calculated discharges presented by figures 4.1, 4.3 and 4.5.

4.2.2 simulations made with increased gas puff

In the discharge shown in Fig.4.3 [a,b] the gas puff is increased at t=0.3 s by a factor of 3 with respect to the level assumed in the previous case. This results in a strong broadening of the density profile in rough agreement with the experimental behaviour. However, the increase in the edge density and its gradient significantly exceed the measured values and the density profile is too flat in the outer plasma region (see Fig. 4.3[a]). Moreover, the increase of the gas puff results in a further rise of Z_{eff} in the whole plasma column with respect to the level in the RI-mode (see Fig. 4.3[b] and Fig.4.2, curve **b**). The latter contradicts the experiment, which shows a significant decrease of Z_{eff} with the intense gas puff.

Thus, the computations show that the effect of a strong gas puff can not be simulated by an increase of the neutral particle influx alone, but that, additionally, the transport of charged particles should be increased. In the plasma core this occurs automatically because the broadening of density profile leads to a resumption of the ITG induced transport on a wide plasma zone. However, charged particles can not leave the plasma since their diffusivity at the plasma edge is limited by the present edge transport model given by Eq.(4.7). Moreover $D_{\perp}^{EDGE}$ even decreases when the temperature at the LCMS drops with the neutral puff (see Fig. 4.3[b]).

One can see that the value of the edge transport given by the Eq. (4.7) depends on the e-folding lengths at the LCMS which are taken constant from the experiment. On the other hand, it is known that the density profile of the L-mode is characterized by the shorter L_n at the edge. Possibly, that assumption can explain the disagreement between modelling and experiment. Figure 4.4 shows the dependence of the density,

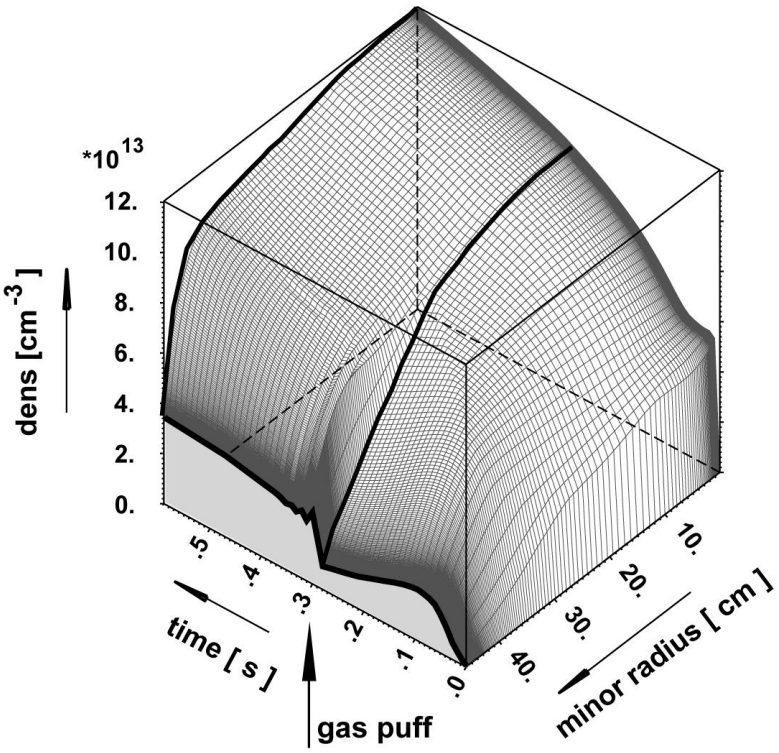

Fig. 4.3 [a] Simulated evolution of the electron density profile where the gas puff intensity after 0.3 s is by a factor of 3 higher than one in the discharge presented by Fig. 4.1 .

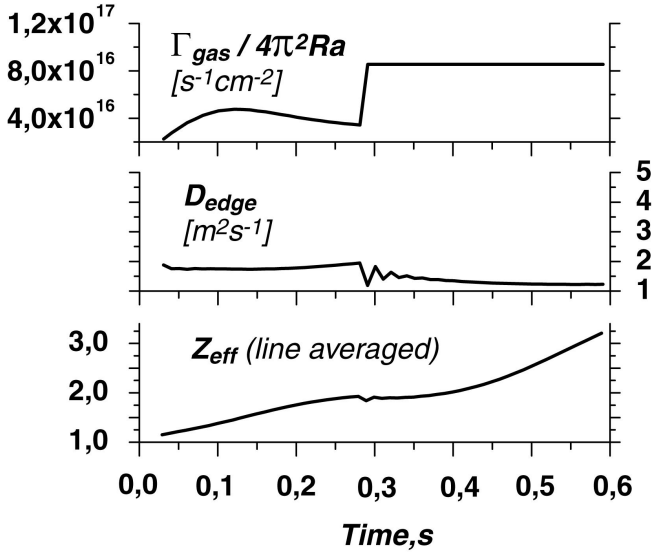

Fig. 4.3[b] Time traces of the gas influx, edge diffusion and Z_{eff} durin the simulations presented in Fig. 4.3 [a]

effective charge and ITG-induced diffusion profiles on the density e-folding length value at the LCMS. The shortening of L_n allows to obtain the density profile closer to

the experimental one with the simultaneous reduction of the effective charge and as the consequence higher ITG diffusion. But, to obtain the value of Z_{eff} at least the same like in the RI-mode (to be in agreement with the experiment we need much lower one) we should assume L_n much shorter than it is observed in experiment.

One can also speculate that the penetration of neutrals through the scrape-off layer should play an important role, but it was found that the penetration depth does not effect the density profile with the present model for the edge transport.

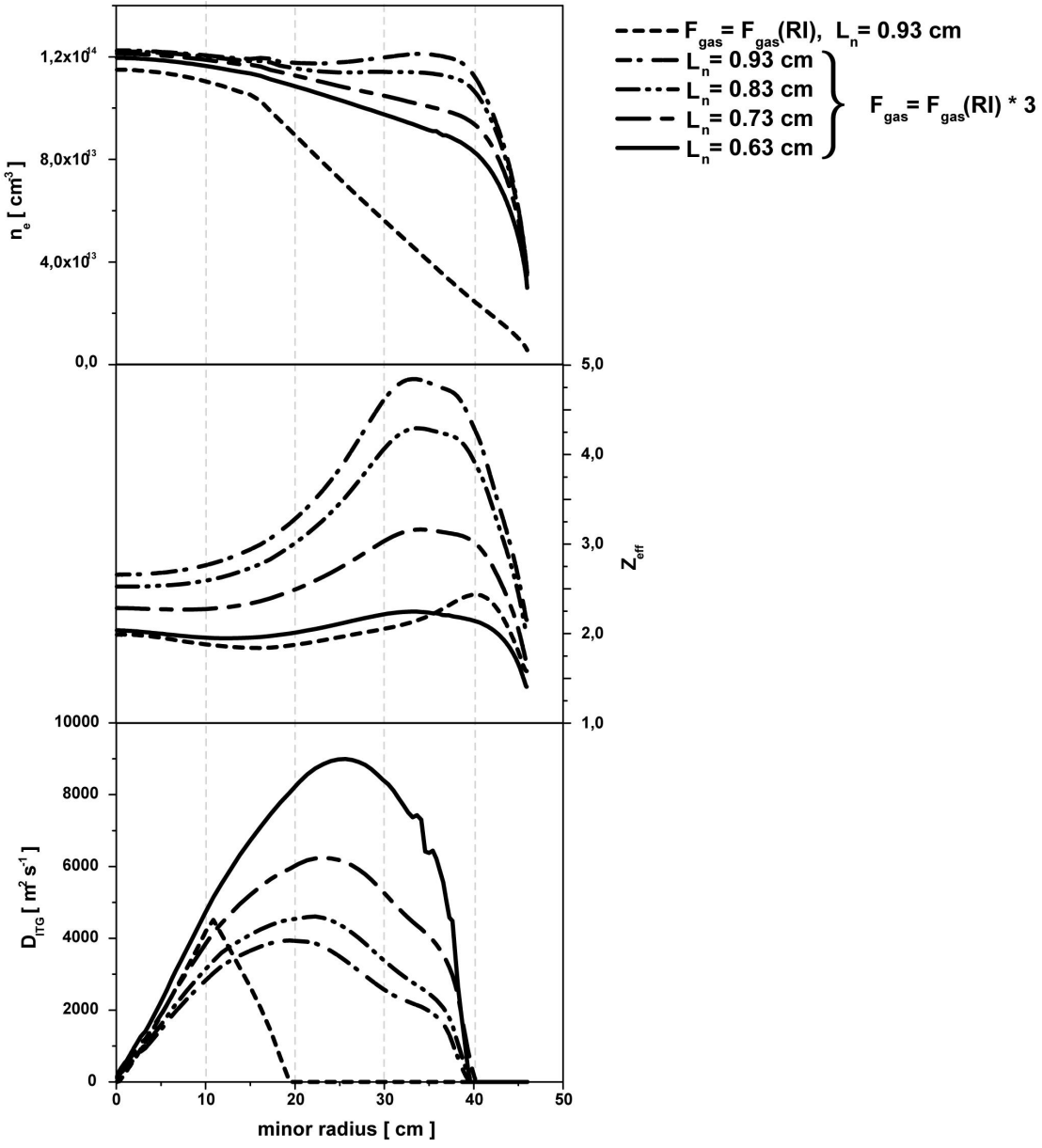

Fig. 4.4 Dependence of the density, effective charge and ITG-induced diffusion coefficient on the density e-folding length value at the LCMS.

4.2.3 simulations made with increased gas puff under the assumption of increased edge transport

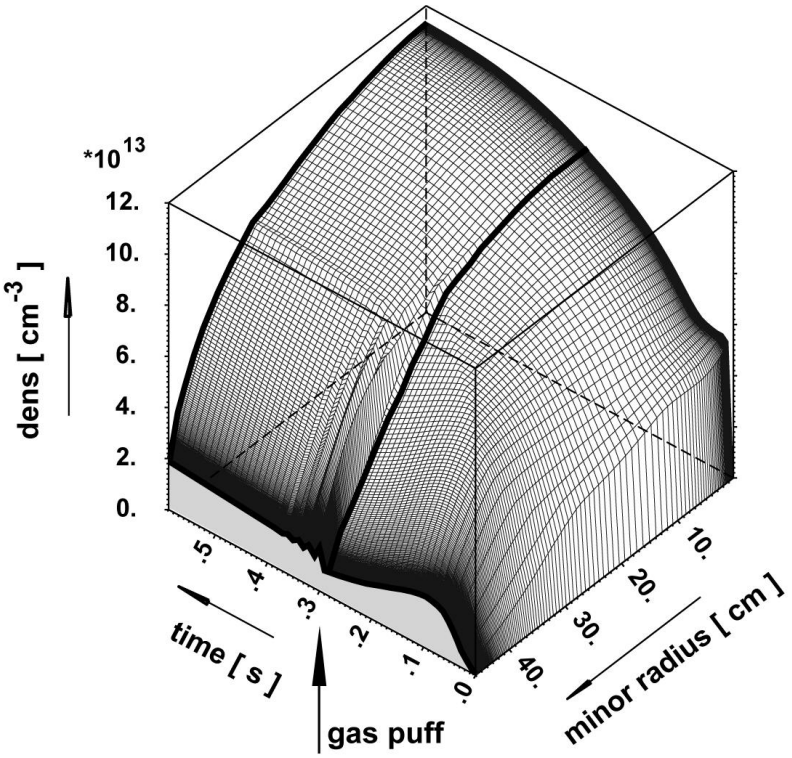

Fig. 4.5 [a] Simulated evolution of the electron density profile where simultaneously with an increase of the gas puff intensity the edge transport was increased by the factor of three.

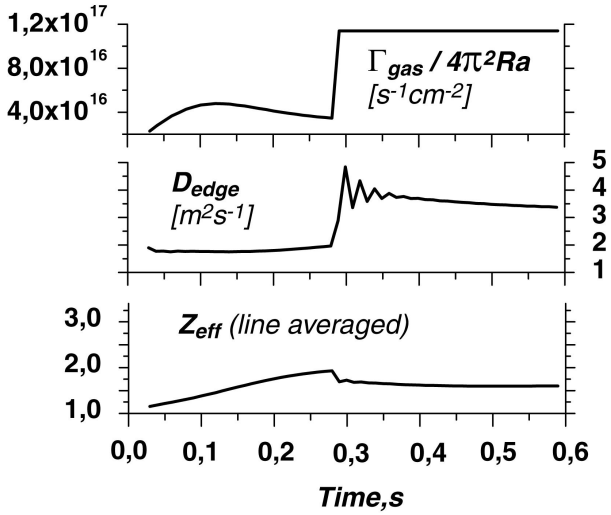

Fig. 4.5[b] Time traces of the gas influx, edge diffusion and Z_{eff} durin the simulations presented in Fig. 4.5 [a]

Figure 4.5[a] shows the density profile computed under the assumption that, simultaneously with the intensification of the gas puff at t=0.3s, the edge diffusion coefficient is increased by a factor of 3 with respect to the level prescribed by Eq. (4.7) (see Fig. 4.5[b]). In this case the flattening of the density profile occurs in agreement with the experimental observations without formation of an extremely high density and density gradient at the LCMS. Simultaneously the high edge diffusion allows more impurity ions to escape from the plasma and the Z_{eff} value reduces in the whole plasma (see Fig. 4.5[b] and Fig.4.2 curve **c**).

The steady state profiles finally reached in these simulated discharges are quite different (see Fig. 4.6, 4.7). The calculated density profile in the case of a low gas puff (Fig.4.6) reproduces well the experimental RI-mode density and has a steep gradient over a wide plasma zone. As a result, the ITG-mode is suppressed and the diffusion flow caused by this turbulence is reduced over 2/3 of the radius. The later is also confirmed by the experimental data. As it can be seen in Fig. 4.6 (at the bottom) showing the profiles of the parameters η and $\eta_{critical}$ computed from experimental profiles, the ITG turbulence exists only in the central plasma region.

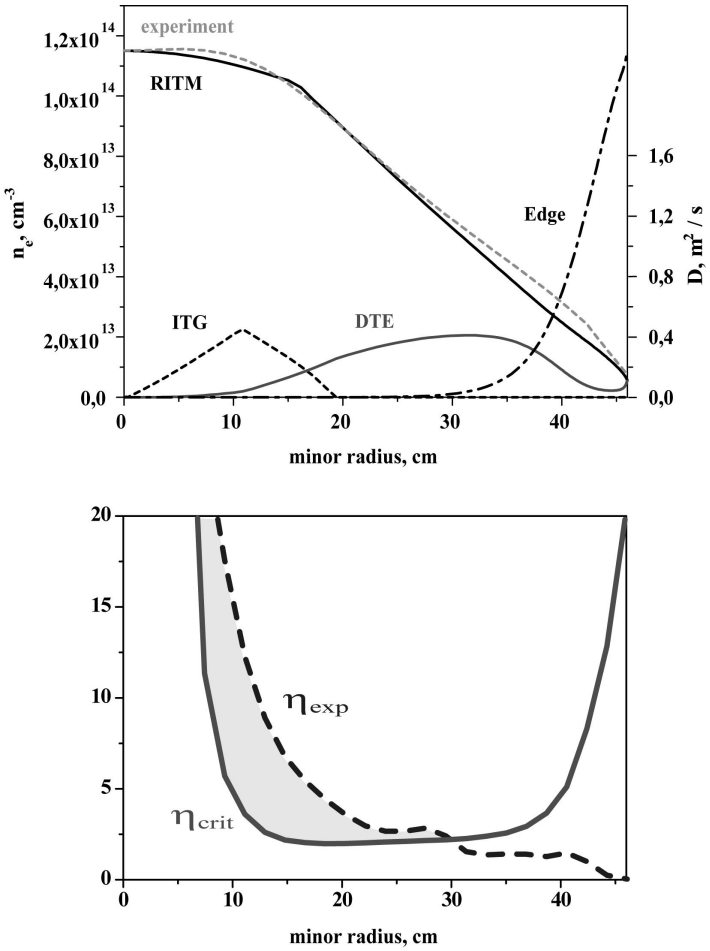

Fig. 4.6 Low gas puff: (top) Profiles of computed and experimental electron density and corresponding diffusion coefficients from ITG, DTE and Edge modes; (bottom) Profiles of the parameter η and its critical value for the suppression of ITG mode computed from experimental profiles.

Figure 4.7 (top) shows the density and diffusion profiles for the modelled discharge in which the gas puff is increased by a factor of 4 and the edge diffusion coefficient is increased by a factor of 3 with respect to the first simulation. The computed density profile mimics the shape of the experimental density profile after the RI-L back transition caused by a strong gas puff. Nevertheless, there is a difference of 20% in the line-averaged densities between experimental and RITM-simulated density profiles. This discrepancy arises from the different values of the density at the LCMS, where the simulation assumes fixed e-folding lengths for the densities and temperatures as boundary conditions. We expect that a more sophisticated model for the scrape-off layer (SOL), taking into account ionisation of neutrals in the SOL, would improve the numerical results.

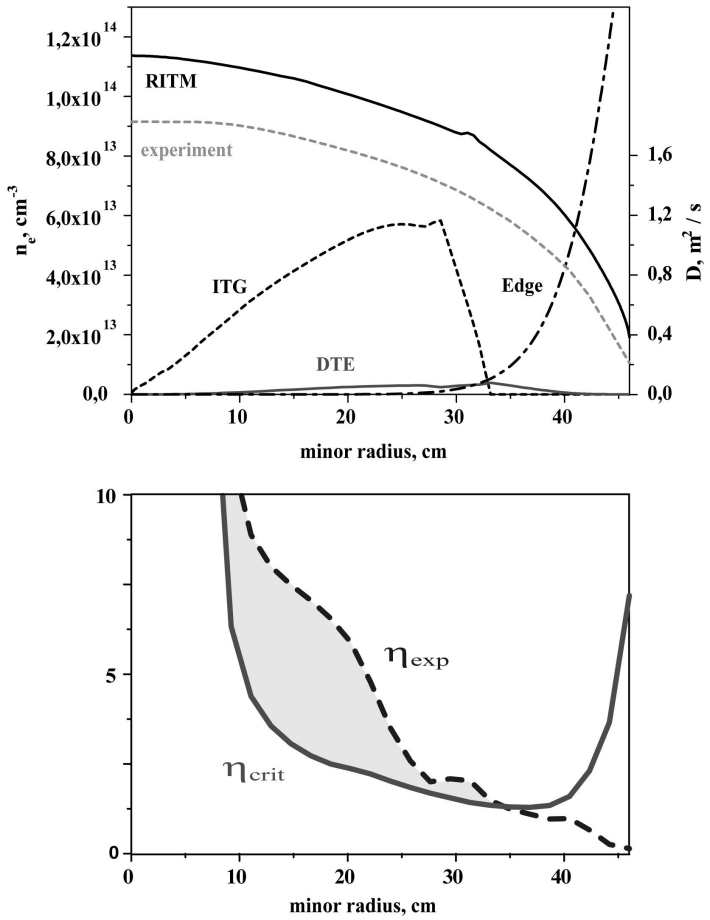

Fig. 4.7 Strong gas puff: (top) Profiles of computed and experimental electron density and corresponding diffusion coefficients from ITG, DTE and Edge modes; (bottom) Profiles of the parameter η and its critical value for the suppression of ITG mode computed from experimental profiles.

It is important to stress that the strong gas puff results in the resumption of the ITG-turbulence in the significant part of plasma, as it follows from the modelling and supported by the experimental measurements of η profile.

4.3 RI-L bifurcation caused by the strong gas injection

In section 3.5 (also see [14]), the transition from L to RI mode caused by seeding of impurities has been interpreted as a bifurcation originating from the parametric dependence of the electron flow upon the peaking factor $p = d\ln n_i / d\ln T_i$, (the inverse value of the parameter η_i often used in ITG models). When plotting the electron flow versus p, an N-shaped dependence is obtained (see Fig. 3.10). The present computations show that the same model is capable of explaining how a strong gas puff can provoke a back transition from RI to L-mode.

The value of the peaking factor at a given radial position can be determined from the integral of the continuity equation for electrons (Eq.(3.14)). Figure 4.8 shows the function G(p) calculated for the conditions pertaining to 4 time instants in Fig.4.5 at 2/3 of the minor radius, where the variation in the density gradients during the stage of intensive gas puff is most pronounced.

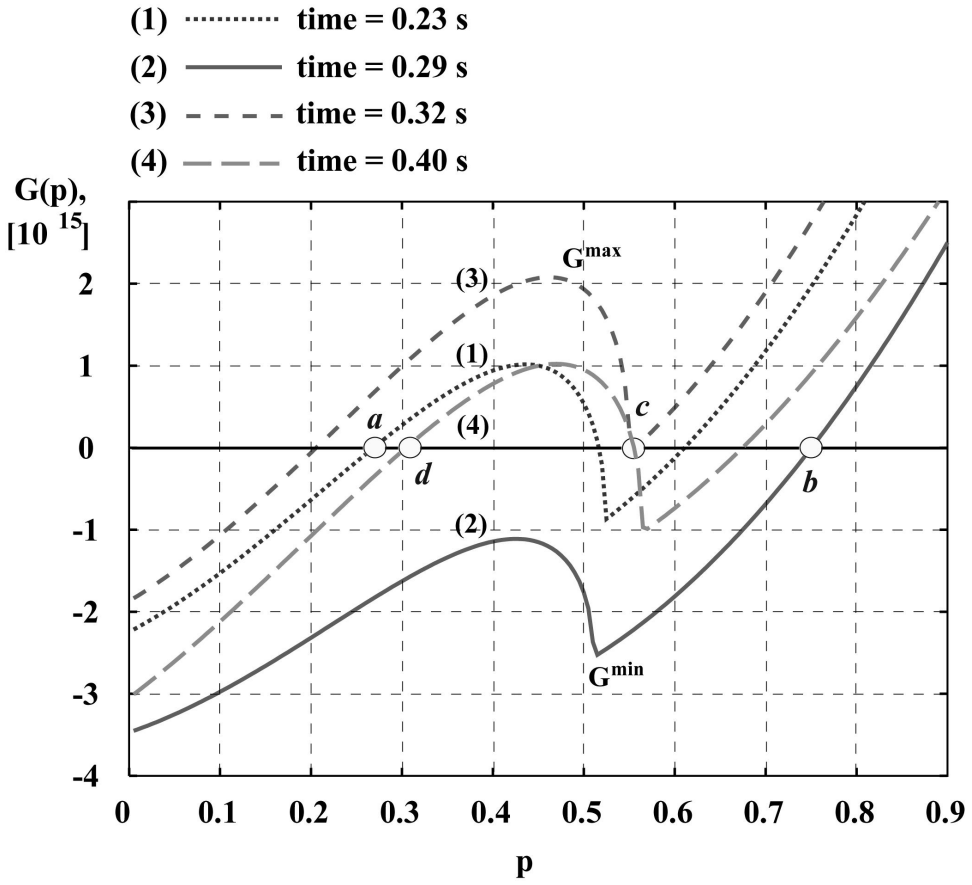

Fig. 4.8 The G function versus the peaking factor p for four time instants in the discharge with the strong gas injection for the conditions pertaining at 2/3 of the minor radius.

The calculations start from the L-mode state, curve (1), where the position of the maximum and minimum values of G(p), G^{max} and G^{min}, with respect to zero level is such that $G^{min} \le 0 \le G^{max}$. The solution ***a*** with a low *p* is realized on the branch of the ITG-mode. As it was discussed in the section 3.5, due to the increase of Z_{eff} caused

by neon seeding, G^{max} decreases because of the Z_{eff} dependence in γ^{ITG}. When G^{max} becomes negative, only the solution ***b*** on the branch of the DTE-mode remains. That solution is characterized by a high value of *p*. This is demonstrated by curve 2 for the RI-mode at t=0.29s. Strong gas puff started at t=0.3s results in an upward shift of the G-curve. This occurs on account of Z_{eff}, decreasing due to an increased edge diffusion, and increasing local density. Positive $\partial n_e / \partial t$ in the last term of Eq. (3.14) moves G^{min} upwards. When G^{min} approaches to zero, curve 3, solution ***c***, the plasma switches into the state on the branch where $\gamma^{ITG}>0$. As $\partial n_e / \partial t$ eventually diminishes with attainment of steady state conditions, G^{min} becomes smaller than zero, G^{max} still remains positive because of the low value of the effective charge. Finally the plasma settles into the stable stationary state ***d*** on curve 4, corresponding to the L-mode and characterized by the low peaking factor.

The gas puff of low intensity in the discharge presented by the Fig. 4.1, does not lead to such a reverse bifurcation, since G^{min} and G^{max} remain negative due to the high, preserved value of the effective charge and small $\partial n_e / \partial t$.

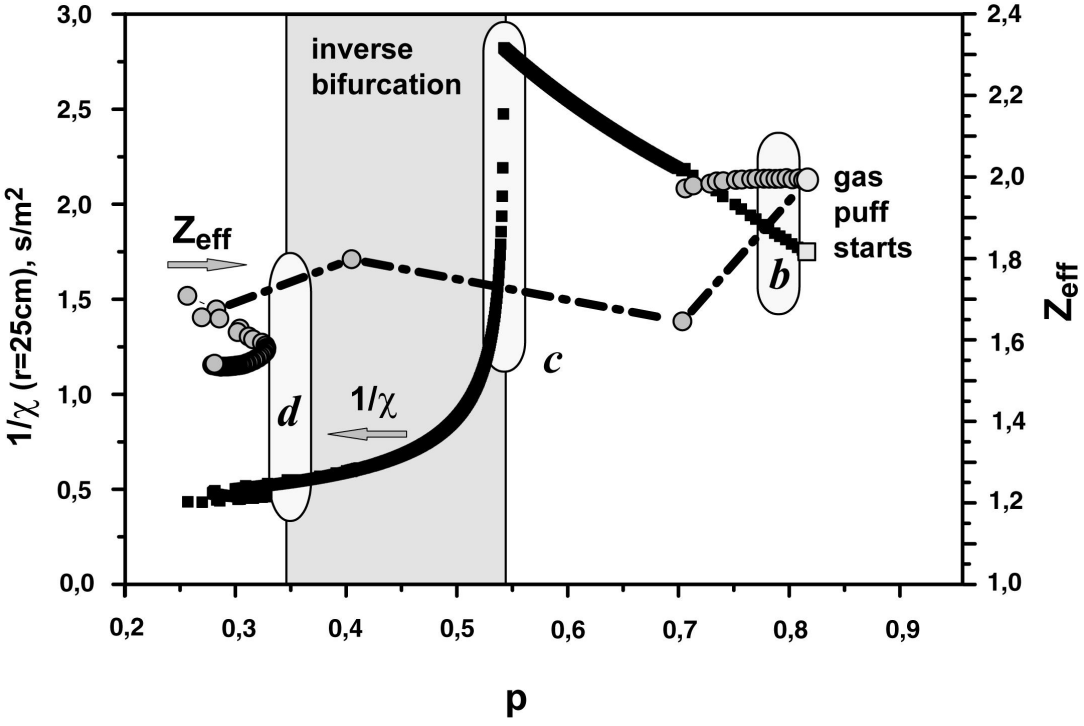

Fig.4.9 Evolution of the local confinement properties during the inverse bifurcation triggered by the gas puff

Based on the bifurcation scenario it is possible to explain the effect of a strong gas puff on the confinement properties. Figure 4.9 shows the evolution of the local confinement and effective charge versus the peaking factor. The confinement quality is quantified by the inverse value of the total heat conductivity, $1/\chi$. The steady state RI-mode obtained after the neon injection, ***b***, is characterized by the high confinement, $1/\chi \approx 1.8$ s/m^2, and a high value of the effective charge, $Z_{eff} \approx 2.0$. The strong gas puff leads to the significant reduction of the Z_{eff} but does not, immediately, affect the confinement properties. The confinement even increases while the G-function in Fig. 4.8 moves upwards, since the transport is governed only by the DTE-

mode and proportional to the peaking factor. When the minimum of the G-function approaches zero, the inverse bifurcation to the state with the low peaking occurs. During the bifurcation the confinement reduces significantly because of the resumption of the ITG-instability. The huge transport after the bifurcation leads to the further reduction of the Z_{eff} while the confinement quality remains.

The evolution of the density profile found in these computations (figures 4.1 and 4.5) is very similar to the experimental one in Fig. 3.17 after the neon injection. Figure 4.10 presents the development of the density peaking factor, γ_n (see Eq.(3.21)), with respect to the Greenwald number for two discharges. An injection of neon, started at the beginning of the calculations, results in the significant increase of γ_n while the density grows. During that time the bifurcation into the RI-mode occurs. Since the low gas puff does not trigger any reverse bifurcation mechanism, the density peaking increases further without an increase of the line averaged density.

As it was already shown by the evolution of the G(p) function, the strong gas puff produces an inverse bifurcation from RI to L-mode, causes the strong broadening of the density profile, and leads to a significant reduction of the γ_n value.

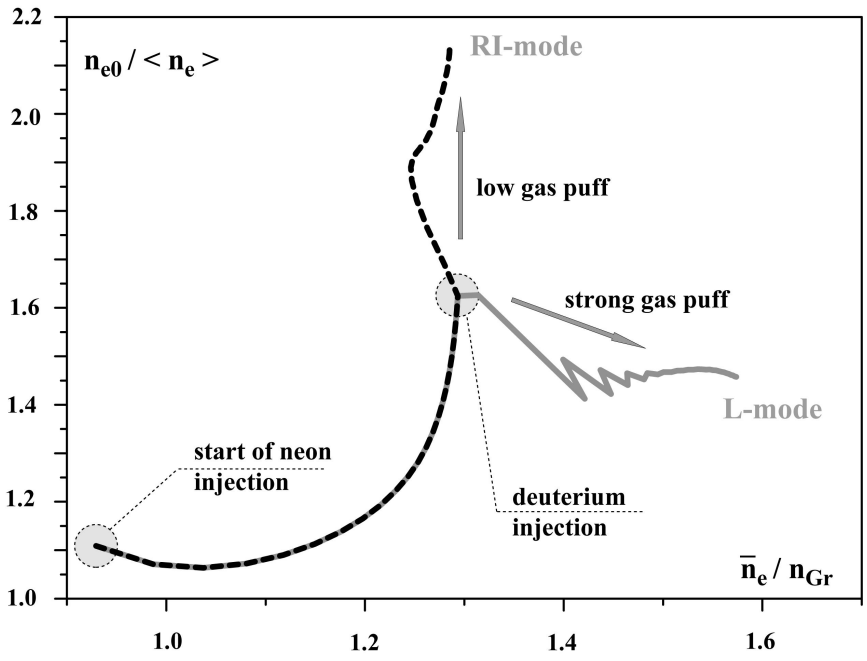

Fig. 4.10 Evolution of the density peaking factor, γ_n, versus Greenwald factor for the computed discharges, presented by figures 4.1 and 4.5

4.4 Experimental confirmation of increased edge transport with the strong gas puff

The idea of the edge transport increase caused by a strong injection rate, which first emerged from results of the RITM modelling (see section 4.2), was later confirmed by

the reflectometer measurements performed on TEXTOR in the impurity seeded discharges where gas puffs of different intensities were applied.

Figure 4.11 shows two discharges differing by the intensity of the gas puff, applied after the neon injection brought the confinement to the H-mode level. The moderate gas puffing in the discharge #88478 allowed to preserve the energy confinement of the H-mode quality at the density of 20-30% above the Greenwald limit. In the discharge #88482, presented by the dashed curves, the intensity of the gas puff was increased by a factor of 3. That leads to the confinement rollover towards L-mode with simultaneous flattening of the density profile and rise of the edge density and neutral pressure.

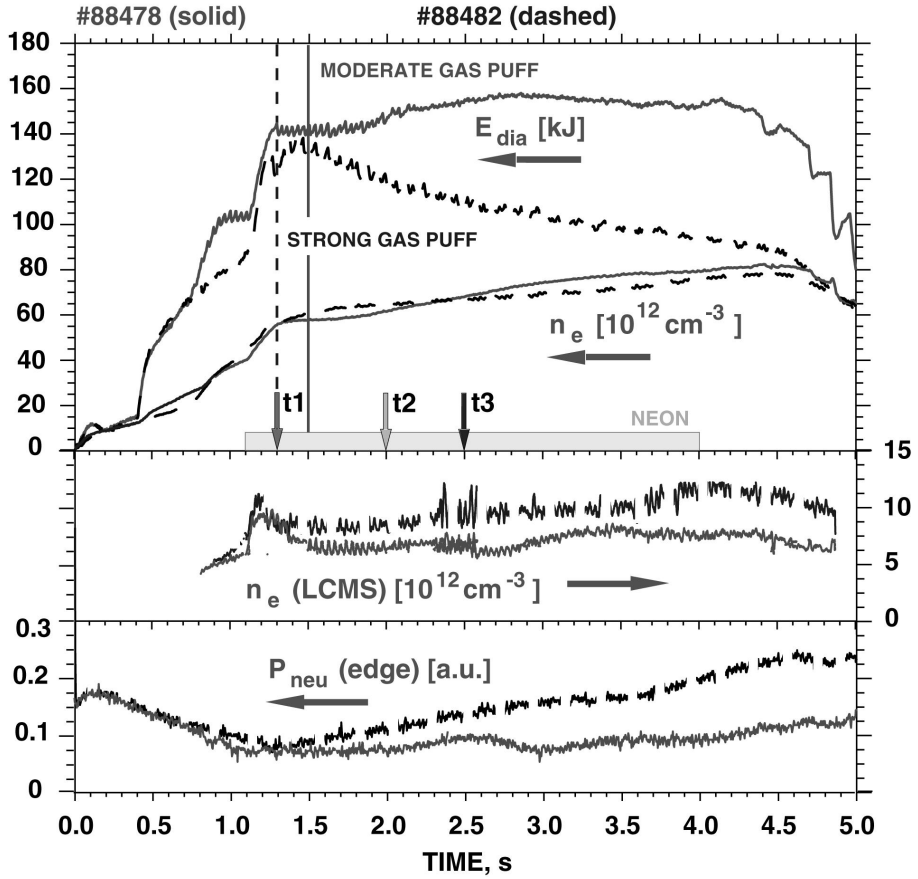

Fig. 4.11 Two discharges differing by the gas puff rate: 88478 (dashed curves) – slow gas puff [$3*10^{21}$ part/sec], 88482 (solid curves) – strong gas puff [$8*10^{21}$ part/sec]. E_{dia} is the diamagnetic energy; n_e is the line averaged electron density; n_e(LCMS) is the electron density at the last closed magnetic surface; P_{neu} is the neutral pressure at the edge; n_{Gr} indicates the Greenwald density limit; t1,t2,t3 are the times of the reflectometer measurements.

Figure 4.12 shows the frequency spectra of the density fluctuation measured by a microwave reflectometer [15] during the discharges of Fig. 4.11. The position of the reflection layer estimated from the cut-off density, corresponding to the reflectometer frequency, is from the top and 2-3 cm inside the LCMS towards the plasma core. It is

seen that both discharges start from the same frequency spectrum of fluctuations. The spectrum remains unchanged in the discharge with a moderate gas puff. In contrast, the intense gas puff leads to a sharp increase of the fluctuation amplitude in the frequency range below 50 kHz [16]. The shift of the maximum of the initial spectrum (t = 1.3 s) could be due to a plasma rotation, which would cause a Doppler shift of the measured frequencies [17]. It should be noted that the same changes in fluctuation spectra were also observed in the discharges where the confinement degradation took place with the moderate gas puff, but due to not optimized wall conditions, as it was presented by the Fig. 3.15.

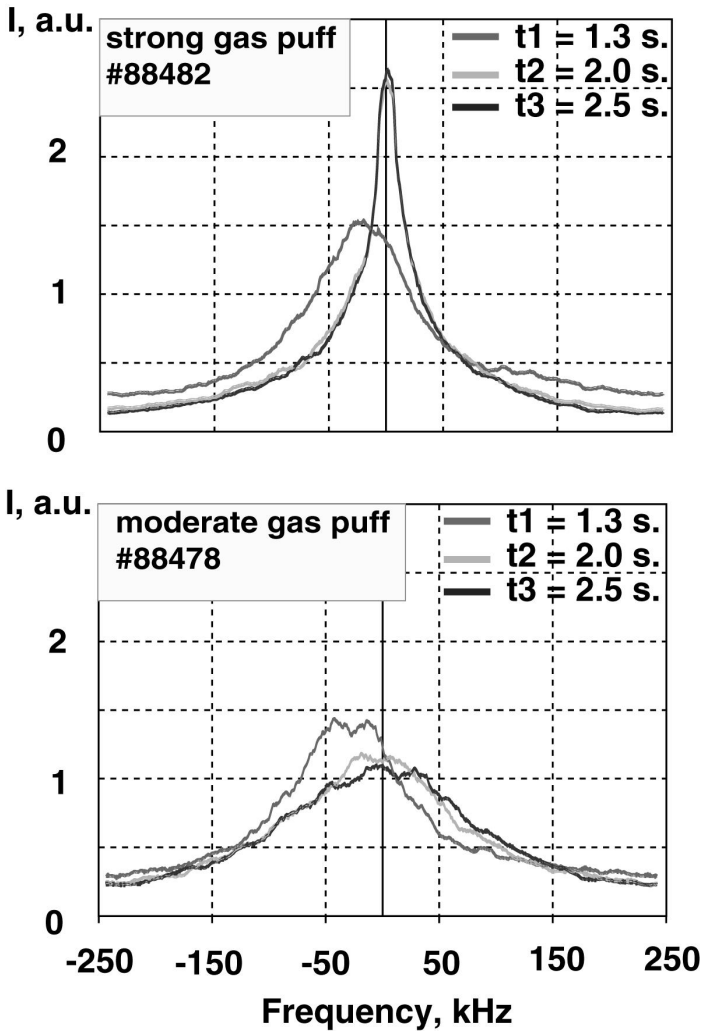

Fig. 4.12 Frequency spectra of density fluctuations measured by the microwave reflectometer from 2-3 cm inside LCMS in discharges presented in the Fig. 4.11

Figure 4.13 shows the correlation between electron density and temperature at LCMS and the width of the auto-correlation function, Δ_{ACF}, being inverse proportional to the perpendicular component of a wave vector of fluctuations. The whole data set is taken at a given magnetic field B_t=2.24T and plasma current I_p=380kA. The areas corresponding to the RI and L-mode are separated by the gray curve where the energy

confinement time, τ, is 80% of that predicted by the RI- mode scaling (Eq. 3.22). It is seen that Δ_{ACF} increases when the plasma edge parameters cross the gray curve going from the RI- to L-mode as a result of an intense gas puff. If one assumes that the plasma rotation does not change significantly in the considered sequence of discharges at the radii near the cut-off layer, then the $\Delta_{ACF} \sim <\lambda> \sim 1/<k_\perp>$, where λ is the wave length of turbulence, averaged over the frequencies and the reflecting volume, and $k_\perp$ is the poloidal component of the wave vector. As the diffusion coefficient is proportional to $1/k_\perp^2$ [5], Fig. 4.13 therefore suggests, in agreement with the RITM modeling, that anomalous transport in the plasma edge increases at the time of the confinement deterioration.

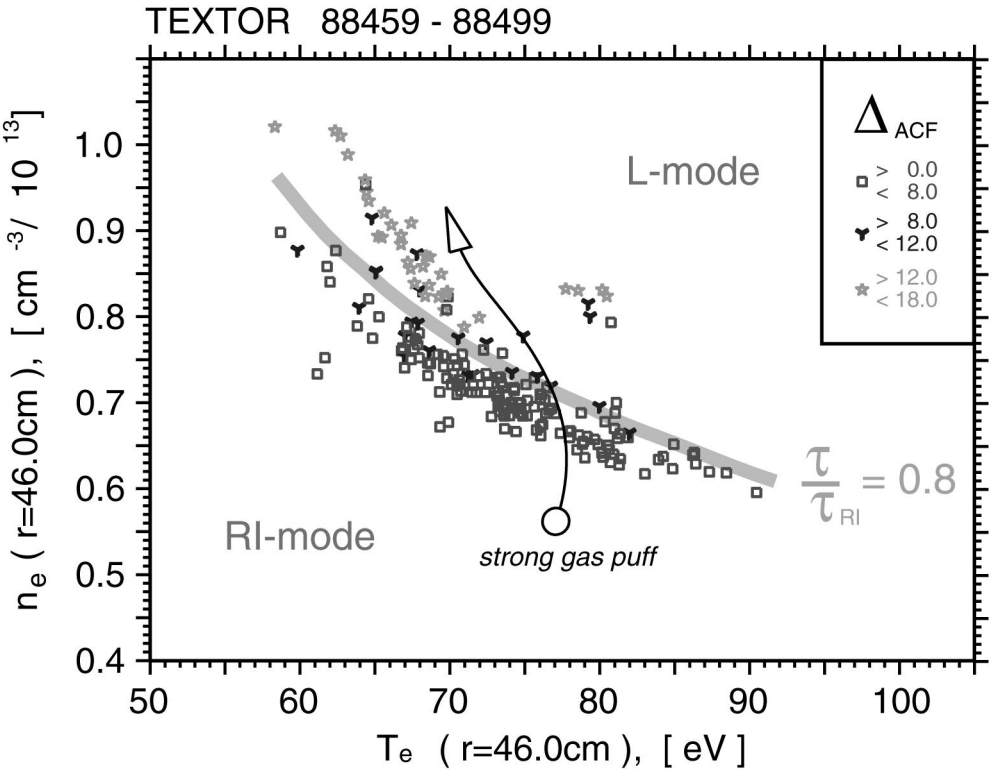

Fig. 4.13 Variation of the auto-correlation function Δ_{ACF} , measured by reflectometer (r≈44 cm), with the plasma edge parameters and its correlation with the confinement performance.

4.5 Summarizing the results of the modeling

The results presented by sections 4.2-4.4 have demonstrated that the confinement degradation in plasmas with a strong gas puff can be explained on the basis of the model described in the sections 3.5 and 4.1. The computations done for different intensities of the gas puff, are capable to reproduce different plasma parameters profiles and also to model the evolution of the discharge.

One sees that the degradation of confinement occurs on account of a significantly increased edge transport. The latter leads to the decrease of the impurity content in the plasma. Together with the reduction of the peaking factor that resumes the ITG-induced transport. The restart of the ITG-mode brings the confinement back to the L-mode level.

The model given by Eq. (5.7), being capable of reproducing the edge transport under RI and non-seeded L-mode conditions, does not allow to explain, in a self-consistent manner, the increase of the edge diffusion during the confinement rollover caused by the strong puff of neutrals.

An appropriate description of the edge transport specific edge instabilities which can be found in the literature is still open in our model. It should explain how the puffed neutrals give a rise to the edge transport of the order of 1 m^2/s.

4.6 Possible candidates for an instability driving the anomalous edge transport

4.6.1 ionization instability

One mechanism, which might drive the turbulence at the plasma edge, is the so-called ionization instability [18-20]. The physics of ionization instability is simple: if the plasma density increases locally as the result of the compression and/or convection effects, it enhances the ionization rate of neutrals by electrons. That contributes directly to the fluctuation growth. A typical dispersion relation for an ionization-driven instability [18,19] has stabilizing terms from the parallel transport and also from the diffusion, *D*, where *D* represents some transport mechanisms other than the ionization mode. The growth rate is then:

$$\gamma_i = \nu_i - \frac{1.71\,\eta_e\,\omega_*}{\chi_{\|}\,k_{\|}^2} - D\left(\frac{1}{\Delta^2} + k_\theta^2\right). \tag{4.14}$$

Here ν_i is the ionization rate, given by $\nu_i = n_N \langle \sigma v \rangle_i$, n_N is the neutral density, and Δ represents the radial width of the mode.

However, the computations made for the conditions described in section 4.2 showed that the ionization source in the Eq. (4.14) is always balanced by the term representing other transport mechanisms for any transport level at a given edge density. Thus, the ionization instability in the form, as it is usually presented, does not exist under the considered conditions.

4.6.2 destabilization of drift waves by the friction with neutrals

Another possible mechanism of the influence of the puffed neutrals on the edge transport can be the enhancement of the drift wave instabilities through the friction between ions and neutrals in their charge-exchange interactions. This channel could

be important since the measurements reveal a strong increase of the neutral pressure at the edge, P_{neu}, in obvious correlation with confinement degradation (see section 3.8).

As it was demonstrated by Linson and Workman [21] the friction of plasma ions with neutrals due to charge-exchange processes in the ionosphere can lead, under specific conditions, to the excitation of new drift instabilities. Recently, this idea has been applied to explain anomalous transport in the SOL plasma of divertor tokamaks by Daughton *et al* [22]. The underlying mechanism can be understood from Fig. 4.14. There a drift wave perturbation of the plasma density is considered, $\tilde{n} \propto \exp\left(-i\omega t + ik_y y + ik_z z\right)$, where $k_{y,z}$ are components of the wave vector. In the presence of a radial flow of neutrals, the friction force on the ions generates a poloidal drift of charged particles, leading to a perturbation of the poloidal current $\tilde{j}_y$

$$\tilde{F}_{fr} = \frac{1}{c\, m_i}\left[\, \tilde{j}_y \times B_0 \,\right] \quad . \tag{4.15}$$

Since the total current perturbation is divergence-free, a distortion of the current component parallel to the magnetic field arises:

$$\tilde{j}_z = -\tilde{j}_y\, k_y / k_z \,. \tag{4.16}$$

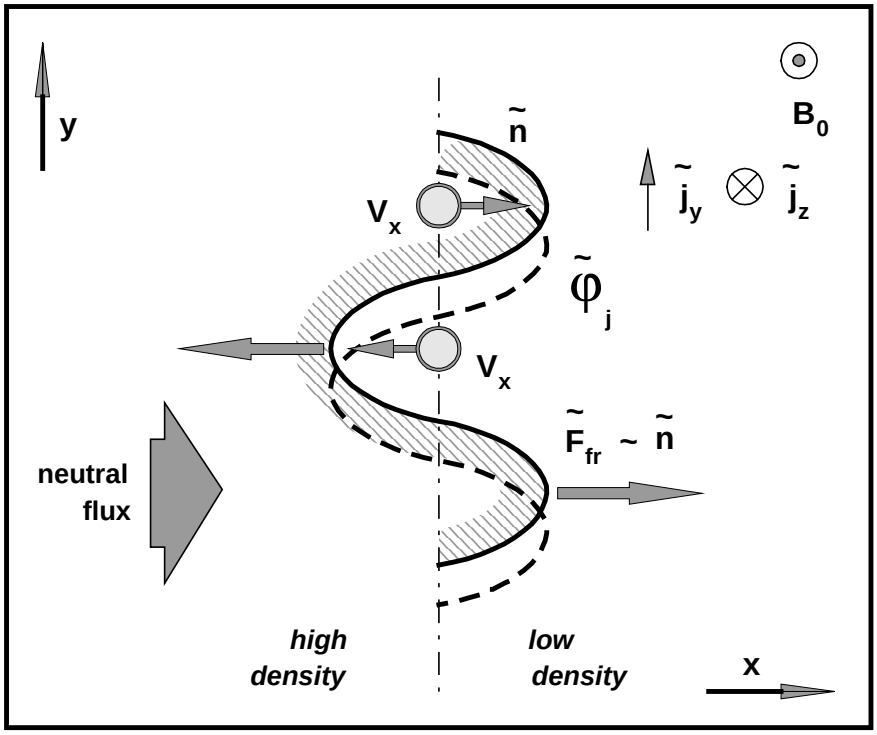

Fig. 4.14 Destabilization of drift waves by friction with neutrals.

The z-component of current gives a contribution to the Ohm's law. That brakes the Boltzmann distribution of the electron density:

$$T_e \frac{d\tilde{n}}{dy} = en\frac{d\tilde{\varphi}}{dy} + \frac{m_e}{e\tau_{ei}}\tilde{j}_z . \tag{4.17}$$

The poloidal electric field resulting from Eq. (4.17) is such that the produced radial drift can lead to the growth of the wave amplitude.

Daughton *et al* [22] demonstrated that, for an instability to grow, the radial gradient of the neutral pressure should have the same direction as the gradient of the unperturbed plasma density. Such a situation can be realized in the vicinity of a strong neutral source such as, e.g., produced by strong gas puffing. Here a total number of neutrals launched into the plasma is comparable with the total loss of plasma particles through the LCMS. The ionization of these neutrals can provide a local maximum in the density of charged particles [23], as it is demonstrated in Fig. 4.15. Neutrals push the ions with the force **F** in the radial direction *x*. It leads to the guiding center drift, $V_d \propto F \times B$, in the *y* direction. The resulting charge separation leads to the $E \times B$ drift in the *x* direction and reinforces the initial density perturbation so that the resulting radial gradient of the ion density can have the sign required for the instability.

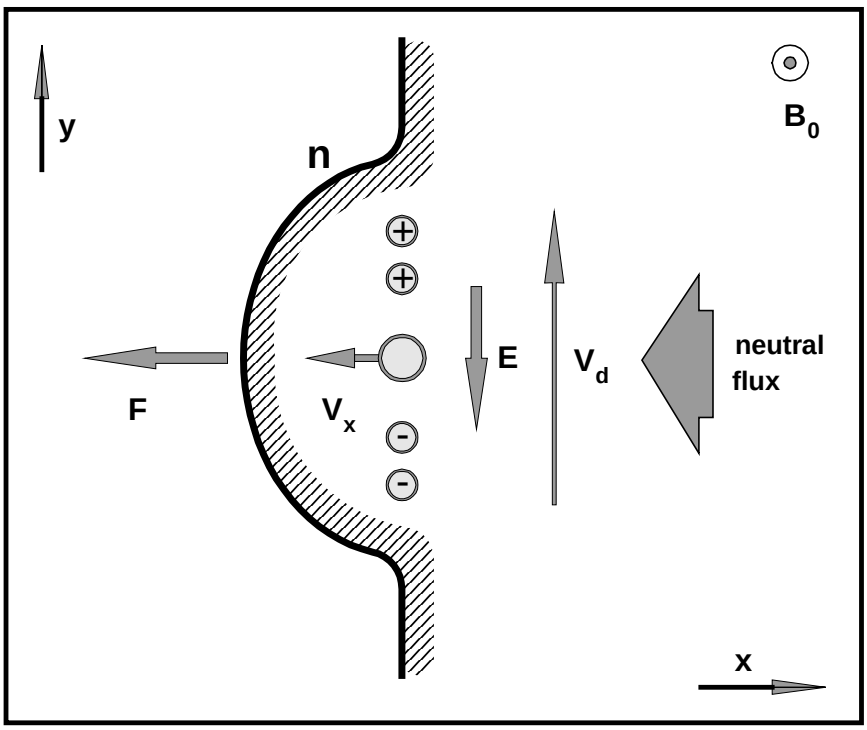

Fig. 4.15 Density perturbation with the local gas puff.

No firm appraisal of this mechanism can be made without further complex modeling. However, in the limit of a very large influx of neutrals the growth rate of the instability can be roughly estimated [22] as

$$\gamma \approx \sqrt{k_{cx} j_a / L_n} , \tag{4.18}$$

where $k_{cx} \approx 3 \cdot 10^{-8}\ cm^3 s$ is the charge-exchange rate coefficient, j_a the density of neutral flux, and L_n is the plasma density e-folding length. By taking j_a as the density (averaged over the magnetic surface) of a local influx of 10^{22} neutrals/s and $L_n \approx 1cm$ one gets $\gamma \approx 3 \cdot 10^4$ neutrals/s. For $k_y \geq 1cm^{-1}$ (for perturbations of smaller k_y the distortion of parallel current is too small) a mixing length approximation results in an increase of the particle diffusivity by some m^2/s.

4.6.3 Drift Resistive Ballooning mode (DRB)

Since the tokamak edge plasmas are collisional, the Drift Resistive Ballooning (DRB) [24] instability, driven by the pressure and the magnetic curvature effects, is a likely candidate for the edge turbulence.

The physics of the DRB-mode is similar to the one described in the previous section, where the growth of an instability came through the perturbation of the component of the plasma current parallel to the magnetic field. The initial perturbation of the plasma pressure, $\tilde{P}$, leads to a perturbation of the radial component of plasma current, $\tilde{j}_r$:

$$\frac{\partial \tilde{P}}{\partial y} = -\tilde{j}_r \frac{B}{c}. \qquad (4.19)$$

In an inhomogeneous magnetic field , $B \sim 1-(r/R)\cos\theta$, such a radial current is not divergence-free. That results in the perturbation of the parallel current, $\tilde{j}_{\|}$. Thus, following Eq. (4.17), the radial drift created by $\tilde{j}_{\|}$ enhances the initial perturbation and leads to an instability growth.

The transport driven by the DRB-mode is given by the expression [24]:

$$D_{DRB} \approx (2\pi q \rho_e)^2 \nu_e \frac{R}{L_n}. \qquad (4.19)$$

The strong injection of neutrals by recycling can affect the DRB-mode, since it causes the significant modification of the plasma edge parameters. As it is discussed in section 3.8, the strong gas puff leads to a noticeable increase of $n_{e\ LCMS}$ and a simultaneous reduction of the edge temperature. These modifications result in an increase of the electron collisional frequency ν_e and can lead to an increase of the transport due to DRB unstable modes. Moreover, the strong coupling between the neutral population and the plasma fluid can lead to the further amplification of the DRB-mode due to an influence of neutrals on the plasma motion described in the previous section [25].

The computations presented in the next paragraph show that, the DRB-mode explains the edge particle diffusion under the RI-mode conditions and reproduces an increase of the transport needed for an interpretation of the “strong gas puff effect”.

4.7 Computations made with modified transport model

As it follows from the modeling presented in sections 4.2 and 4.3, the edge transport model given by the Eq. (4.7) is not capable of the reproduction of the increased edge diffusion during RI-L transition triggered by the strong gas injection. It suggests to modify the transport model in the RITM-code (see section 4.1) and take into account one of the modes described in the previous section.

The DRB mode [24] is an appropriate candidate for the turbulence driving the edge transport, where the diffusion coefficient is given by Eq. (4.19). It is important to note that Eq. (4.19) does not contain any direct "effects of neutrals" and the level of the transport is determined from the plasma edge parameters. Possible amplifications for the DRB-mode produced by the direct influence of neutrals on the plasma motion or by the local perturbation of the temperature on the magnetic surface, which are not taken into account by Eq. (4.19), might enhance the transport by the factor of 2 on top of the level given by Eq. (4.19) [29]. That would be beneficial for an explanation of the increase of the edge diffusion produced by a strong gas injection.

Computations were done with the total diffusion governed by three types of turbulence: ITG, DTE and DRB. The time scenario of the discharge arranged in the same way as it was done in section 4.2.

Figure 4.16 represents the time traces of the normalized gas influx, edge density, edge diffusion driven by DRB-instability, line averaged effective charge, density peaking factor and recycling flux for two modeled discharges which differ by the intensity of the gas puff. In the discharge represented by dashed black curves the gas puff was maintained at a low level after the RI-mode conditions were established (t>0.3s). Such a low gas injection does not modify the edge properties of the plasma and the edge diffusion is low. Also, the edge electron density and recycling flux are low and typical for the RI-mode conditions. The density profile peaks further, and the value of the density peaking factor is up to 1.9. The value of the effective charge increases, whereas the shape of Z_{eff} profile is similar to the one in the Fig 4.2, curve *a*.

The strong gas injection in the discharge shown by solid grey curves leads to the significant modification of the plasma edge that results in a strong increase of the recycling flux. The latter give a rise to the edge transport driven by DRB-turbulence. The line-averaged value of the effective charge diminishes, and the profile of Z_{eff} becomes similar to the one in Fig. 4.2, curve *c*. The shape of the density profile changes such that the value of its peaking factor reduces to 1.5. Simultaneously, the edge density is considerably higher than in the computation made with a low gas puff.

Figure 4.17 shows the final profiles of density and transport coefficients for two discharges compared in Fig. 4.16. It is seen that in the case of a low injection rate, the combination of ITG, DTE and DRB modes allows to model the density profile in perfect agreement with the experiment (Fig 4.17 (a)). In particular, the edge region of the plasma can be reproduced in detail by the DRB-mode, whereas at the inner radii the transport is governed by DTE and ITG modes. This figure also confirms our previous findings; in discharges with low fuelling rates the ITG-mode is suppressed on the major part of plasma radii. That preserve the confinement of the H-mode or higher quality.

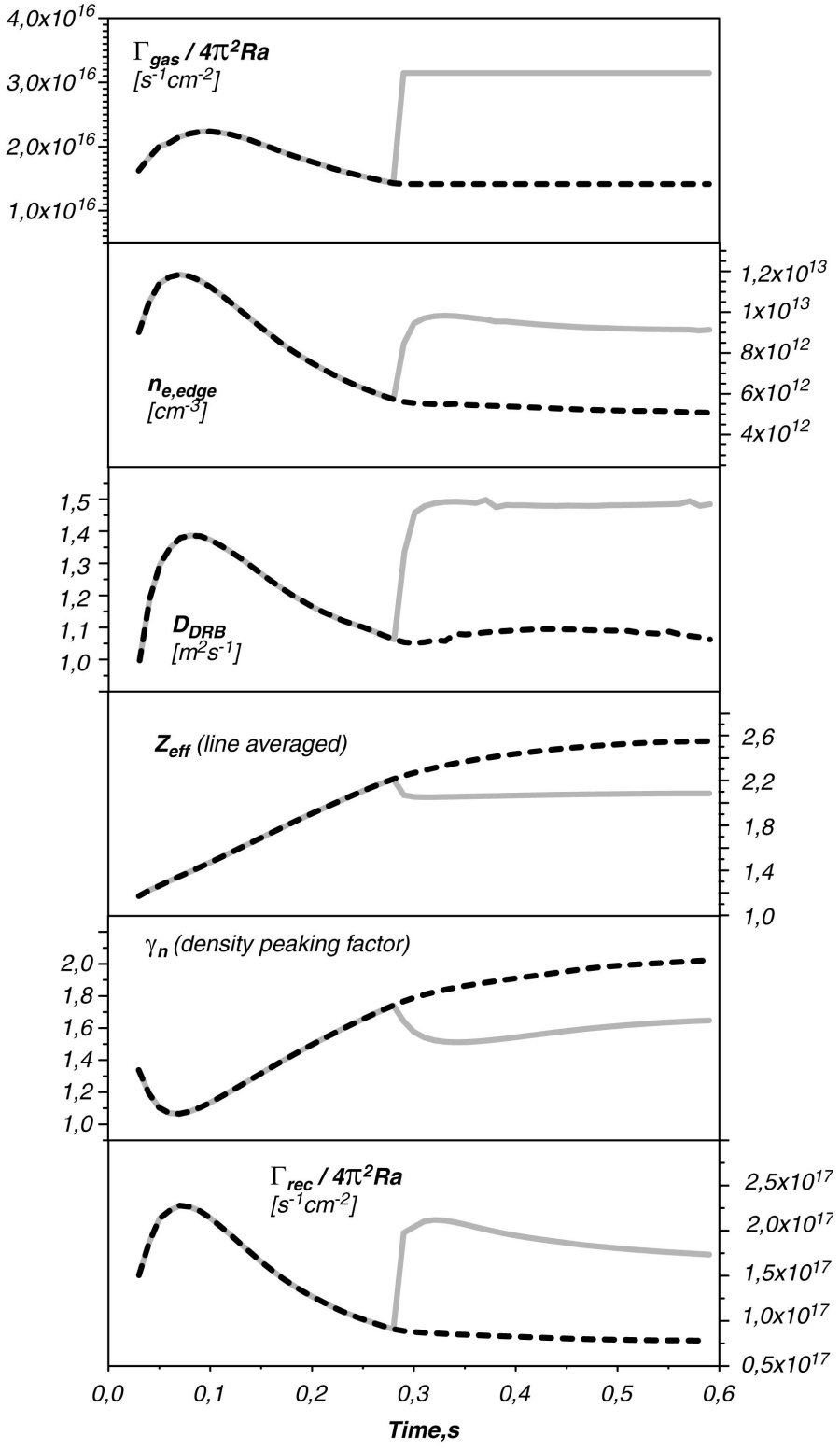

Fig. 4.16 Time traces of the normalized gas influx, edge density, edge diffusion driven by DRB-instability, line averaged effective charge, density peaking factor and recycling flux for two modeled discharges differing by the intensity of the gas puff.

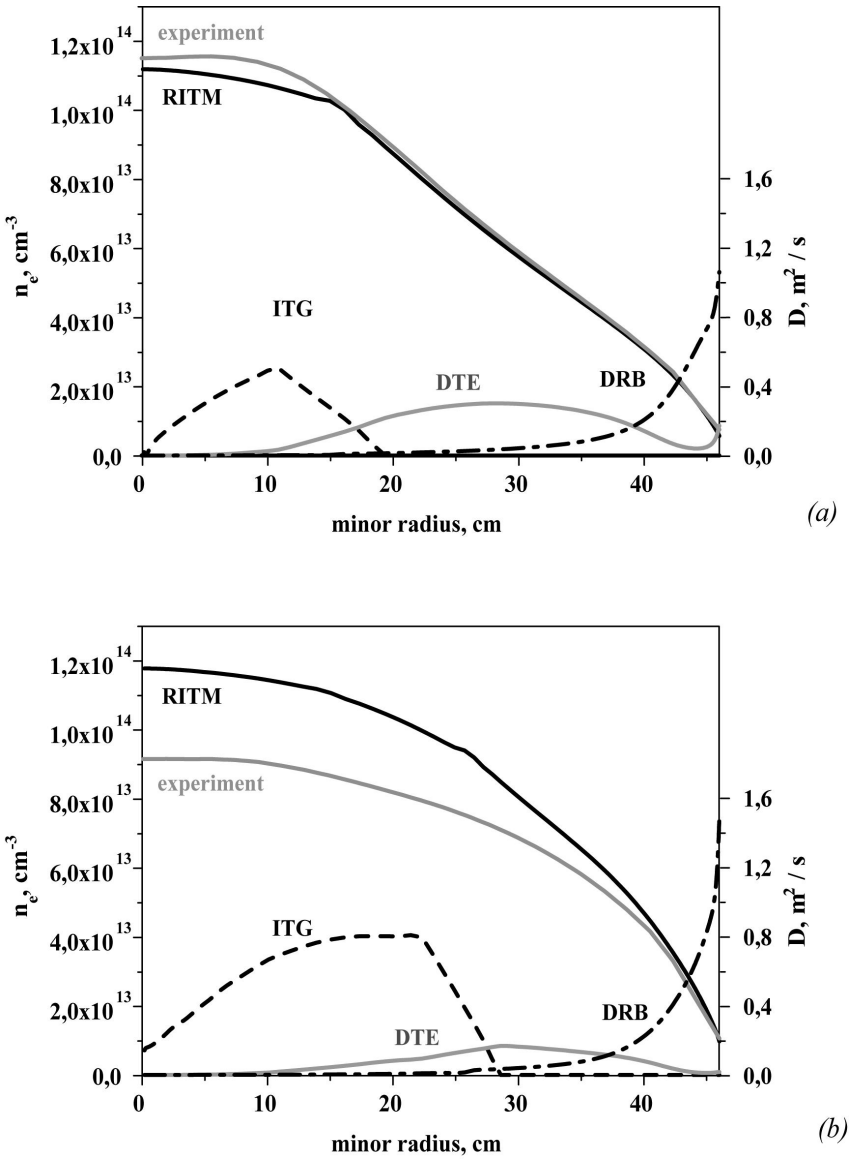

Fig. 4.17 Profiles of density and diffusion coefficients for the discharges presented in Fig. 4.16

The shape of the density profile modelled with a strong gas puff imitates the experimental one, and at the edge both of them are congruent. Significant reduction of the Z_{eff} value being the result of an increased edge transport driven by DRB-turbulence, together with a broadening of the density profile, are the crucial factors for the resumption the ITG-instability in a wide radial zone. The latter, as it is apparent from Fig. 4.9, brings the confinement back to the L-mode level.

Thus, the DRB-mode allows to reproduce the experimental time evolution of discharges with different fuelling rates in a self-consistent manner. The profiles computed with the edge transport driven by DRB-turbulence demonstrate the perfect agreement with experimental observations. Moreover, Fig. 4.16 has demonstrated that strong gas puffs effect the core confinement through an increase of the recycling flux activating the edge turbulence. The latter is supported by experimental observations presented in Fig. 3.20, showing the strong correlation of the confinement properties of RI-mode plasmas to the recycling flux.

4.8 Discussions of still existing problems

This thesis has demonstrated that the RITM-code is capable of explaining the effect of a gas puff on the plasma performance. Nevertheless, there are still some slight discords between the modelled and the experimental results. The major problem is the disagreement of 20% in the line-averaged densities between the experimental and RITM density profiles.

The RITM-computations reproduce the typical broadening of the density profile experimentally observed with the strong gas puff. The modelled profile mimics the experimental one. The strong gas puff in the RITM-code rises significantly the line-averaged density, whereas in the experiment it leads to the saturation in density. There are two possible reasons for such a behavior: (i) the fuelling efficiency assumed in the RITM-code is equal to one, it means that all of the puffed neutrals penetrate freely through the scrape of layer (SOL) and are ionized only in the core plasma; (ii) probably the total particle transport in RITM-code is lower than the experimental one and some other instabilities should be taken into account.

During the work several attempts, aimed to reproduce the value of the line-averaged density in computations, were done. Firstly, a very simple model describing the particle balance in the SOL, where ionization in the SOL should reduce the fuelling efficiency, was introduced into the RITM-code. In contrary to our believe, the computations made with this rough SOL model did not reproduce the line-averaged density in agreement with experiment. We expect that more sophisticated model could slightly improve the numerical results but, they will not change them principally.

The second attempt was a modification of the transport. One sees that experimental and modeled profiles [Fig.4.17 (b)] disagree in the central zone, whereas the reconstruction of profile at the edge is well done by DRB-mode. It suggests to take into account one of the additional modes, besides the toroidal ITG and DTE, which might drive the central transport.

The first candidate is the Electron Temperature Gradient (ETG) instability [26]. The physical mechanism of this mode is very similar to the ITG and the mode become destabilized by the temperature gradient when the parameter η exceeds the critical level, $\eta_{crit} = 1/6 + 1/(4\varepsilon_n) + \varepsilon_n(49/36)$. Here $T_i = T_e$ is assumed. In contrast to ITG, the contribution to the particle transport from ETG turbulence does not come from the effect on trapped particles (because ions are not trapped), but from the interaction with a Kelvin-Helmholtz (or zonal flow) secondary instability, whose saturation level was calculated by Singh *et al* 2001 [26].

As it can be seen from Fig. 4.18 the contribution of the ETG mode to transport is very small. It is also expected from the difference in Larmor radii of electrons and ions, and does not prevent the rise of the density.

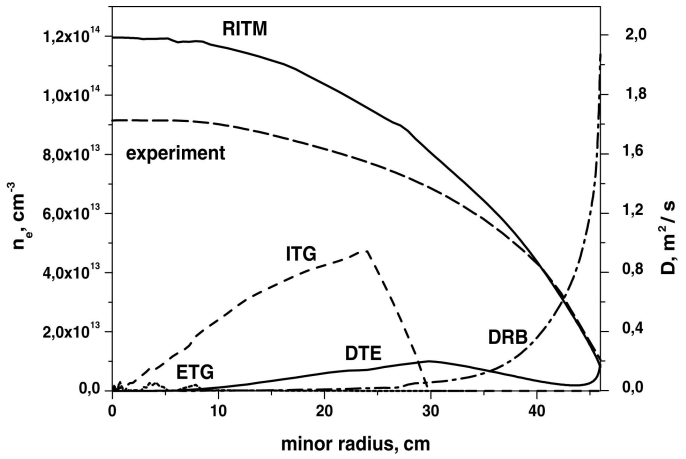

Fig. 4.18 Contribution of the Electron Temperature Gradient instability to the total transport.

On the other hand, the important contribution to transport might be given by the slab branch of the ITG-mode. This instability occurs due to the gradient of the ion temperature and is stabilized by parallel motion effects [28]. The driving mechanism for the toroidal ITG is based on the magnetic curvature effects. Usually, this instability is not taken into account for the transport in tokamaks since the level of the transport governed by slab ITG is much lower than that from the toroidal one. Besides, that does not demonstrate the bifurcation behavior, as it is done by the toroidal ITG.

Since the theory, which combines both branches of the ITG mode does not exist, in the first approximation, we put some small addition, of about 0.15 m^2/s, to the total transport at the radii where the growth rate of the slab ITG is different from zero.

As it is seen from Fig. 4.19, this assumption allows to reproduce the density profile in perfect agreement with experimental one. At the same time, it does not change any conclusion of sections 4.2-4.9 about the physical mechanism leading to the confinement degradation.

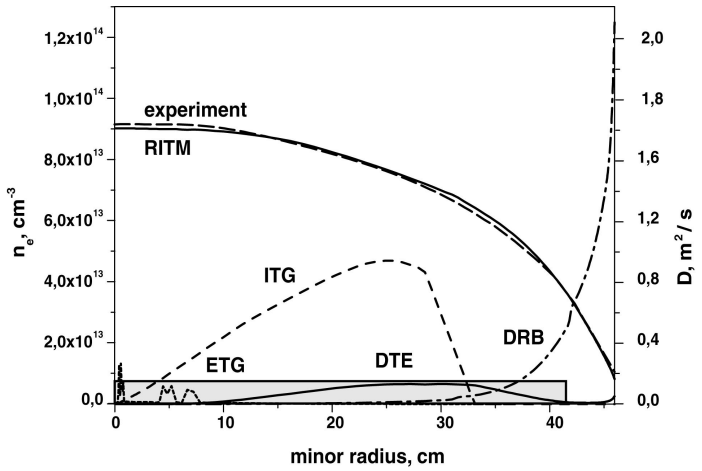

Fig. 4.19 Computations hold with the small addition to the central transport.

4.9 References

1. Tokar M.Z. 1994 Plasma Phys. and Control. Fusion **36** 1819
2. Solov'ev L.S. and Shafranov V.D. 1970 Review of Plasma Physics **5** 1
3. Hirshman S.P. *et al* 1977 Nucl.Fusion **17** 611
4. Baelmans *et al* 1995 in: Proceedings of the 22nd European Physical Society Conference on Controlled Fusion and Plasma Physics, Bournemouth, Europhys. Conf. Abstr., vol.19C, 1995, IV-321
5. Kadomtsev B.B. and Pogutse O.P 1971 Nucl. Fusion **11** 67
6. Endler M. *et al* 1995 J. Nucl. Mater. **220-222** 293
7. Isichenko M.B. *et al* 1995 Phys. Rev. Lett. **74** 4436
8. Yankov V.V. and Nycander J. 1997 Phys. Plasmas **4** 2907
9. Baker D.R and Rosenbluth M.N. 1998 Phys. Plasmas **5** 2936
10. Wesson J. 1997 *Tokamaks*, Oxford Engineering Science Series **48**, Claredon Press, Oxford, 2nd edition, 1997.
11. Hirshman S.P. *et al* 1977 Nucl.Fusion **17** 611
12. Weynants R.R. *et al* 1999 Nucl. Fusion **39** 1637
13. Wenzel K.W. and Sigmar D.J. 1990 Nucl. Fusion **30** 1117
14. Tokar M.Z. *et al* 2000 Phys. Rev. Lett. **84** 895
15. Dreval V. et al 1999, Microwave reflectometric studies on TEXTOR-94, 26th EPS, Maastricht
16. Unterberg B. *et al.* 2000 Improved energy confinement at trans-Greenwald densities in discharges with a radiating edge in the tokamak TEXTOR-94, IAEA-CN-77/EX5/2
17. Crowley T. and Mazzucato E. 1985 Nucl.Fusion **25** 507
18. Singh R. et al, 1996, Plasma Phys. And Control. Fusion **38** 1985-1997

19. Ross D., 1994, Phys. Plasmas, Vol. 1, No. 8, 2630

20. Zhang Y.Z. and Mahajan S.M., 1992, Phys. Fluids, **B 4**, 207

21. Linson L. M. and Workman J. B., 1970, J. Geophys. **75** 3211

22. Daughton W. *et al* 1998 Phys. of Plasmas **5** 2217

23. Tokar M.Z. 1993 Plasma Phys. and Control. Fusion **35** 1119

24. Gusdar P.N. *et al* 1993 Phys. Fluids **B 5** 3712

25. Ödblom A. et al 1999 Phys. Plasmas, **vol. 6**, no. 8, 3239

26. Singh R. and Tangri V., Physics of Plasmas, 2001, **Vol. 8**, Issue 10 pp. 4340

27. Diamond P.H. and Rosenbluth M.N. 2000 Phys. Rev. Lett. **84** 4842

28. A.Rogister, 2000, Phys. of Plasmas, vol.7 no.**12**, pp. 5070

29. M.Tokar, private communications

Chapter 5

Summary and Conclusions

In the tokamak TEXTOR the seeding of impurities (Ne, Ar, Si) brings the confinement to the level of the H-mode, considered as the major operational scenario for the reactor-size machine, or even higher **[§3.1,3.2]**. The physics mechanism for this improved confinement regime, called **Radiative Improved (RI) mode**, is the suppression of the toroidal **Ion Temperature Gradient (ITG)** instability through the dependence on the effective charge and the density peaking **[§3.4]**. The particle transport in the RI-mode is governed by the Dissipative Trapped Electron instability. That mode establishes the scaling for the energy confinement time, increasing linearly with the density **[§2.6,3.6]**. **The aim of recent experiments performed on TEXTOR is to attain the densities significantly above the Greenwald limit [§2.2] with simultaneous maintenance of the RI-mode quality confinement.**

External gas puffing is the simplest and most frequent method for the control of the plasma density in fusion devices. However, as it has been found in many tokamaks, a too intensive puffing can lead to a progressive deterioration of the energy and particle confinement. Experiments with different scenarios of gas puff have been performed on TEXTOR tokamak in discharges with impurity seeding **[§3.6]**. It has been found that a **strong gas puff allows to increase the density much above the empirical Greenwald limit, but at the same time it leads to the confinement deterioration** towards the Low confinement mode. **Strong gas puff also interrupts the peaking of the density profile [§3.7], observed after the neon injection, and leads to the appreciable flattening of it**. Simultaneously, the **strong reduction of the effective charge is observed [§3.7]**.

Conversely, a **low gas puff allowed to preserve the energy confinement of the H-mode**, or even higher quality, **and to maintain the peaked density profile**, which is of principal importance for RI-mode performance **[§3.6,3.7]**. It also **does not affect the value of the effective charge**.

Moreover, it has been found that that the **quality of confinement has a strong link to the plasma edge properties [§3.8]**. High performance, with the energy confinement time being at least 80% of the value predicted by the RI-mode scaling, at high densities is **characterized by a low density at the LCMS and by a low neutral pressure** at the wall. In plasmas where the gas injection triggers the confinement

deterioration, **the edge density, the neutral pressure at the edge and the recycling flux are much higher** than in discharges with a low gas puff. A strong connection of the energy confinement degradation with the latter quantities is observed.

The **transport model [§3.5]** used here was shown to explain the transition from L to RI-mode as a bifurcation between the plasma states, where the transport is governed mainly by the ITG and DTE modes, respectively. The high value of the effective charge and the high density peaking are thought to be instrumental in that bifurcation process.

The present thesis explains the degradation of the confinement caused by the strong gas puff.

To that end, the one-dimensional transport code **RITM [§4.1]** was modified in order to simulate the effect of the gas puff on the confinement properties. The calculations have been arranged in order to reproduce the experimental **density profiles**, plasma **effective charge** and also the **time evolution** of discharges similar to experiments. Three series of simulations were performed:

1. The calculated density profile in the case of a **low gas puff [§4.2.1]** reproduces well the experimental RI-mode density with a steep gradient over a wide plasma zone, the effective charge being in the range 1.8-2.4. As a result, the ITG-mode is suppressed over 2/3 of plasma radii. These runs allows to conclude that the **low gas puff does not affect the confinement properties of the RI-mode**, since it does not resume the ITG-induced transport firstly suppressed by the neon injection.

2. A **strong gas puff [§4.2.2]** results in a considerable broadening of the density profile in rough agreement with the experimental behaviour. However, the increase in the edge density and its gradient significantly exceed the measured values. The density profile is too flat in the outer plasma region. Moreover, the effective charge rises in the whole plasma column with respect to the low fuelling case, which contradicts the experimental observations. An analysis of results shows that the low edge transport does not allow the impurity ions to escape the plasma.

3. The third series of calculations was done with a **strong gas puff and a simultaneous increase of the edge transport [§4.2.3]**. In this case the **flattening of the density profile occurs in agreement with the experimental observations**, without formation of an extremely high density and density gradient at the edge. The value of the **effective charge decreases** in the whole plasma column. These changes of the plasma parameters result in the **resumption of the ITG-induced transport, and the latter causes the progressive confinement deterioration**. Computations also show that, at the given radius, the transition from RI to L-mode can be explained as the bifurcation inverse to one observed when the puff of impurities brings the confinement to the RI-mode level **[§4.3]**.

All of the presented results have clearly demonstrated that the **confinement degradation in plasmas with a strong gas puff can be explained by the model**

described in [§3.5 and 4.1]. The computations hold for different intensities of the gas puff, are **capable of the explicit reproduction of different parameters profiles and also allow to model the evolution of the discharge [§4.2]**. It was also shown that the **degradation of confinement occurs due to a significantly increased edge transport**. This follows from the RITM modeling **[§4.2]** and is supported by reflectometer measurements **[§4.4]**.

The review of the possible mechanisms for the edge instabilities being sensitive to the neutral puff suggests a modification of the transport model used in the RITM-code by taking into account the **Drift Resistive Ballooning (DRB)** instability driven by the pressure and the magnetic curvature effects **[§4.6]**. The computations made with the edge transport governed by DRB instability allow to reproduce, in a **self consistent manner**, the evolution of different parameters profiles in discharges with different intensities of the gas puff **[§4.7]**. These computations also support our previous findings that **the strong gas injection results in the significant increase of the edge diffusion**. The fact that our one-dimensional calculation appear to be capable of explaining the experimental results, tend to indicate that local effects are not absolutely necessary. Even a uniform gas puff is able to trigger an also uniform recycling enhancement, which, in steady state, balances the increased plasma outflow driven by the DRB-mode.

List of figures:

Acknowledgments

Here I would like to acknowledge for people who made this work possible and who helped me during the work.

In first I wish to thank for Prof. Dr. K.H Spatschek for the possibility to perform my PhD work in frames of Graduiertenkolleg on "High-temperature Plasma Physics" in Heinrich-Heine Universität Düsseldorf.

Also I would like to give special acknowledgments for Dr. M Tokar, who helped me very much in understanding of physical basics of transport processes in tokamak and also helped to learn the RITM-code.

I wish to thank for R. Weynants, A. Messiaen, P. Dumortier, B. Unterberg, G. Van Wassenhove, S. Soldatov, R. Singh, D. Reiser and J. Ongena for the knowledge I have got from them in Experimental and Theoretical Plasma Physics during my PhD studies. I also would like to mention here that besides of physics I have learned many other things from these people, like operation with TEXTOR data base and programming, which helped me a lot in my work.

The TEXTOR team is gratefully acknowledged for providing excellent experimental conditions.

My special thanks are for the Laboratory of Plasma Physics in Ecole Royale Militaire, Brussels for the possibility of joint work with the team of this laboratory.

My private thank I address to my wife for the huge moral support given for me during three years of PhD studies and, in particular, for the birth of my son which I consider as one of the most important issues from this time.